Final Report

Failure of Non-Circular Composite Cylinders

NAG1-01072

Submitted by M.W. Hyer

Virginia Polytechnic Institute and State University

September 2004

This final report is the thesis of Gabriela F. Wolford for a Master of Science degree in Engineering Mechanics from Virginia Polytechnic Institute and State University.

FAILURE INITIATION AND PROGRESSION IN INTERNALLY PRESSURIZED NON-CIRCULAR COMPOSITE CYLINDERS

ABSTRACT

In this study, a progressive failure analysis is used to investigate leakage in internally pressurized non-circular composite cylinders. This type of approach accounts for the localized loss of stiffness when material failure occurs at some location in a structure by degrading the local material elastic properties by a certain factor. The manner in which this degradation of material properties takes place depends on the failure modes, which are determined by the application of a failure criterion. The finite-element code STAGS, which has the capability to perform progressive failure analysis using different degradation schemes and failure criteria, is utilized to analyze laboratory scale, graphite-epoxy, elliptical cylinders with quasi-isotropic, circumferentially-stiff, and axially-stiff material orthotropies. The results are divided into two parts. The first part shows that leakage, which is assumed to develop if there is material failure in every layer at some axial and circumferential location within the cylinder, does not occur without failure of fibers. Moreover before fibers begin to fail, only matrix tensile failures, or matrix cracking, takes place, and at least one layer in all three cylinders studied remain uncracked, preventing the formation of a leakage path. That determination is corroborated by the use of different degradation schemes and various failure criteria. Among the degradation schemes investigated are the degradation of different engineering properties, the use of various degradation factors, the recursive or non-recursive degradation of the engineering properties, and the degradation of material properties using different computational approaches. The failure criteria used in the analysis include the noninteractive maximum stress criterion and the interactive Hashin and Tsai-Wu criteria. The second part of the results shows that leakage occurs due to a combination of matrix tensile and compressive, fiber tensile and compressive, and inplane shear failure modes in all three cylinders. Leakage develops after a relatively low amount of fiber damage, at about the same pressure for three material orthotropies, and at approximately the same location.

Table of Contents

Chapter 1 Introduction 1

Chapter 2 Use and Characterization of Computational Analysis Software 9

2.1 STAGS Progressive Failure Analysis 10

2.2 Study of Simple Cases 15

2.2.1 Single-Layer Square Plate Under Inplane Tensile Loading 15

2.2.2 Internal Radial Loading of a Single-Layer Circular Cylinder 23

Chapter 3 Matrix Failure Scenarios in Internally Pressurized Elliptical Cylinders Using Different Degradation Schemes 33

3.1 Problem Formulation 34

3.2 Finite-Element Model 36

3.3 Method of Illustration 37

3.4 Failure Initiation and Progression in a Quasi-Isotropic Elliptical Cylinder Using the Maximum Stress Failure Criterion and the Baseline Degradation Scheme with β=0.2 38

3.5 Effects of not Degrading G_{12} on the Matrix Failure Scenarios 49

3.6 Influence of β on the Matrix Failure Scenarios 55

3.7 Effects of Recursive Degradation on the Matrix Failure Scenarios 61

3.8 Evaluation of Computational Algorithms 67

3.9 Summary of Matrix Failure Scenarios in Internally Pressurized Elliptical Cylinders Using Different Degradation Schemes 72

Chapter 4 Matrix Failure Scenarios in Internally Pressurized Elliptical Cylinders Using Different Failure Criteria **78**

4.1 Comparison Between the Maximum Stress and Hashin Failure Criteria 78

4.2 Comparison Between the Maximum Stress and Tsai-Wu Failure Criteria 85

4.3 Summary of Matrix Failure Scenarios in Internally Pressurized Elliptical Cylinders Using Different Failure Criteria 89

Chapter 5 Failure Analysis Beyond Fiber Failure in Internally Pressurized Elliptical Cylinders **92**

5.1 Leakage Path Formation in Internally Pressurized Elliptical Cylinders 92

5.2 Summary of Failure Analysis Beyond Fiber Failure in Internally Pressurized Elliptical Cylinders..... 98

Chapter 6 Conclusions and Future Work **99**

6.1 Conclusions 99

6.2 Future work 102

References..... **103**

List of Figures

Figure 2.1: Geometry and nomenclature of a square plate reference surface subjected to an inplane tensile loading 16
Figure 2.2: Applied inplane load vs. v^o-displacement at $y=+a/2$ 24
Figure 2.3: Applied inplane load vs. u^o-displacement at $x=-a/2$ 24
Figure 2.4: Geometry and nomenclature of a circular cylinder reference surface subjected to an internal radial loading 25
Figure 2.5: Internal radial load vs. outward displacement at any axial location 31
Figure 2.6: Internal radial load vs. axial displacement at $x=+L/2$. 31
Figure 3.1: Geometry and nomenclature of elliptical cylinder. 36
Figure 3.2: Finite-element mesh of elliptical cylinder 36
Figure 3.3: Method of illustrating one quadrant of the elliptical composite cylinder 37
Figure 3.4: Matrix cracking scenario for the quasi-isotropic $[\pm 45/0/90]_s$ elliptical cylinder at different pressure levels, maximum stress criterion, baseline degradation scheme, $\beta=0.2$ 41
Figure 3.5: Matrix cracking scenarios for elliptical cylinders with different material orthotropy, maximum stress criterion, baseline degradation scheme, $\beta=0.2$. 46
Figure 3.6: Effects of shear modulus degradation on the matrix cracking scenario for the quasi-isotropic $[\pm 45/0/90]_s$ elliptical cylinder, maximum stress criterion, $\beta=0.2$. 50
Figure 3.7: Effects of shear modulus degradation on the matrix cracking scenario for the circumferentially-stiff $[\pm 45/90_2/0_{1/2}]_s$ elliptical cylinder, maximum stress criterion, $\beta=0.2$ 52
Figure 3.8: Effects of shear modulus degradation on the matrix cracking scenario for the axially-stiff $[\pm 45/0_2/90_{1/2}]_s$ elliptical cylinder, maximum stress criterion, $\beta=0.2$ 54
Figure 3.9: Effects of degradation factors on the matrix cracking scenario for the quasi-isotropic $[\pm 45/0/90]_s$ elliptical cylinder, maximum stress criterion, baseline degradation scheme. 56

Figure 3.10: Effects of degradation factors on the matrix cracking scenario for the circumferentially-stiff $[\pm 45/90_2/0_{1/2}]_s$ elliptical cylinder, maximum stress criterion, baseline degradation scheme 58

Figure 3.11: Effects of degradation factors on the matrix cracking scenario for the axially-stiff $[\pm 45/0_2/90_{1/2}]_s$ elliptical cylinder, maximum stress criterion, baseline degradation scheme 60

Figure 3.12: Effect of recursive degradation on the matrix cracking scenario for the quasi-isotropic $[\pm 45/0/90]_s$ elliptical cylinder, maximum stress criterion, β=0.2 64

Figure 3.13: Effect of recursive degradation on the matrix cracking scenario for the circumferentially-stiff $[\pm 45/90_2/0_{1/2}]_s$ elliptical cylinder, maximum stress criterion, β=0.2 65

Figure 3.14: Effect of recursive degradation on the matrix cracking scenario for the axially-stiff $[\pm 45/0_2/90_{1/2}]_s$ elliptical cylinder, maximum stress criterion, β=0.2 66

Figure 3.15: Matrix cracking scenarios for the quasi-isotropic $[\pm 45/0/90]_s$ elliptical cylinder, maximum stress criterion, baseline degradation scheme, β=0.2, different computational algorithms 73

Figure 3.16: Matrix cracking scenarios for the circumferentially-stiff $[\pm 45/90_2/0_{1/2}]_s$ elliptical cylinder, maximum stress criterion, baseline degradation scheme, β=0.2, different computational algorithms 74

Figure 3.17: Matrix cracking scenarios for the axially-stiff $[\pm 45/0_2/90_{1/2}]_s$ elliptical cylinder, maximum stress criterion, baseline degradation scheme, β=0.2, different computational algorithms 75

Figure 4.1: Matrix cracking scenarios for maximum stress and Hashin failure criteria for the quasi-isotropic $[\pm 45/0/90]_s$ elliptical cylinder, baseline degradation scheme, β=0.2 80

Figure 4.2: Matrix cracking scenarios for maximum stress and Hashin failure criteria for the circumferentially-stiff $[\pm 45/90_2/0_{1/2}]_s$ elliptical cylinder, baseline degradation scheme, β=0.2 82

Figure 4.3: Matrix cracking scenarios for maximum stress and Hashin failure criteria for the axially-stiff $[\pm 45/0_2/90_{1/2}]_s$ elliptical cylinder, baseline degradation scheme, β=0.283

Figure 4.4: Matrix cracking scenarios for maximum stress and Tsai-Wu failure criteria for the quasi-isotropic $[\pm 45/0/90]_s$ elliptical cylinder, non-recursive degradation of E_2, ν_{12}, and ν_{21}, β=0.2 86

Figure 4.5: Matrix cracking scenarios for maximum stress and Tsai-Wu failure criteria for the circumferentially-stiff $[\pm 45/90_2/0_{1/2}]_s$ elliptical cylinder, non-recursive degradation of E_2, ν_{12}, and ν_{21}, β=0.2 88

Figure 4.6: Matrix cracking scenarios for maximum stress and Tsai-Wu failure criteria for the axially-stiff $[\pm 45/0_2/90_{1/2}]_s$ elliptical cylinder, non-recursive degradation of E_2, ν_{12}, and ν_{21}, β=0.2 90

Figure 5.1: Modes of failure involved in leakage for the quasi-isotropic $[\pm 45/0/90]_s$ elliptical cylinder, baseline degradation scheme, maximum stress criterion, β=0.2 94

Figure 5.2: Modes of failure involved in leakage for the circumferentially-stiff $[\pm 45/90_2/0_{1/2}]_s$ elliptical cylinder, baseline degradation scheme, maximum stress criterion, β=0.2 96

Figure 5.3: Modes of failure involved in leakage for the axially-stiff $[\pm 45/0_2/90_{1/2}]_s$ elliptical cylinder, baseline degradation scheme, maximum stress criterion, β=0.2 97

List of Tables

Table 2.1: Standard degradation schemes used by the PFA in STAGS 14
Table 3.1: First matrix failure pressures for maximum stress criterion 47
Table 3.2: First fiber failure pressures for maximum stress criterion, baseline degradation scheme, β=0.2 47
Table 3.3: Effects of shear modulus degradation on first fiber failure pressures and percent damage, maximum stress criterion, β=0.2 53
Table 3.4: Effects of degradation factors on first fiber failure pressures and percent damage, maximum stress criterion, baseline degradation scheme 59
Table 3.5: Effects of recursive degradation on first fiber failure pressures and percent damage, maximum stress criterion, β=0.2 63
Table 3.6: Effects of computational algorithms on the number of iterations and percent damage, maximum stress criterion, baseline degradation scheme, β=0.2 70
Table 3.7: Effects of computational algorithms on first fiber failure pressures and percent damage, maximum stress criterion, baseline degradation scheme, β=0.2 72
Table 4.1: Maximum stress and Hashin failure criteria predictions of initial matrix failure pressures 84
Table 4.2: Maximum stress and Hashin failure criteria predictions of first fiber failure pressures and percent damage, baseline degradation scheme, β=0.2 84
Table 4.3: Maximum stress and Tsai-Wu failure criteria predictions of initial matrix failure pressures 89
Table 4.4: Maximum stress and Tsai-Wu failure criteria predictions of first fiber failure pressures and percent damage, non-recursive degradation of E_2, ν_{12}, and ν_{21}, β=0.2 89
Table 5.1: Leakage pressures, baseline degradation scheme, maximum stress criterion, β=0.2 . . 98

Chapter 1 Introduction

Because of aerodynamic advantages, weight, and geometric constraints, future designs of fuel tanks for reusable launch vehicles may call for noncircular cylinders fabricated of fiber-reinforced laminated composite materials. A critical issue to consider in the design of composite tanks is failure due to leakage of fuel through the tank wall. Typical fuels used in these vehicles are gaseous substances, such as hydrogen and oxygen, that are liquefied at cryogenic temperatures. The internal pressure resulting from the use of these gases can produce enough material damage in the wall so that a continuous path through the layers of the composite laminate can occur. This situation is extremely hazardous, as it involves leakage of volatile fluids. To prevent this hazard it is essential that the conditions under which leakage is likely to occur be known.

To study the potential for leakage in noncircular cylinders, a progressive failure analysis will be used here. Such an approach is based on the manner by which composite materials are known to fail. Generally, at a high enough load level, small local cracks in the material initiate the failure process. Due to the material softening because of the cracking, stresses redistribute and more cracking occurs. As the load level increases, the failed, or damaged, region becomes larger and stresses are redistributed further. At some level of load, fibers begin to fail at a particular location. Stresses are again redistributed, more failures occur, the load is increased, more fibers fail, more matrix cracking occurs, and the region of damage continuous to grow. At some point the material can no longer sustain the load and the laminate breaks into two pieces, or in the case of a pressurized cylinder, the pressure rapidly escapes and a large hole develops. The work here focuses on an earlier step of damage, namely, one when the cylinder is intact but leakage is beginning. This could occur due to excessive matrix cracking with no fiber failure, or it may involve a small amount of fiber failure. The primary objective of the study here is to determine at what pressure levels leakage occurs and what the modes of failure are when this happens. Here, leakage will be

assumed to occur if there is material failure in every layer at some axial and circumferential location within the cylinder.

To quantitatively assess the pressure levels and the modes of failure associated with leakage in noncircular laminated composite cylinders, it is necessary to adopt a specific type of noncircular geometry. For this study, a cylinder with an elliptical cross section will be used. The reason for this choice is that past works have characterized some aspects of the response of elliptical composite cylinders and, if needed, closed-form expressions for the cross-section geometry are available. Among the past works that described the behavior of elliptical cylinders is the study carried out by McMurray and Hyer in [1, 2]. In that study, using a semi-analytical approach, the effects of noncircular geometry, geometric nonlinearities, and different material orthotropies on the response and failure of internally pressurized elliptical cylinders with clamped boundary conditions were investigated. To look at the effects of noncircular geometry, a portion of the study compared the geometrically linear response of a quasi-isotropic $[\pm 45/0/90]_s$ elliptical cylinder, where 0 deg. is the axial direction, to that of a circular cylinder with the same lay-up. In the modeling of the elliptical cylinder, McMurray and Hyer used Donnell shell theory. This portion of the study concluded that in elliptical cross-sections the displacement response varies with axial and circumferential position, producing spatially varying displacement gradients. Through the constitutive relation, that variation is reflected in the stresses, resulting in stress concentrations at specific axial and circumferential locations. The specific locations of those stress concentrations found by McMurray and Hyer can be summarized as follows:

i. The maximum force resultants in the axial direction occur at the clamped boundaries at the ends of the major diameter.

ii. The maximum force resultants in the circumferential direction occur partway between the clamped boundaries and the midspan of the cylinder at the ends of the minor diameter.

iii. The maximum shear force resultants occur near the clamped boundaries part way between the ends of the minor diameter and the ends of the major diameter. It is important to note that due to the presence of the stiffnesses D_{16} and D_{26}, those maximum values do not occur in every quadrant

of the cylinder. In fact, they occur in opposite quadrants at one clamped boundary and the reverse of that at the other clamped boundary.

iii. The maximum magnitude of the bending moment resultants in the axial and circumferential direction and shear moment resultants occur at the clamped boundaries at the ends of the minor diameter.

In investigating the influence of geometric nonlinearities on the response of elliptical cylinders, McMurray and Hyer found that if geometric nonlinearities are included in the analysis, the magnitude and location of the maximum displacement response are slightly different with respect to the geometrically linear analysis. Those nonlinear effects are found in the strain and stress responses as well. To determine the effects of material orthotropy, the study compared the quasi-isotropic cylinder with two other cylinders which had circumferentially-stiff, $[\pm 45/90_2/0_{1/2}]$, and axially-stiff, $[\pm 45/0_2/90_{1/2}]$, lay-ups. Despite the fact these cylinders were of different wall thickness, these lay-ups were chosen because for each cylinder there was at least one layer with fibers in the axial direction and one layer with fibers in the circumferential direction. To do otherwise would be unrealistic. Using a geometrically nonlinear analysis, the study found that material orthotropy diminishes or amplifies the effect of elliptical geometry in some of the responses. For example, an axially-stiff material orthotropy amplifies the circumferential strain response of an elliptical cross-section, while a circumferentially-stiff material orthotropy tends to diminish it. On the other hand, a circumferentially-stiff material orthotropy accentuates the axial strain response of an elliptical cross section, while the axially-stiff material orthotropy mitigates it. Making use of the above findings, McMurray and Hyer included failure predictions. By using the maximum stress and Hashin failure criteria and geometrically linear and nonlinear analyses, the failure pressure, location, and mode were predicted for each of the three cylinder lay-ups. The study found that both criteria predicted that the initial mode of failure was matrix tension, or matrix cracking, and that it occurred at the clamped boundaries in all the cylinders. The two criteria predicted that for the quasi-isotropic and axially-stiff cylinders the pressure for initial failure was higher than that for the circumferentially-stiff cylinder. Regarding the circumferential location and layer where the matrix failure occurred: Both criteria predicted that, in the first two cylinders, matrix cracking occurred partway between the ends of the minor and major diameters at the inner most

+45° layer. This cracking did not occurred in all the quadrants of the cylinder due to the presence of the stiffnesses D_{16} and D_{26}. The cracking occurred at only two opposite quadrants at each clamped boundary. According to both criteria, first failure in the circumferentially-stiff cylinder appeared at the ends of the major diameter at the outer most 90° layer. When geometrical nonlinearities were included in the analysis, in general, the failure pressures were higher and circumferential locations were somewhat different than when only geometrical linearities were used. The study also determined the first fiber failure pressure, location, and mode using the same two failure criteria and analyses. In this analysis of first fiber failure, the effects of any previous matrix failures were ignored. For the geometrically linear case, both criteria found that the first fiber failure was due to fiber compression in the three cylinders. Although different for each degree of orthotropy, the two criteria predicted similar failure pressures and locations. For the geometrically nonlinear case, it was found that the Hashin criterion predicted that the mode of failure was fiber tension for the circumferentially-stiff cylinder; however, the maximum stress criterion predicted that the first fiber failure was due to fiber compression.

Though useful, since the findings in [1] give an accurate idea of where and when initial matrix cracking may occur in elliptical composite cylinders, the effort of predicting first fiber failure was somewhat limited. Because no consideration was given to the loss of local stiffness near the region where the first matrix crack occurred and to the consequent redistribution of stresses, which may cause additional matrix cracks, the first fiber failure prediction may not have been accurate. In other words, the study did not use a progressive failure analysis to determine the effects of loss of local stiffness and development of additional cracks on the first fiber failure pressure, location, and mode of failure. In a later work, McMurray and Hyer [3] accounted for the loss of stiffness due to previous matrix cracks. In that study, they used a progressive failure analysis to characterize the matrix cracking between the first matrix failure and the first fiber failure events, and to determine if a leakage path developed at some pressure between those two events. The study examined the matrix cracking scenario, predicted the first fiber failure, and determined if a leakage path was formed for the same internally pressurized elliptical cylinders investigated in [1]. In this case, however, instead of using a semi-analytical approach to approximate the geometrically nonlinear response of the cylinders, McMurray and Hyer used the finite-element code

STAGS (STructural Analysis of General Shells) in combination with a stand-alone pre/post processing program to perform the progressive failure analysis.

A typical progressive failure methodology, and the one used in [3], uses five basic steps, as explained by Sleight, Knight, and Wang [4]. First, a nonlinear static analysis is performed to satisfy the equilibrium of the structure which is under a certain load condition. The analysis must be nonlinear even if geometrical nonlinearities are not considered due to material nonlinearities associated with failure. These material nonlinearities enter the analysis when damage is detected and the local softening of the material causes the stiffnesses to change. Second, the stresses in each layer of the composite are calculated using a certain approach, such as the classical lamination theory. Then, those stresses are compared to the specific allowable strengths by way of a failure criterion that is used to determine the locations where failure initiates in the structure. The use of a failure criterion allows for the characterization of the failure; that is, it allows for a mode of failure to be determined. Depending upon the mode of failure, a local degradation of the material properties is then carried out at the locations where failure is detected. There is then an iteration due to the need for equilibrium to be re-established. As the local stiffnesses of the structure have changed when the material properties are degraded, under the same pressure level, the structure no longer is in equilibrium. During the iteration process, generally, more failures are encountered, the progression of the damage can be assessed, and equilibrium re-established again. At some point in the iteration process, at each specific load level, no further damage is predicted, equilibrium is satisfied, and the analysis proceeds to the next pressure level.

The manner in which the progressive failure methodology was performed in [3] was as follows. The stand-alone program used the strains computed by STAGS to calculate the stresses at the two interfaces of each layer (above and below the centroid of the layer). The program then used these stresses in the maximum stress criterion. If any of the conditions in the criterion were satisfied, then the mode of failure was identified; otherwise, the program returned to STAGS, the pressure was increased to the next load step, the strains were calculated, the program retrieved the new strains and, the process of analyzing failure was repeated. If conditions for failure were found and tensile matrix failure was identified, then the elastic modulus normal to the fibers and the inplane shear modulus were multiplied by a factor of β, specifically β=0.2. This level of property

reduction followed the work of Camanho and Matthews in [5], who followed the findings of other researchers, as cited in [5]. These reduced moduli were then input to STAGS, a new analysis with these new properties was executed to compute the strains, and the process was repeated at a specific load level until no more failures were detected. The results obtained using this procedure indicated that first failure was due to matrix cracking at the clamped boundaries in all three cylinders, as expected from the results in [1,2]. The first matrix failure pressures and circumferential locations and through thickness locations within the cylinder wall were similar to the ones predicted by the geometrically nonlinear analysis in [1,2]. The first fiber failure pressures, however, were lower than the pressures predicted in [1,2] using the geometrically nonlinear analysis, the maximum stress failure criterion, and ignoring the effects of previous matrix failures. However, the mode of failure was found to be due to fiber compression, as found in the previous study. Between the first matrix failure and the first fiber failure events, the matrix cracking pattern found was a function of each particular cylinder lay-up. For example, a remarkable amount of cracking occurred in the axially-stiff cylinder as compared to the other two. The study concluded that no leakage path was formed because there was always at least one uncracked layer in each of the cylinders.

The work of McMurray and Hyer sets the stage for the present study. They characterized the matrix failure scenario up to the point where the first fiber failure occurred and found that leakage was unlikely to develop in elliptical composite cylinders without failing some amount of fibers. So if the pressure is increased above the first fiber failure pressure, at some point, leakage will occur, and the pressure and modes of failure involved can be determined. The present study will continue to increase the pressure and determine when a leakage path forms and what modes of failure are involved when leakage occurs. However, a secondary objective of the work here will be to explore several issues that the failure scenarios described by McMurray and Hyer raise. Those issues originate from the fact that the work in [3] used a very specific progressive failure approach. Recall that in [3], the maximum stress failure criterion was used and that the extensional modulus perpendicular to the fibers as well as the inplane shear modulus were reduced, or degraded, by a factor of β=0.2 when matrix tensile failure was detected. Legitimate questions arise naturally as to how the failure scenario for the elliptical cylinders would differ if different failure criteria and other factors of β and degradation schemes were to be used. Would the results

differ if instead of multiplying the elastic moduli by a factor of 0.2, they are multiplied by 0.05, or not reduced at all? After the initial failure is encountered, would degrading the moduli thereafter at each pressure level, thereby representing continuing softening, produce a different result than degrading the moduli only once? What type of impact does the degradation of the inplane shear modulus have on the failure scenario? That is, if the shear modulus is not degraded, but the extensional modulus is, would there be considerably less cracks predicted? Would an interactive failure criterion such as the Hashin or Tsai-Wu criteria predict more failures? If an interactive failure criterion was to predict more matrix cracks, would there still remain an uncracked layer before first fiber failure is detected? To answer these questions, the present work will use a similar approach to the one used in [3], but additional failure criteria and material degradation schemes will be explored and STAGS will be used to perform the progressive failure analysis. However, unlike in [3] that used the STAGS finite-element code to calculate strains, but utilized a stand-alone program to perform the progressive failure analysis, the present work takes advantage of an added capability to STAGS that performs the progressive failure analysis internally. Using STAGS Progressive Failure Analysis (PFA) option, the user can choose from among five failure criteria. The user can also choose from a number of material degradation schemes. It is important to note that some of the algorithms used by STAGS are still in their experimental stage; thus, a third objective to this study is to scrutinize the performance of various algorithms. Specifically, at issue is the order of the computations in the coding within STAGS and whether or not a particular computation can lead to unusually large numbers when moduli are degraded considerably, and whether to degrade engineering properties, which then degrade the stiffness matrix, or whether to directly degrade the stiffness matrix.

The remainder chapters are organized so that the thesis begins by building model complexity and developing an understanding of the PFA in STAGS. This is done by first discussing the manner in which the simple case of a flat plate made of a single-layer of graphite-epoxy material is modeled and handle by STAGS using the PFA, and then by studying a single-layer circular cylinder subjected to an internal radial load. Subsequently, after achieving an adequate understanding of the PFA in STAGS, attention turns to the pressurized elliptical cylinder problem. This is divided into two parts. The first part involves the comparison of matrix cracking scenarios, between the first matrix failure and the first fiber failure events, resulting from using various deg-

radation schemes and then different failure criteria for three different cylinder orthotropies; namely, quasi-isotropic, circumferentially-stiff, and axially-stiff. The different failure criteria to be compared include the maximum stress, Hashin, and Tsai-Wu criteria. In investigating different degradation schemes, only the maximum stress failure criterion is used. The issue of computational algorithms is addressed at this point. The second part of this investigation assesses the pressures beyond fiber failure and modes of failure associated with leakage in each of the cylinders. This second part uses the maximum stress failure criterion and a particular degradation scheme. Finally, conclusions and some final remarks on future work are given.

Chapter 2 Use and Characterization of Computational Analysis Software

STAGS [6] is a finite-element code mainly designed to analyze shell structures. These shells can be modeled in STAGS by specifying geometry, material types, loading conditions, boundary conditions, and finite elements that best describe the physics of a particular problem. Among the materials that can be modeled in STAGS are fiber-reinforced laminated composites. These composites can have up to 100 layers, with each layer having a different fiber orientation. The types of loading that STAGS allows shell models to be subjected to ranges from simple to complex. Simple loadings that include prescribed displacements, point loads, line loads, surface tractions, thermal loads, and pressure loads can be combined to create specific loading requirements. The boundary conditions of a shell structure can be assigned in STAGS by specifying the individual degrees of freedom at a point, line, or surface in a shell unit to be free, fixed, or to have a prescribed value. The geometry of the structural model can be constructed by using a variety of elements from the STAGS element library. Among the standard elements commonly used to construct shell structures, are planar, 4-node quadrilateral plate or curved shells. These shell elements can have four, five, or nine integration points. Some of the standard analysis capabilities of STAGS include static stress, static stability, vibration, and transient analysis. These can include geometric and material nonlinearities. A new additional capability of STAGS is a progressive failure analysis, or PFA. This particular analysis, which includes geometric and material nonlinearities, is used to evaluate failure initiation and progression and is the basis for analyses here.

With the above simplified overview of some of STAGS modeling and analysis capabilities, the next sections will proceed to discuss in detail the specific features that will be used in this study, and also will validate the results of simple problems solved by STAGS.

2.1 STAGS Progressive Failure Analysis

The basic steps of the PFA in STAGS can be summarized as follows: Assuming a general structure in which the displacements at a load step N have already been calculated and equilibrium has been satisfied, begin the next load step. With an extrapolated displacement guess $\{\Delta\}_{i=0}$ from the previous steps, the extrapolated strains and curvatures are calculated at the midsurface of the laminate, $\{\varepsilon^o\}_{i=0}$ and the $\{\kappa^o\}_{i=0}$, respectively. (The first time the analysis is performed, step N=0, a linear analysis is used to find the displacements $\{\Delta\}_{i=0}$ to be used as a guess for step N=1.) The extrapolated strains through the thickness are then computed according to the classical lamination theory,

$$\{\varepsilon\}_{i=0} = \{\varepsilon^o\}_{i=0} + \zeta \{\kappa^o\}_{i=0} \tag{2.1}$$

where ζ is the distance from the midsurface to any location within the laminate. The extrapolated stresses are calculated using these strains and the transformed reduced stiffness matrix from step N,

$$\{\sigma\} = [Q]\{\varepsilon\} \tag{2.2}$$

where Q is the transformed reduced stiffness matrix of the undamaged material. A failure criterion is then evaluated using the extrapolated principal material coordinate system stresses. Because the extrapolated displacements $\{\Delta\}_{i=0}$, and consequently the extrapolated midsurface strains and curvatures are different, perhaps higher, than the ones in step N, the resulting extrapolated stresses may be predicted to cause failures. If this is the case, depending upon the failure criterion used and the mode of failure, the engineering properties are then degraded according to a particular degradation scheme, and a new stiffness matrix, $[Q^d]_{i=0}$ (where d stands for degraded), is formed. (The STAGS analysis offers two options for computing this new stiffness matrix components using the degraded engineering properties. However, a third option, which degrades the components of the stiffness matrix directly, that is, without degrading the engineering properties, is also possible. The details associated with these computational algorithms will be discussed in a later chapter and, as mentioned earlier, their performance evaluated.) After the reduced stiffness matrix is formed, the stresses are recomputed, that is,

$$\{\sigma\}_{i=0} = [Q^d]_{i=0}\{\varepsilon\}_{i=0} \tag{2.3}$$

Also, the first variation of the energy functional, $\{R\}_{i=0}$, is computed using the $[Q^d]_{i=0}$ and $\{\Delta\}_{i=0}$. At this point a Newton-Raphson iteration is performed to determine the second variation or tangent stiffness matrix, $[K_T]_{i=0}$, using $[Q^d]_{i=0}$ and $\{\Delta\}_{i=0}$. With the tangent stiffness matrix, incremental displacements, $\delta\{\Delta\}_{i=0}$, can be found by solving $[K_T]_{i=0}\,\delta\{\Delta\}_{i=0}=-\{R\}_{i=0}$. Then a corrected displacement prediction can be determined by $\{\Delta\}_{i=1} = \{\Delta\}_{i=0} + \delta\{\Delta\}_{i=0}$. The strains and curvatures at the midsurface are recomputed using $\{\Delta\}_{i=1}$ and the strains through the thickness are re-calculated, becoming $\{\varepsilon\}_{i=1}$. New stresses are found using these new strains and the transformed stiffness matrix from step N, $[Q]$. The failure criterion is re-evaluated, the material properties are degraded, and the stiffness matrix is again degraded resulting in a new transformed stiffness matrix, $[Q^d]_{i=1}$. It is important to note that these last steps are necessary to determine the accuracy of the failures predicted using guessed displacements. In other words, it may be found that at the current iteration the displacement solution produce more, less, or no failures with respect to the previous iteration step. If more or less failures are found, it is due to the fact that in the previous iteration a lower or higher estimate of the displacements was made. Therefore, the engineering properties need to be degraded, or reinstated, where appropriate, and the stiffnesses need to be updated. If the solution is not yet converged for i=1, a new iteration is performed (i=2). If no failures are found, then the solution is converged, the stiffness matrix remains $[Q^d]_{i=1}$, and this becomes $[Q]$ (see equation Eq. (2.2)) for the next load step.

In STAGS, the failures due to high stresses can be found by using any of five different failure criteria. They include the maximum stress, Hashin, Tsai-Wu, maximum strain, and Chang-Chang criteria. Though the first three will be used and discussed in later chapters, for a matter of convenience, these three criteria are defined here so that the reader can refer to them through out the remainder of this study. The failure modes for the maximum stress criterion can be written as follows by using STAGS nomenclature and protocol, and considering a state of plane stress:
Fiber tensile failure:

$$\frac{\sigma_1}{X_t} \geq 1 \tag{2.4}$$

Fiber compressive failure:

$$\frac{\sigma_1}{X_c} \leq -1 \tag{2.5}$$

Matrix tensile failure:

$$\frac{\sigma_2}{Y_t} \geq 1 \tag{2.6}$$

Matrix compressive failure:

$$\frac{\sigma_2}{Y_c} \leq -1 \tag{2.7}$$

Inplane shear failure:

$$\frac{|\tau_{12}|}{S_{xy}} \geq 1 \tag{2.8}$$

where,

X_t = tensile strength in the fiber direction

X_c = compressive strength in the fiber direction (a positive number)

Y_t = tensile strength normal to the fiber direction

Y_c = compressive strength normal to the fiber direction (a positive number)

S_{xy} = inplane shear strength

and, σ_1, σ_2, and τ_{12} are the inplane stresses in the usual principal material coordinate system notation. The failure modes for the Hashin criterion are denoted as follows:

Fiber tensile failure:

$$\left(\frac{\sigma_1}{X_t}\right)^2 + \left(\frac{\tau_{12}}{S_{xy}}\right)^2 \geq 1 \tag{2.9}$$

Fiber compressive failure:

$$\frac{\sigma_1}{X_c} \leq -1 \tag{2.10}$$

Matrix tensile failure:

$$\left(\frac{\sigma_2}{Y_t}\right)^2 + \left(\frac{\tau_{12}}{S_{xy}}\right)^2 \geq 1 \tag{2.11}$$

Matrix compressive failure:

$$\left(\frac{\sigma_2}{2S_{xy}}\right)^2 + \left[\left(\frac{Y_c}{2S_{xy}}\right)^2 - 1\right]\frac{\sigma_2}{Y_c} + \left(\frac{\tau_{12}}{S_{xy}}\right)^2 \geq 1 \tag{2.12}$$

Inplane shear failure:

$$\frac{|\tau_{12}|}{S_{xy}} \geq 1 \tag{2.13}$$

The Tsai-Wu failure criterion is defined by

$$F_1\sigma_1 + F_2\sigma_2 + F_{11}\sigma_1^2 + F_{22}\sigma_2^2 + 2F_{12}\sigma_1\sigma_2 + F_{66}\tau_{12}^2 \geq 1 \tag{2.14}$$

where

$$F_1 = \frac{1}{X_t} - \frac{1}{X_c} \qquad F_2 = \frac{1}{Y_t} - \frac{1}{Y_c} \qquad F_{11} = \frac{1}{X_t X_c} \qquad F_{22} = \frac{1}{Y_t Y_c}$$
$$F_{12} = -2\sqrt{F_{11}F_{22}} \qquad F_{66} = \frac{1}{S_{xy}^2} \tag{2.15}$$

For the Tsai-Wu criterion the failure modes are determined as follows:

Fiber tensile and compressive failure is assumed to occur when the following terms dominate:

$$F_1\sigma_1 + F_{11}\sigma_1^2 + F_{12}\sigma_1\sigma_2 \tag{2.16}$$

The sign of σ_1 determines whether failure is due to tension or compression. Matrix tensile or compressive failure is assumed to occur when the following terms dominate:

$$F_2\sigma_2 + F_{22}\sigma_2^2 + F_{12}\sigma_1\sigma_2 \tag{2.17}$$

The sign of σ_2 determines whether failure is due to tension or compression. The inplane shear failure is assumed to occur if the following term, dominates:

$$F_{66}\tau_{12}^2 \tag{2.18}$$

The different standard material degradation schemes that can be adopted by the PFA in STAGS are summarized in Table 2.1 according to failure criteria and mode of failure.

Table 2.1: Standard degradation schemes used by the PFA in STAGS

Failure Criterion	Mode of failure	Engineering properties degraded
maximum stress	fiber tensile and compressive	E_1, G_{12}, ν_{12}, and ν_{21}, or E_1, ν_{12}, and ν_{21}
	matrix tensile and compressive	E_2, G_{12}, ν_{12}, and ν_{21}, or E_2, ν_{12}, and ν_{21}
	inplane shear	G_{12}
Hashin	fiber tensile and compressive	E_1, G_{12}, ν_{12}, and ν_{21}
	matrix tensile and compressive	E_2, G_{12}, ν_{12}, and ν_{21}
	inplane shear	G_{12}
Tsai-Wu	fiber tensile and compressive	E_1, ν_{12}, and ν_{21}
	matrix tensile	E_2, ν_{12}, and ν_{21}
	inplane shear	G_{12}

The amount by which the engineering properties are degraded can vary. When a failure is detected and the failure mode is identified in STAGS, the engineering properties are multiplied by a factor β, where $0 \leq \beta \leq 1$. This factor can be either applied once after the first failure at a point is detected (non-recursive degradation), or the factor can be applied after first fiber failure at a point is detected and at each subsequent load step (recursive degradation). In other words, in a non-recursive degradation scheme, when a failure at a point is first detected at certain load step, the engineering properties are reduced by β only at that step. Thereafter, for subsequent load steps, the degraded properties at that point do not change. In a recursive degradation scheme, for subsequent load steps, the engineering properties are again multiplied by β at each load step. So after the third load step, for example, after failure, the engineering properties would be multiplied by a factor of β^3. It is important to note that, for example, with matrix failure mode, Table 2.1 indicates that E_2, G_{12}, ν_{12}, and ν_{21} are all degraded. The degradation of E_2, ν_{12}, and ν_{21}violates

the well-known reciprocity relation and result in an unsymmetric stiffness matrix. However, STAGS forces the stiffness matrix to be symmetric and E_1 is not degraded.

According to [6], the PFA in STAGS can only be performed on the standard 4-node quadrilateral plane elements from its element library. These elements, as mentioned earlier, can have four, five, or nine integration points in a plane, depending on the user preferences. For a laminated composite, because a single quadrilateral element is generally formed by several layers, the total number of integration points depends on the number of layers and their location within the layers. For a four-layer laminate, for example, assuming that a quadrilateral element with four integration points in a plane is chosen and that planes are located at each layer interface, the element would have a total of 32 integration points. At each one of these points the strains, stresses, and failure criterion involved in the PFA are evaluated. Before applying this analysis to the particular problem to be investigated in this study, the following sections will examine and characterize the PFA in STAGS by analyzing two simple cases.

2.2 Study of Simple Cases

To gain an insight on the actual performance of the PFA capability, a single-layer composite square plate under a tensile inplane load and a single-layer circular cylinder subjected to internal radial load will be studied. Analytical calculations will be used to determine failure loads and displacements for both cases, and these will be compared with the results computed by STAGS.

2.2.1 Single-Layer Square Plate Under Inplane Tensile Loading

The schematic of a perfectly flat plate can be seen in Fig. 2.1. In the figure only the plate's reference surface is depicted. The geometry of the plate is a square of sidelength a and thickness H. The sides of the plate are parallel with the x- and y-directions of an orthogonal coordinate system located at the centroid of the plate. A uniformly distributed tensile load, f, is applied in the y-direction at $y=+a/2$. Also depicted in the figure are the directions of the inplane displacements, u^o and v^o, and normal displacement, w^o, as well as the rotations, ru^o, rv^o, and rw^o, as defined by the con-

ventions used in STAGS. Because of the nature of the formulation of the elements in STAGS, those rotations must also be specified at the boundaries. The boundary conditions at the edges of

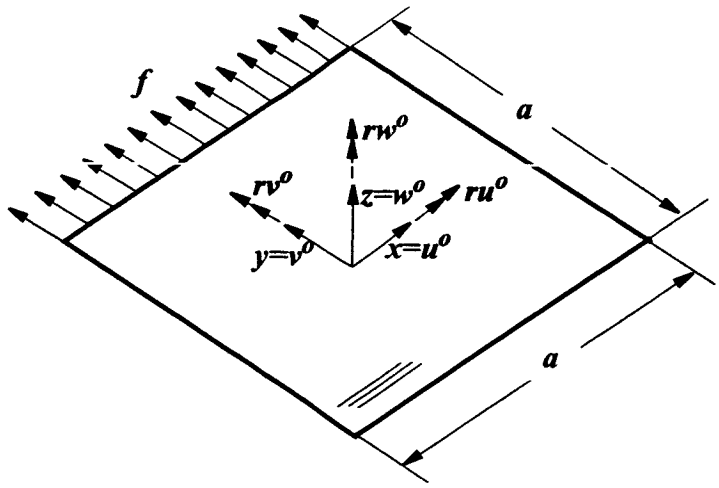

Figure 2.1 Geometry and nomenclature of a square plate reference surface subjected to an inplane tensile loading

the plate are assumed to be as follows:

$$\begin{aligned}
x &= +\frac{a}{2} \qquad u^o = 0,\ w^o = 0, ru^o = 0, rv^o = 0, rw^o = 0, v^o \text{unspecified} \\
x &= -\frac{a}{2} \qquad w^o = 0, ru^o = 0, rv^o = 0, rw^o = 0, u^o \text{and } v^o \text{unspecified} \\
y &= +\frac{a}{2} \quad w^o = 0, ru^o = 0, rv^o = 0, rw^o = 0, N_x = f, u^o \text{and } v^o \text{unspecified} \\
y &= -\frac{a}{2} \qquad v^o = 0,\ w^o = 0, ru^o = 0, rv^o = 0, rw^o = 0, u^o \text{unspecified}
\end{aligned} \tag{2.19}$$

where N_x is the edge stress resultant defined by

$$N_x = \int_{-\frac{H}{2}}^{\frac{H}{2}} \sigma_x dz \tag{2.20}$$

The plate is fabricated of a single-layer of graphite-epoxy with fibers oriented in the direction of the x-coordinate. The fiber direction is indicated in Fig. 2.1 by the three lines near the lower corner of the plate. The engineering properties, failure properties, and the thickness of the single-layer are assumed to be

$$
\begin{aligned}
E_1 &= 18.85 \text{ Msi} \qquad E_2 = 1.407 \text{ Msi} \\
G_{12} &= 0.725 \text{ Msi} \qquad \nu_{12} = 0.300 \qquad h = 0.0055 \text{ inches} \\
X_t &= 200 \text{ ksi} \qquad X_c = 180 \text{ ksi} \\
Y_t &= 7.25 \text{ ksi} \qquad Y_c = 180 \text{ ksi} \\
S_{xy} &= 14.5 \text{ ksi}
\end{aligned}
\tag{2.21}
$$

These properties will be used throughout this study. The side dimension, a, for this problem is 5 in.

The stress-strain relations of this particular orthotropic plate for a state of plane stress can be written as

$$
\begin{Bmatrix} \sigma_x \\ \sigma_y \\ \tau_{xy} \end{Bmatrix} = \begin{bmatrix} Q_{11} & Q_{12} & 0 \\ Q_{12} & Q_{22} & 0 \\ 0 & 0 & Q_{66} \end{bmatrix} \cdot \begin{Bmatrix} \varepsilon_x \\ \varepsilon_y \\ \gamma_{xy} \end{Bmatrix} \tag{2.22}
$$

where Q_{11}, Q_{12}, Q_{22}, and Q_{66}, are the reduced stiffnesses, which in terms of engineering properties, are given by

$$
\begin{aligned}
Q_{11} &= \frac{E_1}{1 - \nu_{12} \cdot \nu_{21}} \\
Q_{12} &= \frac{E_2 \cdot \nu_{12}}{1 - \nu_{12} \cdot \nu_{21}} \\
Q_{22} &= \frac{E_2}{1 - \nu_{12} \cdot \nu_{21}} \\
Q_{66} &= G_{12}
\end{aligned}
\tag{2.23}
$$

It is important to emphasize that due to the orthotropic nature of the material, $\nu_{12} \neq \nu_{21}$. In fact, these ratios are related by the reciprocity relationship,

$$
\frac{E_1}{\nu_{12}} = \frac{E_2}{\nu_{21}} \tag{2.24}
$$

In Eq. (2.22), the only nonzero stress is the stress in the direction of the load, the y-direction. The stress in the fiber direction, σ_x, is zero because the plate is free to contract, due to the Poisson effect, in that direction. The shear stress, τ_{xy}, in the other hand, is zero because the uniform char-

acter of the applied load causes no shear deformation. Within the context of simple plate theory, the displacements at any point within the plate can be expressed as follows:

$$\begin{aligned} u(x,y,z) &= u^o(x,y) - z\, ru^o(x,y) \\ v(x,y,z) &= v^o(x,y) - z\, rv^o(x,y) \\ w(x,y,z) &= w^o(x,y) \end{aligned} \tag{2.25}$$

The above equation can be simplified by the facts that the plate is assumed to be perfectly flat before and during loading, and that the load is uniform and unidirectional. In other words, due to the transverse displacement, w, being zero everywhere in the plate, the only displacements to be consider are u and v. In addition, because the load is uniformly applied in the y-direction, the u-displacement is only a function of x and the v-displacement is only a function of y. As a consequence of these assumptions, the displacements in Eq. (2.25) reduce to

$$\begin{aligned} u(x,y,z) &= u^o(x) \\ v(x,y,z) &= v^o(y) \\ w(x,y,z) &= w^o(x,y) = 0 \end{aligned} \tag{2.26}$$

The complete nonlinear strain-displacement relations for the reference surface are given by

$$\begin{aligned} \varepsilon_x(x,y) &= \frac{\partial u^o}{\partial x} + \frac{1}{2}\left[\left(\frac{\partial u^o}{\partial x}\right)^2 + \left(\frac{\partial v^o}{\partial x}\right)^2 + \left(\frac{\partial w^o}{\partial x}\right)^2\right] \\ \varepsilon_y(x,y) &= \frac{\partial v^o}{\partial y} + \frac{1}{2}\left[\left(\frac{\partial u^o}{\partial y}\right)^2 + \left(\frac{\partial v^o}{\partial y}\right)^2 + \left(\frac{\partial w^o}{\partial y}\right)^2\right] \\ \gamma(x,y) &= \frac{1}{2}\left[\frac{\partial u^o}{\partial y} + \frac{\partial v^o}{\partial x} + \frac{\partial u^o}{\partial x}\frac{\partial u^o}{\partial y} + \frac{\partial v^o}{\partial x}\frac{\partial v^o}{\partial y} + \frac{\partial w^o}{\partial x}\frac{\partial w^o}{\partial y}\right] \end{aligned} \tag{2.27}$$

If all of the assumptions discussed above are considered, the strain-displacement relations become

$$\begin{aligned} \varepsilon_x(x) &= \frac{du^o}{dx} + \frac{1}{2}\left(\frac{du^o}{dx}\right)^2 \\ \varepsilon_y(y) &= \frac{dv^o}{dy} + \frac{1}{2}\left(\frac{dv^o}{dy}\right)^2 \\ \gamma(x,y) &= 0 \end{aligned} \tag{2.28}$$

If σ_y from Eq. (2.22) is substituted into the total potential energy of the plate, the total potential energy is given by

$$\Pi = \frac{1}{2}\int_{-\frac{H}{2}}^{\frac{H}{2}}\int_{-\frac{a}{2}}^{\frac{a}{2}}\int_{-\frac{a}{2}}^{\frac{a}{2}} \sigma_y \varepsilon_y dx dy dz - P v^o\left(\frac{a}{2}\right) \tag{2.29}$$

where $P = f \cdot a$, gives the following

$$\Pi = \frac{1}{2}\int_{-\frac{H}{2}}^{\frac{H}{2}}\int_{-\frac{a}{2}}^{\frac{a}{2}}\int_{-\frac{a}{2}}^{\frac{a}{2}} (Q_{12} \cdot \varepsilon_x + Q_{22} \cdot \varepsilon_y)\varepsilon_y dx dy dz - P v^o\left(\frac{a}{2}\right) \tag{2.30}$$

The strains ε_x and ε_y can be related by σ_x which, as mentioned previously, is zero. Thus, from the first equation of Eq. (2.22),

$$\varepsilon_x = -\frac{Q_{12}}{Q_{11}} \cdot \varepsilon_y \tag{2.31}$$

If this strain is substituted into Eq. (2.30), and since ε_y is only a function of y, the total potential energy of the plate can be expressed as

$$\Pi = \frac{1}{2} H \cdot a \cdot \left(\frac{Q_{22} \cdot Q_{11} - Q_{12}^2}{Q_{11}}\right)\int_{-\frac{a}{2}}^{\frac{a}{2}} \varepsilon_y{}^2 dy - P v^o\left(\frac{a}{2}\right) \tag{2.32}$$

The first variation of Eq. (2.32) is given by

$$\delta\Pi = H \cdot a \cdot \left(\frac{Q_{22} \cdot Q_{11} - Q_{12}^2}{Q_{11}}\right)\int_{-\frac{a}{2}}^{\frac{a}{2}} (\varepsilon_y \cdot \delta\varepsilon_y) dy - P\delta v^o\left(\frac{a}{2}\right) \tag{2.33}$$

In terms of displacement gradients, the first variation can be written as

$$\delta\Pi = H \cdot a \cdot \left(\frac{Q_{22} \cdot Q_{11} - Q_{12}^2}{Q_{11}}\right)\int_{-\frac{a}{2}}^{\frac{a}{2}} \left(\left(\frac{dv^o}{dy} + \frac{1}{2}\left(\frac{dv^o}{dy}\right)^2\right) \cdot \delta\left(\frac{dv^o}{dy} + \frac{1}{2}\left(\frac{dv^o}{dy}\right)^2\right)\right) dy - P\delta v^o\left(\frac{a}{2}\right) \tag{2.34}$$

The variation of $\left(\frac{dv^o}{dy} + \frac{1}{2}\left(\frac{dv^o}{dy}\right)^2\right)$ and integration by parts of Eq. (2.34) results in

$$\begin{aligned}\delta\Pi = {} & H \cdot a \cdot \left(\frac{Q_{22} \cdot Q_{11} - Q_{12}^2}{Q_{11}}\right)\left\{\left\{\left(\frac{dv^o}{dy} + \frac{1}{2}\left(\frac{dv^o}{dy}\right)^2\right)\left(1 + \frac{dv^o}{dy}\right)\right\}\delta v^o\Big|_{-\frac{a}{2}}^{\frac{a}{2}}\right\} - P\delta v^o\left(\frac{a}{2}\right) \\ & - \int_{-\frac{a}{2}}^{\frac{a}{2}} H \cdot a \cdot \left(\frac{Q_{22} \cdot Q_{11} - Q_{12}^2}{Q_{11}}\right)\frac{d}{dy}\left\{\left(\frac{dv^o}{dy} + \frac{1}{2}\left(\frac{dv^o}{dy}\right)^2\right)\left(1 + \frac{dv^o}{dy}\right)\right\}\delta v^o dy\end{aligned} \tag{2.35}$$

Setting the first variation to zero yields the Euler-Lagrange equation for v^o, and the corresponding variationally consistent boundary conditions at $y=\pm a/2$. That is,

$$H \cdot a \cdot \left(\frac{Q_{22} \cdot Q_{11} - Q_{12}^2}{Q_{11}} \right) \frac{d}{dy} \left\{ \left(\frac{dv^o}{dy} + \frac{1}{2} \left(\frac{dv^o}{dy} \right)^2 \right) \left(1 + \frac{dv^o}{dy} \right) \right\} = 0 \tag{2.36}$$

and using the fact that $\delta v^o\left(-\frac{a}{2}\right) = 0$, since $v^o\left(-\frac{a}{2}\right)$ is known,

$$H \cdot a \cdot \left(\frac{Q_{22} \cdot Q_{11} - Q_{12}^2}{Q_{11}} \right) \left(\frac{dv^o}{dy} + \frac{1}{2} \left(\frac{dv^o}{dy} \right)^2 \right) \left(1 + \frac{dv^o}{dy} \right) = P \tag{2.37}$$

Equation Eq. (2.36) indicates that the expression in braces is constant. From Eq. (2.37), the value of that constant can be determined and the equation can be written

$$\left(\frac{dv^o}{dy} + \frac{1}{2} \left(\frac{dv^o}{dy} \right)^2 \right) \left(1 + \frac{dv^o}{dy} \right) = \frac{P}{H \cdot a \cdot \left(\frac{Q_{22} \cdot Q_{11} - Q_{12}^2}{Q_{11}} \right)} = \frac{P}{H \cdot a \cdot E_2} \tag{2.38}$$

The above expression is a cubic equation in dv^o/dy that can be solved at any load P. If the solution to Eq. (2.38) is denoted as $dv^o/dy=f(P)$, and this displacement gradient is integrated with respect to y, then the displacement v^o at any y-location for any load P is found by

$$v^o = f(P)y + C_1 \tag{2.39}$$

where C_1 is a constant of integration to be solved by applying the displacement boundary condition on v^o at $y=-a/2$. Enforcement of Eq. (2.19), results in

$$v^o = f(P)\left(y + \frac{a}{2} \right) \tag{2.40}$$

To find the u^o-displacement, Eq. (2.28) and Eq. (2.31) or Eq. (2.38) can first be used to relate the displacement gradients by the following equation

$$\frac{du^o}{dx} + \frac{1}{2} \left(\frac{du^o}{dx} \right)^2 = -\frac{Q_{12}}{Q_{11}} \cdot \left(\frac{dv^o}{dy} + \frac{1}{2} \left(\frac{dv^o}{dy} \right)^2 \right) = -\frac{\nu_{21}}{E_2} \cdot \frac{P}{H \cdot a} \cdot \frac{1}{\left(1 + \frac{dv^o}{dy} \right)} \tag{2.41}$$

If the value of dv^o/dy found in Eq. (2.38) is used in Eq. (2.41), the axial displacement gradient, du^o/dx, can then be computed. Referring to the solution of Eq. (2.41) as $du^o/dx=g(P)$, integrating this gradient with respect to x, and applying the displacement boundary condition on u^o at $x=+a/2$, the u^o-displacement is found to be

$$u^o = g(P)\left(x - \frac{a}{2}\right) \tag{2.42}$$

To calculate the load at which the plate will fail due to excessive tensile stress perpendicular to the fibers, the stress σ_y in Eq. (2.22) is substituted by its allowable strength, Y_t, resulting in

$$Y_t = Q_{12} \cdot \varepsilon_{xt} + Q_{22} \cdot \varepsilon_{yt} \tag{2.43}$$

where the subscript t indicates failure value due to tension. Substituting Eq. (2.31) and Eq. (2.28) into Eq. (2.43) gives

$$Y_t = \frac{Q_{11} \cdot Q_{22} - Q_{12}^2}{Q_{11}} \cdot \left(\left(\frac{dv^o}{dy}\right)_t + \frac{1}{2} \cdot \left(\frac{dv^o}{dy}\right)_t^2\right) \tag{2.44}$$

Recognition of the right hand side of Eq. (2.44) in Eq. (2.37), and substitution of the right hand side for Y_t from Eq. (2.44), the failure load is found to be, from Eq. (2.37),

$$P_t = H \cdot a \cdot Y_t \cdot \left(1 + \left(\frac{dv^o}{dy}\right)_t\right) \tag{2.45}$$

The displacement gradient at failure, $(dv^o/dy)_t$, is computed using equation Eq. (2.44).

To complete the objective of this simple problem, which was to compare STAGS results with the above analytical solutions, as well as to understand the PFA, numerical results for the displacements v^o and u^o were obtained by modeling the square plate with a finite-element mesh composed of a total of 25 quadrilateral elements using the E410 quadrilateral shell element from STAGS element library. Each element was assigned with four integration points in a plane located at the top and bottom of the layer, for a total of eight integration points per element. A line load was applied at one of the edges of the mesh and boundary conditions were set so that they were consistent with the constraints given in Eq. (2.19). A nonlinear analysis with the PFA capability was performed. The PFA was directed to use the maximum stress failure criterion and to multiply E_2, G_{12}, ν_{12}, and ν_{21} non-recursively by a factor of β=0.2 for matrix tensile failure

mode. In the STAGS analysis, the load was increased from zero in steps of 20 lbs, except near the expected failure load, where the load increments were of 0.1 lbs. The load steps were increased up to a load well beyond the value to cause the failure of the plate. From a physical point of view, there is no meaning for the results obtained after the plate failed, since for this problem every element had failed and the plate can not longer carry any additional load. However, for the purpose of understanding the PFA in STAGS, the results beyond failure, particularly the increased strains and displacements, were of interest as they led to a further understanding of how STAGS works.

The plate modeled in STAGS failed at about 200.4 lbs due to matrix tension failure. The analytical failure load predicted by Eq. (2.45) was found to be precisely that value. Figures 2.2 and 2.3 show the comparison between analytical (solid line) and STAGS numerical (triangular symbols) displacements v^o and u^o at particular locations in the plate and at certain load steps. Specifically, the figures show the v^o-displacement at the edge $y=+a/2$ and the u^o-displacement at the edge $x=-a/2$ for loads ranging from 100 to 260 lbs. Although the loads were increased from zero, only loads above 100 lbs are shown because more significant displacements began to take place at these load levels. From both figures can be seen that there is excellent agreement between the analytical solution and STAGS results.

In Fig. 2.2 it is shown that the v^o-displacement increases with increasing load. This is expected since the free edge of the plate is being stretched more and more with increasing load. At the failure load, it can be observed that the load-v^o-displacement relation exhibits a discontinuity. This jump is due to the sudden reduction of the extensional modulus E_2 by a factor of β=0.2 when failure is encountered. Note that at the failure load, E_2 in Eq. (2.38) is multiplied by β, causing the displacement gradient dv^o/dy to change suddenly by certain amount. As a result of that change, the v^o-displacement in Eq. (2.39) experiences a jump at the failure load. After that jump, the magnitude of the v^o-displacements are in the order of 10^{-1} inches; while, before the failure, the magnitude of the displacements are in the order of 10^{-2} inches. Also in Fig. 2.2, it can be observed that after failure, the slope of the load-v^o-displacement curve has changed. This change in slope can be attributed to the fact that, before failure, the stress σ_y and strain ε_y and, therefore, the load and v^o-

displacement, are related by the original value of the extensional modulus, E_2. After the failure, however, those parameters are related by the reduced extensional modulus, βE_2.

Figure 2.3 shows that the u^o-displacement of the edge that is free to contract due to Poisson's effect increases with increasing load. This behavior is typical of a material that is being stretched more and more as it is pulled in one direction, causing a larger and larger contraction perpendicular to the direction of the pull. The fact that the u^o-displacements in the figure are positive indicate that the free edge moves in the positive direction toward the fixed edge. The small discontinuity in the load-u^o-displacement curve which can be observed in the figure is associated with the change in the displacement gradient dv^o/dy mentioned above. Note that since immediately after failure E_2 is multiplied by β and ν_{21} is also multiplied by β, to maintain the reciprocity relation of Eq. (2.24), the term dv^o/dy in the denominator in the right hand side of Eq. (2.41) is the only term responsible for the sudden change in du^o/dx, which in turn produces the discontinuity in the load-u^o-displacement curve at the failure load. The magnitude of the u^o-displacements are in the order of 10^{-4} inches.

From this simple case of a single-layer square plate under inplane tensile loading, it was determined that the numerical results given by STAGS and its PFA capability are in good agreement with the analytical solutions described. The errors in the results, which were found to be insignificant, are believed to be due to the computational algorithm, which is generally expected of finite-element codes. In the next section, a slightly more complicated case with different geometry and loading will be study analytically and using STAGS.

2.2.2 Internal Radial Loading of a Single-Layer Circular Cylinder

Seen in Fig. 2.4 is a diagram describing the next problem designed to study the PFA option in STAGS. The geometry of the reference surface of a single-layer circular cylinder of radius R and length L subjected to a uniformly distributed radial load, denoted by p_o, is depicted. A global reference system is located at the geometric center of the cylinder. The coordinate ζ is measured

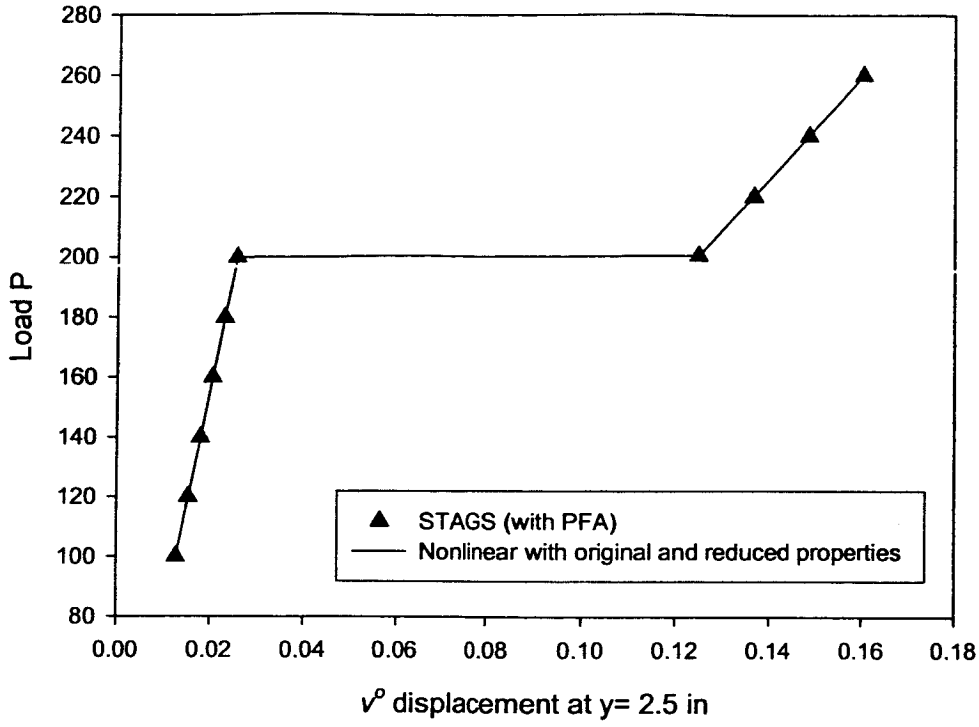

Figure 2.2 Applied inplane load vs. v^o-displacement at $y=+a/2$

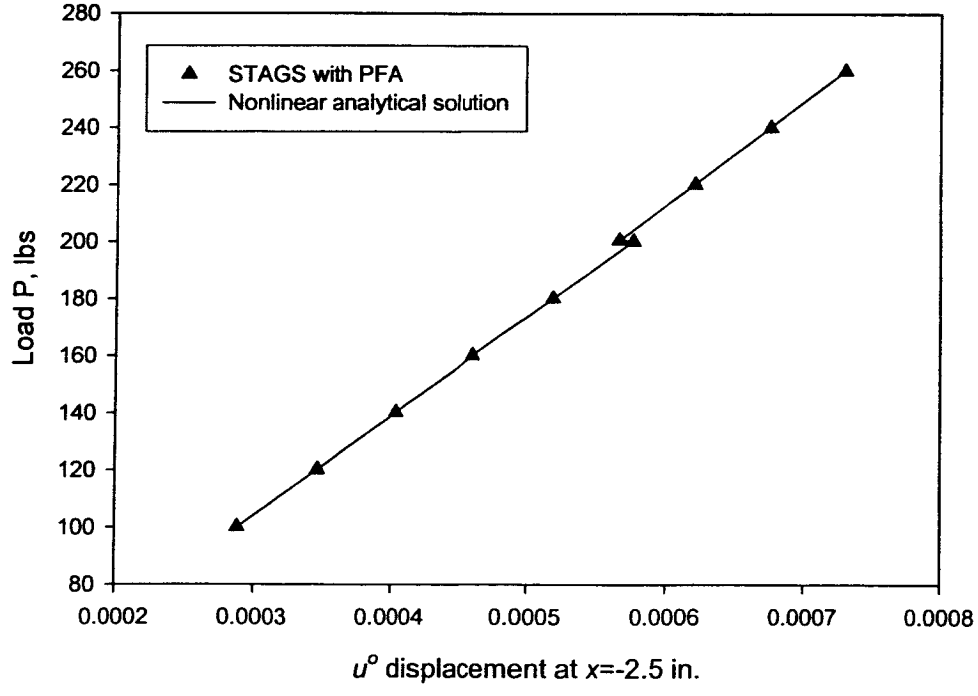

Figure 2.3 Applied inplane load vs. u^o-displacement at $x=-a/2$

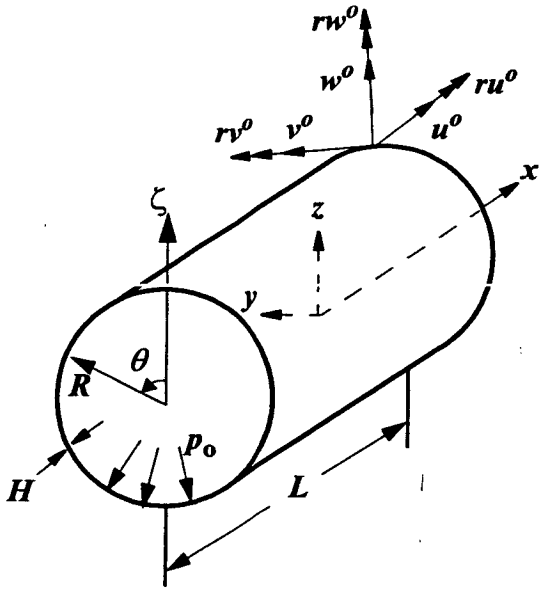

Figure 2.4 Geometry and nomenclature of a circular cylinder reference surface subjected to an internal radial loading

from the middle of the single-layer, like z in Fig. 2.1. The axial, tangential, and outward displacement directions are indicated by u^o, v^o, and w^o, respectively. The boundary conditions are given by

$$\begin{aligned} x &= -\frac{L}{2} \qquad u^o = 0,\ ru^o = 0,\ rv^o = 0,\ v^o,\ w^o, \text{ and } rw^o \text{ unspecified} \\ x &= +\frac{L}{2} \qquad ru^o = 0,\ rv^o = 0,\ u^o,\ v^o,\ w^o, \text{ and } rw^o \text{ unspecified} \end{aligned} \tag{2.46}$$

Because of the formulation of the element in STAGS, the following other conditions were imposed:

$$\begin{gathered} u^o, w^o, rv^o \text{ and } rw^o \text{ unspecified everywhere else} \\ ru^o = 0 \text{ everywhere} \\ v^o = 0 \text{ at specific locations to prevent rigid body motion} \end{gathered} \tag{2.47}$$

The cylinder is made of a single-layer of graphite-epoxy, with the same material properties and thickness as in the previous case. A list of those was given in Eq. (2.21). The radius of the cylinder is 5 inches and the length is 12.5 inches.

If a state of plane stress is assumed, as it was done for the case of the plate, Eq. (2.22) through Eq. (2.24) remain valid for this case. Within the context of simple cylinder theory, the three components of the displacement, analogous with Eq. (2.25), can be written as

$$\begin{aligned} u(x,\theta,\zeta) &= u^o(x,\theta) - \zeta\, r u^o(x,\theta) \\ v(x,\theta,\zeta) &= v^o(x,\theta) - \zeta\, r v^o(x,\theta) \\ w(x,\theta,\zeta) &= w^o(x,\theta) \end{aligned} \tag{2.48}$$

With boundary conditions, Eq. (2.46), this circular cylinder under the uniform loading p_o is free to expand in the outward direction, is free to contract axially, and the response of the cylinder is expected to be axisymmetric. Therefore, the following assumptions can be made.

$$\begin{aligned} v(x,\theta,\zeta) &= 0 \\ \frac{\partial}{\partial\theta}(\ ) &= 0 \\ \frac{\partial}{\partial x}(\ ) &= \frac{d}{dx}(\ ) \end{aligned} \tag{2.49}$$

Simplifications of Eq. (2.48) can be made by using Eq. (2.49). As a result, Eq. (2.48) reduces to

$$\begin{aligned} u(x,\theta,\zeta) &= u^o(x) \\ v(x,\theta,\zeta) &= 0 \\ w(x,\theta,\zeta) &= w^o(\text{a constant}) \end{aligned} \tag{2.50}$$

The complete nonlinear strain-displacement relations for the reference surface in cylindrical coordinates are derived from [9]

$$\begin{aligned} \varepsilon_x(x,\theta) &= \frac{\partial u^o}{\partial x} + \frac{1}{2}\left[\left(\frac{\partial u^o}{\partial x}\right)^2 + \left(\frac{\partial v^o}{\partial x}\right)^2 + \left(\frac{\partial w^o}{\partial x}\right)^2\right] \\ \varepsilon_\theta(x,\theta) &= \frac{1}{R}\frac{\partial v^o}{\partial\theta} + \frac{w^o}{R} + \frac{1}{2}\left[\left(\frac{1}{R}\frac{\partial u^o}{\partial\theta}\right)^2 + \left(\frac{1}{R}\frac{\partial v^o}{\partial\theta} + \frac{w^o}{R}\right)^2 + \left(\frac{1}{R}\frac{\partial w^o}{\partial\theta} - \frac{v^o}{R}\right)^2\right] \\ \gamma_{x\theta}(x,\theta) &= \frac{1}{2}\left[\frac{1}{R}\frac{\partial u^o}{\partial\theta} + \frac{\partial u^o}{\partial x}\left(\frac{1}{R}\frac{\partial u^o}{\partial\theta}\right) + \frac{\partial v^o}{\partial x} + \frac{\partial v^o}{\partial x}\left(\frac{1}{R}\frac{\partial v^o}{\partial\theta} + \frac{w^o}{R}\right) + \frac{\partial w^o}{\partial x}\left(\frac{1}{R}\frac{\partial w^o}{\partial\theta} - \frac{v^o}{R}\right)\right] \end{aligned} \tag{2.51}$$

If Eq. (2.50) is substituted into Eq. (2.51), the reference surface strains simplify to

$$\begin{aligned} \varepsilon_x(x,\theta) &= \frac{du^o}{dx} + \frac{1}{2}\left(\frac{du^o}{dx}\right)^2 \\ \varepsilon_\theta(x,\theta) &= \frac{w^o}{R} + \frac{1}{2}\left(\frac{w^o}{R}\right)^2 \\ \gamma_{x\theta}(x,\theta) &= 0 \end{aligned} \tag{2.52}$$

Since the only nonzero stress is the circumferential stress, σ_θ, the total potential energy for the radially loaded circular cylinder is given as [10]

$$\Pi = \frac{1}{2}\int_{-\frac{H}{2}}^{\frac{H}{2}}\int_0^{2\pi}\int_{-\frac{L}{2}}^{\frac{L}{2}} \sigma_\theta \varepsilon_\theta dx R d\theta d\zeta - \pi \int_{-\frac{L}{2}}^{\frac{L}{2}} p_o\left(w^o R + \frac{1}{2}w^{o2}\right)dx \tag{2.53}$$

The circumferential stress, σ_θ, in Eq. (2.53) can be written in terms of strains using the second equation in Eq. (2.22), with the appropriate coordinate change. This results in

$$\Pi = \pi \int_{-\frac{H}{2}}^{\frac{H}{2}}\int_{-\frac{L}{2}}^{\frac{L}{2}} (Q_{12}\cdot\varepsilon_x + Q_{22}\cdot\varepsilon_\theta)\varepsilon_\theta \cdot R dx d\zeta - \pi \int_{-\frac{L}{2}}^{\frac{L}{2}} 2p_o\left(w^o R + \frac{1}{2}w^{o2}\right)dx \tag{2.54}$$

Since σ_x is zero, the cylinder is free to contract axially as it expands outward. Thus ε_x is related to the circumferential stress ε_θ by

$$\varepsilon_x = -\frac{Q_{12}}{Q_{11}}\cdot\varepsilon_\theta \tag{2.55}$$

Substitution of Eq. (2.55) into Eq. (2.54) and use of the fact that the circumferential strain is not a function of ζ, allow Eq. (2.54) to be rewritten as

$$\Pi = \pi \int_{-\frac{L}{2}}^{\frac{L}{2}} \left\{ H\left(\frac{Q_{22}\cdot Q_{11} - Q_{12}^2}{Q_{11}}\right) R\varepsilon_\theta^2 - 2p_o\left(w^o R + \frac{1}{2}w^{o2}\right)\right\} dx \tag{2.56}$$

The first variation of the total potential energy is given by

$$\delta\Pi = \pi \int_{-\frac{L}{2}}^{\frac{L}{2}} \left\{ 2H\left(\frac{Q_{22}\cdot Q_{11} - Q_{12}^2}{Q_{11}}\right) R\varepsilon_\theta \delta\varepsilon_\theta - 2p_o(R + w^o)\delta w^o \right\} dx \tag{2.57}$$

If the circumferential strain in Eq. (2.57) is expressed in terms of the outward displacement, as in Eq. (2.52), and the second term is rearranged, the first variation becomes

$$\delta\Pi = \pi\int_{-\frac{L}{2}}^{\frac{L}{2}}\left\{2H\left(\frac{Q_{22}\cdot Q_{11}-Q_{12}^2}{Q_{11}}\right)\left(\frac{w^o}{R}+\frac{1}{2}\left(\frac{w^o}{R}\right)^2\right)\left(1+\frac{w^o}{R}\right)\delta w^o - 2p_oR\left(1+\frac{w^o}{R}\right)\delta w^o\right\}dx \quad (2.58)$$

If the first variation is set to zero, the following Euler-Lagrange equation is found:

$$\frac{w^o}{R}+\frac{1}{2}\left(\frac{w^o}{R}\right)^2 = \frac{p_oR}{H\left(\frac{Q_{22}\cdot Q_{11}-Q_{12}^2}{Q_{11}}\right)} = \frac{p_oR}{H\cdot E_2} \quad (2.59)$$

Equation (2.59) is an algebraic equation which allows for the determination of the outward displacement as a function of the internal load. To find the axial displacement, u^o, as a function of the axial coordinate and the internal pressure, Eq. (2.55) expressed in terms of displacements can be used. That is,

$$\frac{du^o}{dx}+\frac{1}{2}\left(\frac{du^o}{dx}\right)^2 = -\frac{Q_{12}}{Q_{11}}\left(\frac{w^o}{R}+\frac{1}{2}\left(\frac{w^o}{R}\right)^2\right) = -\nu_{21}\cdot\left(\frac{w^o}{R}+\frac{1}{2}\left(\frac{w^o}{R}\right)^2\right) \quad (2.60)$$

The Euler-Lagrange equation found in Eq. (2.59) can be used to rewrite the above equation as

$$\frac{du^o}{dx}+\frac{1}{2}\left(\frac{du^o}{dx}\right)^2 = \frac{-p_oRQ_{12}}{H(Q_{22}\cdot Q_{11}-Q_{12}^2)} = -\frac{\nu_{21}}{E_2}\cdot\frac{p_oR}{H} \quad (2.61)$$

From this equation, the displacement gradient, du^o/dx, can be computed and used to determine the axial displacement, u^o. If the solution to Eq. (2.61) is denoted as $du^o/dx=h(p_o)$, this displacement gradient integrated with respect x, and u^o is set to be zero at $x=-L/2$, according to Eq. (2.46), the axial displacement at any axial location and at any load level is given by

$$u^o = h(p_o)\left(x+\frac{L}{2}\right) \quad (2.62)$$

The load at which the cylinder is expected to fail occurs when the stress in the circumferential direction reaches the allowable stress. Mathematically, this is equivalent to writing

$$Y_t = Q_{12}\cdot\varepsilon_{xt}+Q_{22}\cdot\varepsilon_{\theta t} \quad (2.63)$$

where again the subscript t in the strains indicates failure values due to tension. Equation (2.55) and Eq. (2.52) can be used to write the axial strain in terms of the circumferential strain and the circumferential strain in terms of outward displacement, respectively. Thus, the above equation yields

$$Y_t = \left(\frac{Q_{22} \cdot Q_{11} - Q_{12}^2}{Q_{11}}\right)\left(\frac{w^o}{R} + \frac{1}{2}\left(\frac{w^o}{R}\right)^2\right) \tag{2.64}$$

Substitution of the second factor in Eq. (2.64), which was evaluated by the Euler-Lagrange equation, Eq. (2.59), allows for the solution of the failure load in terms of the allowable strength. That is,

$$p_{ot} = \frac{Y_t \cdot H}{R} \tag{2.65}$$

STAGS numerical results for the failure load and the outward and axial displacements for this case were obtained by constructing a finite-element mesh of the circular cylinder composed of 10 elements in the circumferential direction by 30 elements in the axial direction. The type of elements used was the E410 quadrilateral shell element with four integration points at the top and bottom of the layer, for a total of eight integration points. An internal radial loading was applied and boundary conditions were set so that no rigid body motion was allowed and the cylinder was free to expand outwardly and one end of the cylinder was free to contract axially. The load was increased from zero up to 13 psi in steps of 2 psi, except near the expected failure load, where the load was increased in steps of 0.1 psi or less. As in the case of the plate problem, the load was increased above the failure load only to characterize STAGS PFA capability, since, physically, this cylinder would lose its structural integrity as soon as the failure load is reached. The settings used in the PFA were the same as in the previous plate case. That is, failure was determined using the maximum stress failure criterion and the degradation scheme used reduced non-recursively the elastic moduli E_2, G_{12}, ν_{12}, and ν_{21} by β=0.2 for matrix tensile failure mode.

The axial, circumferential, and outward displacements were recorded for each node at each load step. Figures 2.5 and 2.6 show the load vs. the outward displacement, w^o, for any axial location (red triangular symbols), and the axial displacement, u^o, at the free end of the cylinder (blue triangular symbols), respectively. The circumferential displacement was not plotted since, as expected, due to the axisymmetry of the problem, it was zero. Shown in the figures are also the analytical solutions for the displacements at each load level (solid line). As it can be observed from the figures, analytical solutions and STAGS results are in close agreement.

Figure 2.5 shows that the outward displacement, w^o, increases as the internal load is increased. Also shown in Fig. 2.5 is that at the failure load, a discontinuity in the outward displacement occurs. The change in displacement is directly associated with the fact that the degradation experienced by the extensional modulus, βE_2, at the failure load produces an abrupt change in the in circumferential strain. This sudden rise in strain causes the displacement w^o to also increase abruptly by the second strain-displacement relation in Eq. (2.52). The magnitude of the normal displacements after failure are in the order of 10^{-1} inches, while the magnitude of these displacements before failure are in the order of 10^{-2} inches. Another observation that can be made from the load-displacement curve in Fig. 2.5 is the change in its rate of increase before and after the failure load. The cause of this change can be attributed directly to the degradation of E_2. Before the failure load is reached, the extensional modulus in the load-displacement relation given in Eq. (2.59) has its original value. This results in particular values of w^o-displacements that increase at a certain rate with the load. Immediately after the failure load is reached, E_2 is reduced by the factor β. As a result, the outward displacements increases at a lower rate with load.

In Fig. 2.6, it is seen that the magnitude of the u^o-displacement increases with increasing load. The negative signs indicate that at a given load the cylinder's free end moved toward the other end, which is fixed axially. The increased shortening of the cylinder is the result of the Poisson's effect becoming larger, as higher loads force the cylinder to expand more in the outward direction. This situation is analogous to the one in the previous case in which the plate experienced a larger and larger contraction in one direction as it was pulled more and more in the transversal direction. One interesting observation that can be made in Fig. 2.6 is that unlike the u^o-displacement in the plate problem, the axial displacement is continuous. To see why this is the case, Eq. (2.61) should be carefully examined. Immediately after failure, E_2 and ν_{21} are multiplied by β. This causes the β's to cancel from Eq. (2.61). Therefore, the right hand side of the equation remains constant, and consequently the solution to the equation $du^o/dx=h(p_o)$ also remains constant.

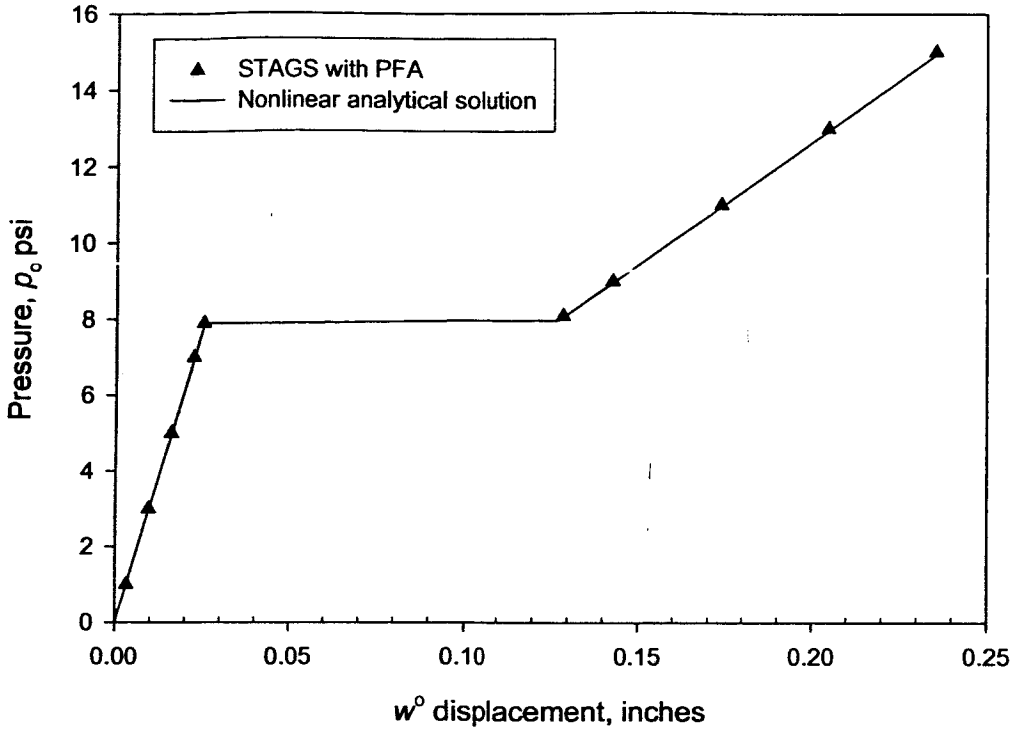

Figure 2.5 Internal radial load vs. outward displacement at any axial location

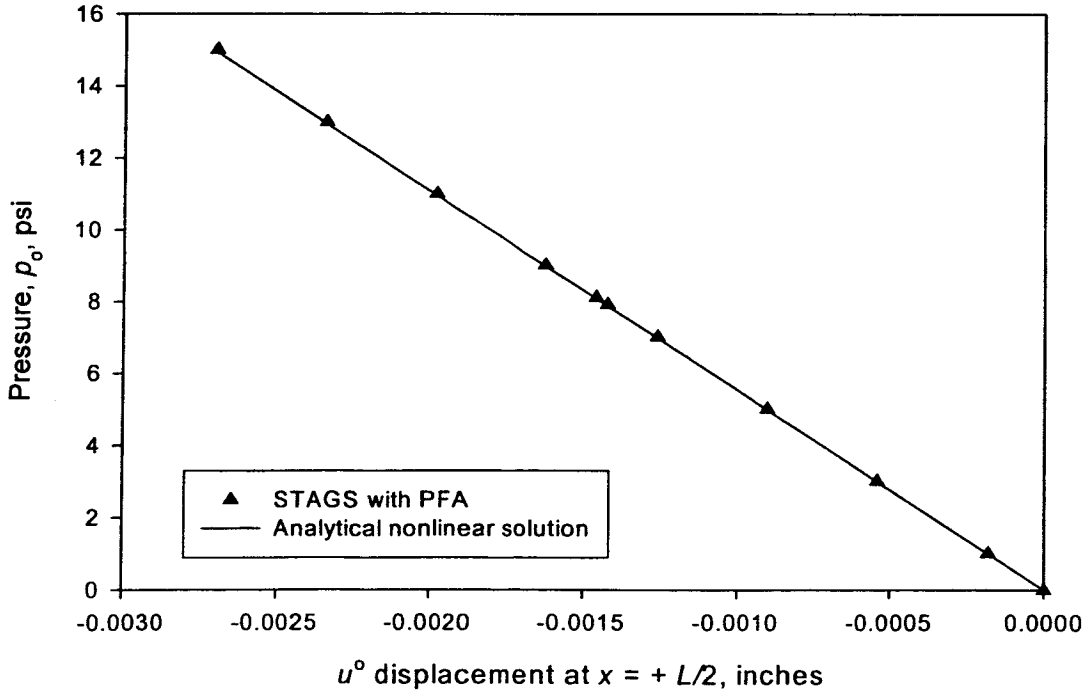

Figure 2.6 Internal radial load vs. axial displacement at x=+$L/2$

2.3 Summary

In this chapter the basic features of the finite-element code STAGS which will be used throughout the remainder of this study have been introduced. It was indicated that this code is generally used to perform stress analysis in thin shells. The specific feature, the PFA option, in STAGS was particularly discussed in detail. In the discussion, it was pointed out that the PFA capability allows an analysis of failure initiation and progression in a given structure. This type of problem forms the basis of the study to be presented in this work.

Chapter 3 Matrix Failure Scenarios in Internally Pressurized Elliptical Cylinders Using Different Degradation Schemes

In this chapter the effects of different degradation schemes on the matrix failure scenarios for an internally pressurized, elliptical, composite cylinder with different material orthotropy will be investigated. As mentioned in the introduction, a secondary objective of this study is to answer some of the questions raised by the work of McMurray and Hyer [3]. Recall that in their study they used a progressive failure analysis to study failure of an internally pressurized, elliptical, composite cylinder with quasi-isotropic, circumferentially-stiff, and axially-stiff material orthotropies. In their progressive failure methodology, they used the maximum stress failure criterion and a degradation scheme that reduced the extensional modulus perpendicular to the fibers and the inplane shear modulus by 80% when matrix tensile failure was encountered. Coincidently, up to the pressure levels they considered, only matrix tensile failures were encountered. The fact that McMurray and Hyer used such a specific failure criterion and degradation scheme prompted several questions in regard to how their failure predictions would change if other criteria and degradation schemes were used. Specifically, the chapter will address the following questions: What is the effect of degrading the inplane shear modulus? How much does the factor by which the engineering properties are reduced influence the failure scenarios? Does it make any difference to reduce the engineering properties once when failure is first detected rather than to recursively reduce the properties at each subsequent pressure level? To study the influence of the different degradation schemes, the PFA option will be configured to use the maximum stress failure criterion.

By way of a brief outline, the chapter will be organized to begin by describing the geometry, nomenclature, material specifications, and finite-element model of the elliptical cylinder to be

investigated. Next, a method of illustration to visualize the failure scenarios will be presented. The chapter will then discuss the failure scenario at several pressure levels for a cylinder with quasi-isotropic material orthotropy resulting from using a degradation scheme that degrades non-recursively the extensional modulus in the direction perpendicular to the fibers, E_2, the inplane shear modulus, G_{12}, the major Poisson's ratio, ν_{12}, and the minor Poisson's ratio, ν_{21}, when matrix tensile failure is detected. (see Table 2.1) This degradation scheme will be referred to as the baseline scheme. The results obtained for the quasi-isotropic cylinder will then be used to compare with the resulting matrix failure scenarios for cylinders with circumferentially-stiff and axially-stiff material orthotropy; the same baseline degradation scheme was used for all three material orthotropies. In keeping with the procedure in Ch. 2, a value of β=0.2 will be used. From that comparison some conclusions on the effects of material orthotropy on the failure behavior of elliptical cylinders will also be made. Finally, other degradation schemes will be used, including using other values of β, and comparisons between the different schemes will be made.

3.1 Problem Formulation

To provide a basis to study and compare the results obtained in this study, an internally pressurized elliptical cylinder model similar to the one used by McMurray and Hyer is adopted. It is believed that the results for an elliptical cylinder can be extended to more general non-circular cylinders due to their common trait, namely, the varying curvature of their cross sections. Figure 3.1 describes the elliptical cylinder by depicting the geometry of its reference surface and the nomenclature to be used. As can be seen from the figure, the length of the cylinder is represented by L and is oriented in the x-direction of an orthogonal reference system located at the geometric center of the cylinder. The major and minor diameters of the elliptical cross section are designated by $2a$ and $2b$, respectively. The ellipticity of the cylinder is denoted by e and is defined here as b/a. The parameter s represents the circumferential coordinate measured counterclockwise from the top, or crown, of the cylinder, and C denotes the circumference of the cylinder cross section. The wall thickness is denoted by H and the internal pressure is indicated by p_o. The crown, keel, and sides of the cylinder are identified by the locations s/C=0, s/C=0.5, and s/C=±0.25, respectively.

Though they will not be discussed explicitly, also shown in fig 3.1 are the directions of the displacements and the rotations of the reference surface. The displacements are denoted by u^o, v^o, and w^o, and represent the axial, circumferential and outward normal displacements, respectively. The corresponding rotations about those directions are denoted as ru^o, rv^o, and rw^o. The displacements and rotations are all functions of the x and s coordinates. The boundary at one end of the cylinder is assumed to be completely clamped, while the other end is clamped but allowed to move freely in the axial direction, as if it was fastened to a bulkhead. Mathematically, the boundary conditions are expressed as follows:

$$\begin{aligned} x &= -\frac{L}{2} \quad u^o = 0,\ v^o = 0,\ w^o = 0,\ rv^o = 0 \\ x &= +\frac{L}{2} \quad u^o = \Delta,\ v^o = 0,\ w^o = 0,\ rv^o = 0 \end{aligned} \tag{3.1}$$

where Δ is given by enforcing equilibrium in the axial direction; that is

$$\int_0^C N_x ds = \pi \cdot a \cdot b \cdot p_o \tag{3.2}$$

where N_x is the axial force resultant defined as

$$N_x = \int_{-\frac{H}{2}}^{\frac{H}{2}} \sigma_x d\zeta \tag{3.3}$$

The cylinder is modeled assuming graphite-epoxy material with properties as listed in Eq. (2.21). Three different balanced symmetric laminates are considered; namely, quasi-isotropic $[\pm 45/90/0]_s$, circumferentially-stiff $[\pm 45/90_2/0_{1/2}]_s$, and axially-stiff $[\pm 45/0_2/90_{1/2}]_s$ laminates. The fiber orientations for all the layers in these laminates are measured with respect to the axial direction. It should be mentioned that each laminate has at least one layer with fibers in the 0° direction, one layer with fibers in the 90° direction, and all have ±45° layers on the inside and outside. In this study laboratory scale elliptical cylinders were studied so that, eventually, experiments can be performed to compare with the results obtained here. From a practical point of view, small scale cylinders are easier to fabricate by hand using elliptical mandrels than large scale cylinders, and they are less expensive to fabricate and test. The dimensions of the cylinder are as follows:

$$L = 12.5 \text{ in.} \quad a = 5 \text{ in.} \quad b = 3.5 \text{ in.}$$

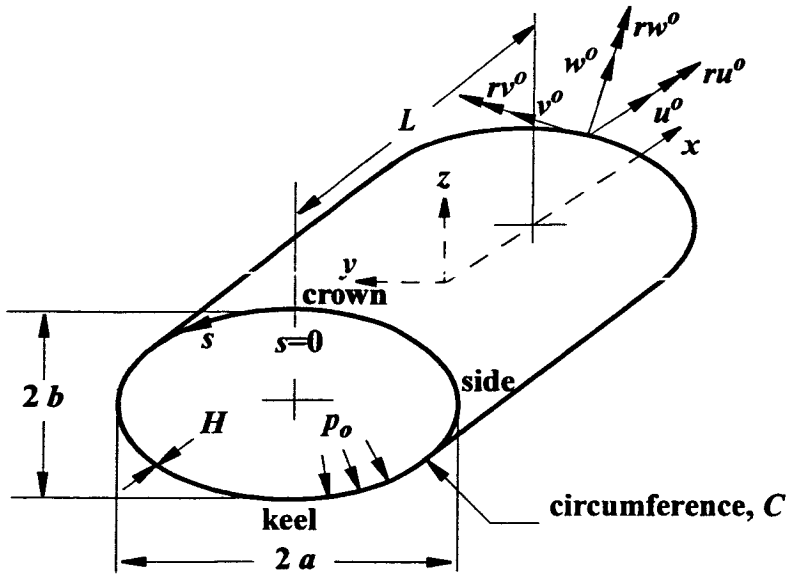

Figure 3.1 Geometry and nomenclature of elliptical cylinder

3.2 Finite-Element Model

The finite-element mesh of the elliptical cylinder is shown in Fig. 3.2. This mesh is con-

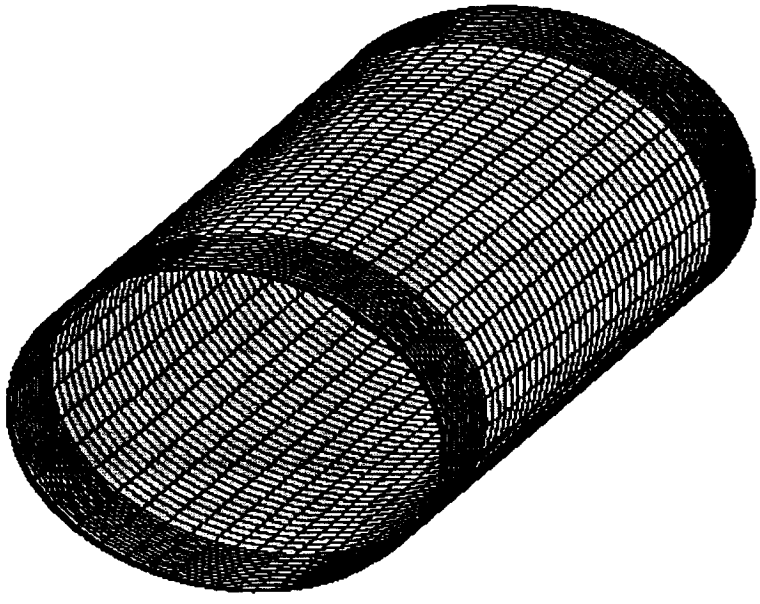

Figure 3.2 Finite-element mesh of elliptical cylinder

structed using five shell units with a total of 3500 elements, there being 70 elements in the axial direction and 50 elements in the circumferential direction. The shell elements are the plane-stress

E410 quadrilateral element from the STAGS element library. The elements are configured to use four integration points at the top and bottom of each layer of composite material. That is, for the eight and nine layer composite laminates studied, there are 64 or 72 integration points per element, respectively. The mesh spacing is uniform in the circumferential direction, however the mesh density in the axial direction, as Fig. 3.2 shows, increases near the clamped ends to accurately describe these zones where high axial gradients are expected.

3.3 Method of Illustration

To illustrate the resulting failure scenarios here and throughout this study, the method of illustration shown in Fig. 3.3 will be used. A quadrant of the cylinder is isolated from the rest of the

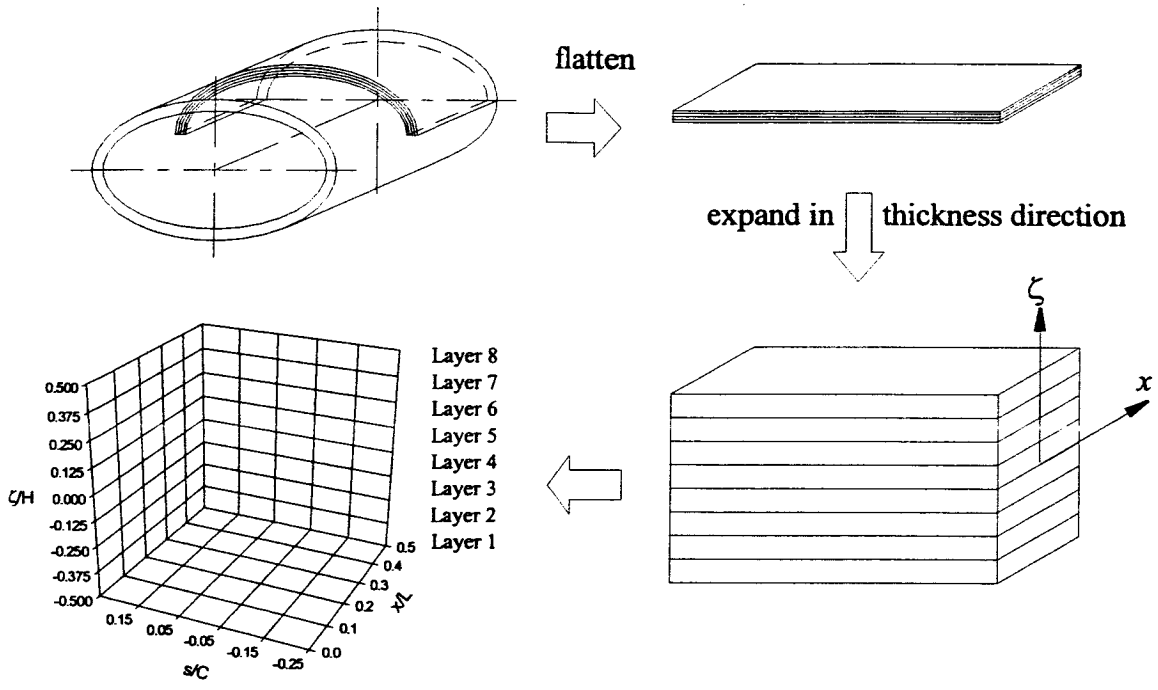

Figure 3.3 Method of illustrating one quadrant of the elliptical composite cylinder

cylinder, as highlighted in the top left portion of the figure. This quadrant is then flattened and expanded in the thickness direction, which is greatly exaggerated. These two steps are identified in the figure. A three-dimensional map is then created, as shown in the bottom left portion of Fig. 3.3. In this map, the non-dimensional range of the quadrant selected extends from $0 \leq x/L \leq +0.5$

in the axial direction and $-0.25 \leq s/C \leq +0.25$ in the circumferential direction. The non-dimensional range in the thickness direction is $-0.5 \leq \zeta/H \leq +0.5$. Where ζ=0 at the geometric midsurface of the cylinder wall. The layers are numbered so that the inner, or bottom layer, is layer 1. The finite-elements consisting of all the layers fill this three-dimensional space. Although failures can occur at each integration point in a layer in an element, when a matrix tensile failure is encountered, for example, a single red circular sphere is plotted at the centroid of the layer in the element in which failure of any of its integration points occurred. This procedure is done due to the limited resolution of this graphical representation. As the pressure is increased and more matrix failures are detected, more spheres are added to the map, exhibiting a clearer matrix cracking pattern. It is important to emphasize that due to the presence of the bending stiffnesses D_{16} and D_{26}, there is not quarter symmetry in the response. However, using symmetric and anti-symmetric arguments, the cracking pattern for the whole cylinder can be envisioned, and displaying one quadrant of the cylinder as in Fig. 3.3 results in a less cluttered display of failure locations. The next section will present and discuss in detail the matrix failure maps at specific pressure levels for the quasi-isotropic cylinder resulting from the use of the baseline degradation scheme.

3.4 Failure Initiation and Progression in a Quasi-Isotropic Elliptical Cylinder Using the Maximum Stress Failure Criterion and the Baseline Degradation Scheme with β=0.2

For the quasi-isotropic cylinder, the pressure was increased in increments of 10 psi or less to determine initial failure and to continue monitoring for failures until first fiber failure occurred. Before performing the analysis, it was determined that below 100 psi the elliptical cylinder was unlikely to fail. That was a rough estimate based on a circular cylinder with a radius equal to the average of the semi-minor and semi-major diameters of the elliptical cylinder. The maximum stress failure criterion was selected in STAGS to determine failure. The conditions for failure using this criterion were listed in Eq. (2.4) through Eq. (2.8). The PFA option in STAGS was set to use the baseline degradation scheme using a factor of β=0.2 when matrix tensile failure was detected. Matrix failures due to shear in the *x-s* plane could be accommodated, but up to first fiber failure, surprisingly, none were encountered. The output given by STAGS listed the mode of failure, element number, layer number, and integration points where failures were detected. With that

information, the three-dimensional map described in the previous section was filled to display the failure pattern in the cylinder.

Figure 3.4 shows the failure maps for the quasi-isotropic cylinder at four different pressure levels. The pressure values are indicated at the upper left hand corner of each map. The fiber angle and layer number are written next to each layer. The red spheres in all of the failure maps indicate that the mode of failure at these pressures is matrix tension, or matrix cracking, which means excessive σ_2 stress in tension in the direction perpendicular to the fibers. At the top left corner of the figure the failure map corresponding to a pressure of 140 psi is shown. This pressure is slightly above the pressure to cause first matrix tensile failure. The pressure at which the first failure occurred was found to be approximately 138 psi. As can be seen from the map, at 140 psi two elements in the inner $+45^{\circ}$ layer, or layer 1, exhibit matrix tensile cracks. The axial location of these failures coincides with the end of the cylinder. The circumferential locations of these cracks are partway between the center of the crown and one of the sides, at $s/C \approx -0.13$. It should be pointed out that there are no companion failures at $s/C \approx +0.13$ due to the nonzero stiffnesses D_{16} and D_{26}. These stiffnesses couple bending and twisting, producing an anti-symmetric failure pattern. In other words, D_{16} and D_{26} cause companion failures to the ones shown at $s/C \approx +0.37$ in the lower quadrant at the $x/L=+0.5$ end of the cylinder. At the other end of the cylinder, at $x/L=-0.5$, the matrix cracks would appear at $s/C \approx +0.13$ and at $s/C \approx -0.37$. The first matrix failure pressure as well as the location of the first matrix cracks agreed with the failure pressure and location found by McMurray and Hyer in [3], where a stand-alone pre/post processing program to perform the progressive failure analysis was used in combination with STAGS. This agreement was expected because, in their work, they used a similar finite-element mesh and the progressive failure analysis is not necessary up to the point of initial matrix cracking. The initial matrix cracks shown in the map corresponding to the 140 psi pressure level are believed to occur at those locations mainly due to large values of shear stress resultant and high bending effects that originate from the clamped boundary conditions which forces any circumferential and normal displacements to be zero at the boundary. These suspicions agree with the findings in [1,2]. Recall, as stated in the introduction, that those studies showed that the maximum shear force resultants occur near the clamped boundaries, part way between the ends of the minor of the major diame-

ters in the four quadrants at each clamped end of the cylinder, and that the maximum bending moment resultants occur at the clamped ends.

At 170 psi, shown at the top right corner of Fig. 3.4, it can be seen that more matrix tensile failures occur in the inner ±45° layers, and new failures occur in the outer 90° and +45° layers. Compared to the 140 psi map, the cracks in the +45° layer have clearly progressed circumferentially toward the crown and the side. Although difficult to notice, some axial progression toward the center of the cylinder also occurs in this layer. This becomes more clear at 200 psi by noticing what seems like the elongation of the round symbols. Due to the perspective of this graphical representation, as cracking moves axially and a symbol is added, it overlaps the symbol behind it, giving the appearance of an elongated symbol. Also at 200 psi, it can be observed that all cracking patterns continue to expand circumferentially. New cracks also have developed at the sides in the other 90° and -45° layers. The two 0° layers do not exhibit any cracks. At 230 psi, it seems that more axial progression of the cracks has occurred, in particular, near the sides. Circumferential progression of the cracks in the inner ±45° layers, as seen by the overlapping near s/C=0.05, begin to create a contiguous path between those two layers. However, because the remainder layers do not possess any cracks at that axial and circumferential location, there is no leakage path. Moreover, it was determined that up to the pressure to cause first fiber failure (not shown), no complete leakage path had developed because the two 0° layers remained free of cracks. This finding coincides with McMurray and Hyer's prediction in [3]. The first fiber failure pressure was found to be approximately 246 psi. The amount of damage in the cylinder at that pressure was assessed by the ratio of the number of integration points with damage (matrix and fiber) and the total number of integration points. That ratio indicated that 5.5% of the cylinder had damage at the first fiber failure pressure. The first fiber failure mode was found to be fiber compression and it occurred in the outer +45° layer near s/C=–0.13. This will be discussed later. One interesting point that should be mentioned is that the overall cracking pattern for the quasi-isotropic cylinder using the PFA option in STAGS was found to be similar to the failure scenario found by McMurray and Hyer. However, the first fiber failure pressure was found to be slightly higher in [3] than the one found here. It is believed that the reason for the discrepancy is that in [3], a different convergence criteria was used in the iteration process of the progressive failure analysis.

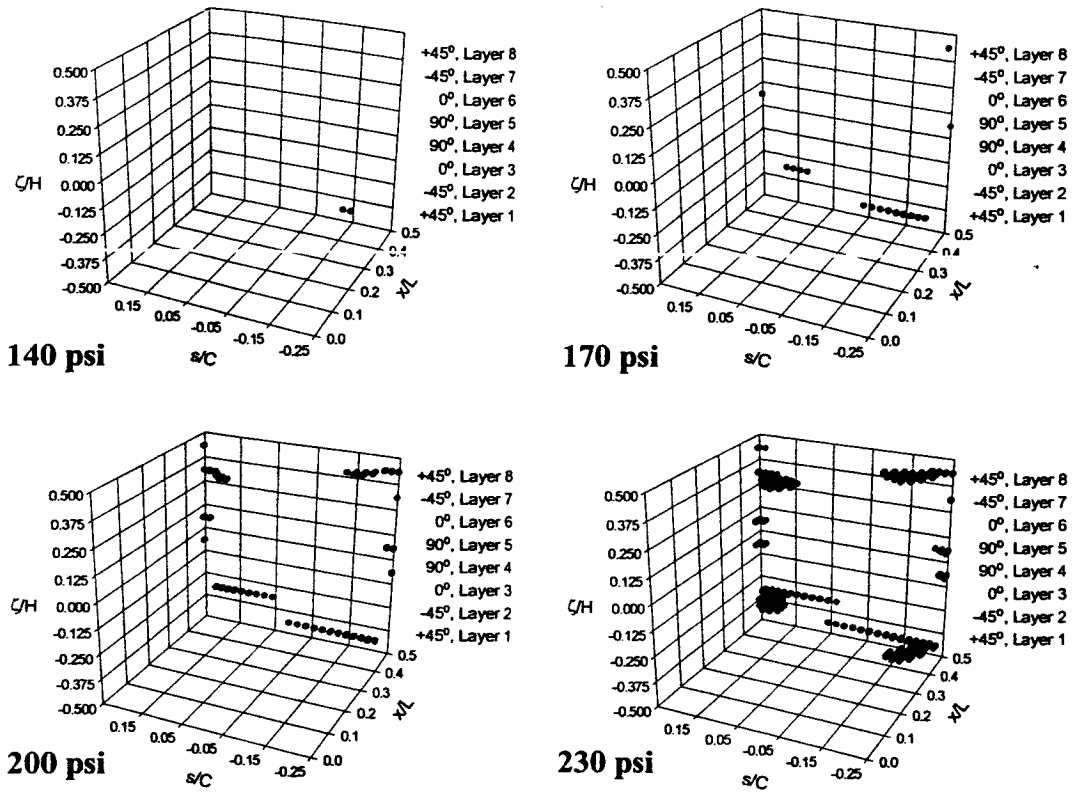

Figure 3.4 Matrix cracking scenario for the quasi-isotropic $[\pm 45/0/90]_s$ elliptical cylinder at different pressure levels, maximum stress criterion, baseline degradation scheme, β=0.2

The same analysis performed on the quasi-isotropic elliptical cylinder was repeated for the circumferentially-stiff and axially-stiff cylinders. The matrix cracking maps for these cylinders can be seen in Fig. 3.5. The first column in the figure shows the failure maps at 140, 170, 200, and 230 psi previously shown in Fig. 3.4 for the quasi-isotropic cylinder. The second and third columns show the cracking patterns, at the same pressure levels, for the circumferentially-stiff and axially-stiff cylinders, respectively. Figure 3.5, clearly shows how material orthotropy influences the matrix cracking patterns in an elliptical cylinder. It should be mentioned again that the circumferentially-stiff and axially-stiff cylinders are made of 9-layers with $[\pm 45/0_2/90_{1/2}]_s$ and $[\pm 45/90_2/0_{1/2}]_s$ fiber orientations, respectively. Because of space limitations, the layer numbers and fiber angles are omitted in the subfigures.

The middle column of Fig. 3.5 shows the cracking maps for the circumferentially-stiff cylinder. At 140 psi can be seen that matrix cracks occur at the sides of the cylinder rather than partway between the crown and the side, as is the case for the quasi-isotropic cylinder. At that pressure level, the circumferentially-stiff cylinder has cracks in the outer ±45° layers, layers 8 and 9, the two outer 90° layers, layer 6 and 7, as well as the 90° layer just inside the midsurface, layer 4. This cylinder exhibits many more cracks than the quasi-isotropic cylinder at 140 psi because the first matrix tensile failure in the circumferentially-stiff cylinder occurred at a pressure of approximately 105 psi. So a number of cracks have developed between 105 and 140 psi. The first matrix failure pressure and location for this cylinder, as expected, also agreed with the failure pressure and location found in [3]. It is believed that the cracks initially occur at the sides of the circumferentially-stiff cylinder because of high values of the circumferential bending moment and force resultants there, and low resistance to cracking in the axial direction of the 90° layers. There is only one 0° layer to directly resist axial loads. The map associated with the pressure of 170 psi shows that the cracking has mainly progressed axially, but also there is some progression circumferentially. This map for 170 psi also shows that several more matrix failures occurred in the inner three layers.

At 200 psi there is even more axial and circumferential progression. However, no cracks are seen in the 0° layer, the central layer, layer 5. At 230 psi, the progressive pattern continues, now causing some overlap of matrix cracks in the inner ±45° layers, layers 1 and 2, near s/C=+0.05, as was the case for the quasi-isotropic cylinder. In addition, new cracks developed at the side s/C=–0.25 in the inner –45° layer, clearly forming a potential continuous path for the pressure to escape. However because the single 0° layer remains crack-free, the formation of a leakage path is impeded. Interestingly, up to the pressure to cause first fiber failure, which was found to be 253 psi, no complete leakage path forms. It is believed that the single 0° layer remains uncracked because the 90° layers protect that layer. The percent damage in the cylinder when first fiber failure occurred was approximately 6.9%. The mode of the first fiber failure was found to be fiber compression and the location of this fiber failure was in the outer +45° layer. More will be said of the first fiber failure later.

The furthest right column of Fig. 3.5 shows the maps for the axially-stiff cylinder. At the pressure levels of 140 and 170 psi, it can be seen that the axially-stiff cylinder exhibits a very similar cracking pattern to the one found for the quasi-isotropic cylinder. Even the first matrix tensile failure was found to occur at practically the same pressure as for the quasi-isotropic case; precisely, the first matrix tensile failure pressure occurred at about 139 psi in the axially-stiff cylinder. Once again, the failure pressure and location agreed with the findings in [3]. It is suspected that the failures, as in the quasi-isotropic case, occur due to high bending effects at the clamped ends of the cylinder and high values of the shear stress resultant produced by the boundary condition on restricting the normal and circumferential displacements. At 200 psi, the cracking pattern changes significantly with respect to the quasi-isotropic case. A large amount of cracking occurs within the range from 170 to 200 psi. In fact, because of a large number of cracks that developed between 180 and 190 psi step (recall that the analysis was performed in 10 psi steps), the number of iterations allowed in STAGS had to be increased. Recall that the PFA option at a given load step performs a Newton-Raphson iteration to determine if more, less, or no failures occurred with respect to the previous iteration. If more failures occur at certain iteration, then the engineering properties are degraded, stresses computed, failure checked, and if more failures are detected, another iteration takes place. This is repeated until no more failures are found and the analysis is said to have converged for that load step. STAGS allows a maximum of 22 of these iterations at a given load step. If this number is exceeded, the program cuts the load step and repeats the analysis at a lower load step. The number of cuts is set by the user. In the analysis performed here, that number was set to 5. For the axially-stiff cylinder, the maximum number of iterations needed for the analysis to converge at the load step between 180 and 190 psi was exceeded and the program cut the load step once in half. The analysis converged at the load step between 180 and 185 psi. However, when the pressure was increased from 185 to 190 psi, the analysis did not converged even after 5 cuts in the pressure step. A special option in STAGS which extends the maximum number of iterations allowed to 40 was then executed. With this option, no cuts in the 10 psi pressure steps were needed.

Also in the cracking map at 200 psi in Fig. 3.5, it can be seen that most of the matrix cracks are concentrated in the 0^{o} layers, layers 3, 4, 7, and 8, near the crown, away from the clamped end. It can also be observed that at 200 psi the cracking has progressed quickly axially towards the

midspan of the cylinder. It is believed that this cracking pattern develops due to large values of the circumferential force resultants. Because the maximum circumferential force resultants occur partway between the clamped end and the midspan of the cylinder in the crown region, as indicated by the previous studies [1, 2], and because there is only one 90° layer in this cylinder wall to resist those force resultants, layer 5, cracking in the 0° layers quickly progresses towards the midspan of the cylinder in the crown area.

To actually see in the cracking map that there is an axial distance between the end of the cylinder and the circumferential line of cracks closest to $x/L=+0.5$ in layer 7, a 0° layer, for instance, a line parallel to the s/C-axis can first be drawn through the centroid of that layer at $x/L=+0.5$. A second line also parallel to the s/C-axis can then be constructed that passes through the centroids of the round symbols forming this line of cracks. Note that the centroids of the round symbols in this line have to be estimated, since other rows of symbols overlap the first row. Finally, a third line, this time parallel to the c-axis and long enough to intersect the previous two, can be traced through the centroid of layer 7 at $s/C=+0.25$. The fact that there is a finite distance between the intersection point of the first with the third line and the intersection point of the second with the third line, indicate that the first row, and therefore subsequent rows of cracks, occur away from the end of the cylinder. This procedure can be followed to estimate the distance between the end of the cylinder and any axial location. Also at 200 psi it is shown that the only uncracked layer is layer 5, or the 90° layer.

The map at 230 psi shows an impressive amount of damage. Cracks have progressed axially as well as circumferentially and encompass a significant percentage of the three-dimensional space. The layers that exhibit the most cracks are the 0° layers. As mentioned above, because there is a small number of fibers in the circumferential direction to resist the large circumferential force resultants, these 0° layers become the most vulnerable to cracking. Although difficult to see from the map, the 90° layer, surprisingly, remains crack-free regardless the high number of matrix tensile failures in the other layers. At the first fiber failure pressure (not shown), which occurs at approximately 251 psi, this 90° layer does not exhibit any cracks, even though 26.5% of the entire

cylinder was found to be damaged. Because up to first fiber failure, the 90^{o} layer remains uncracked, the axially-stiff cylinder does not have a leakage path for the pressure to escape.

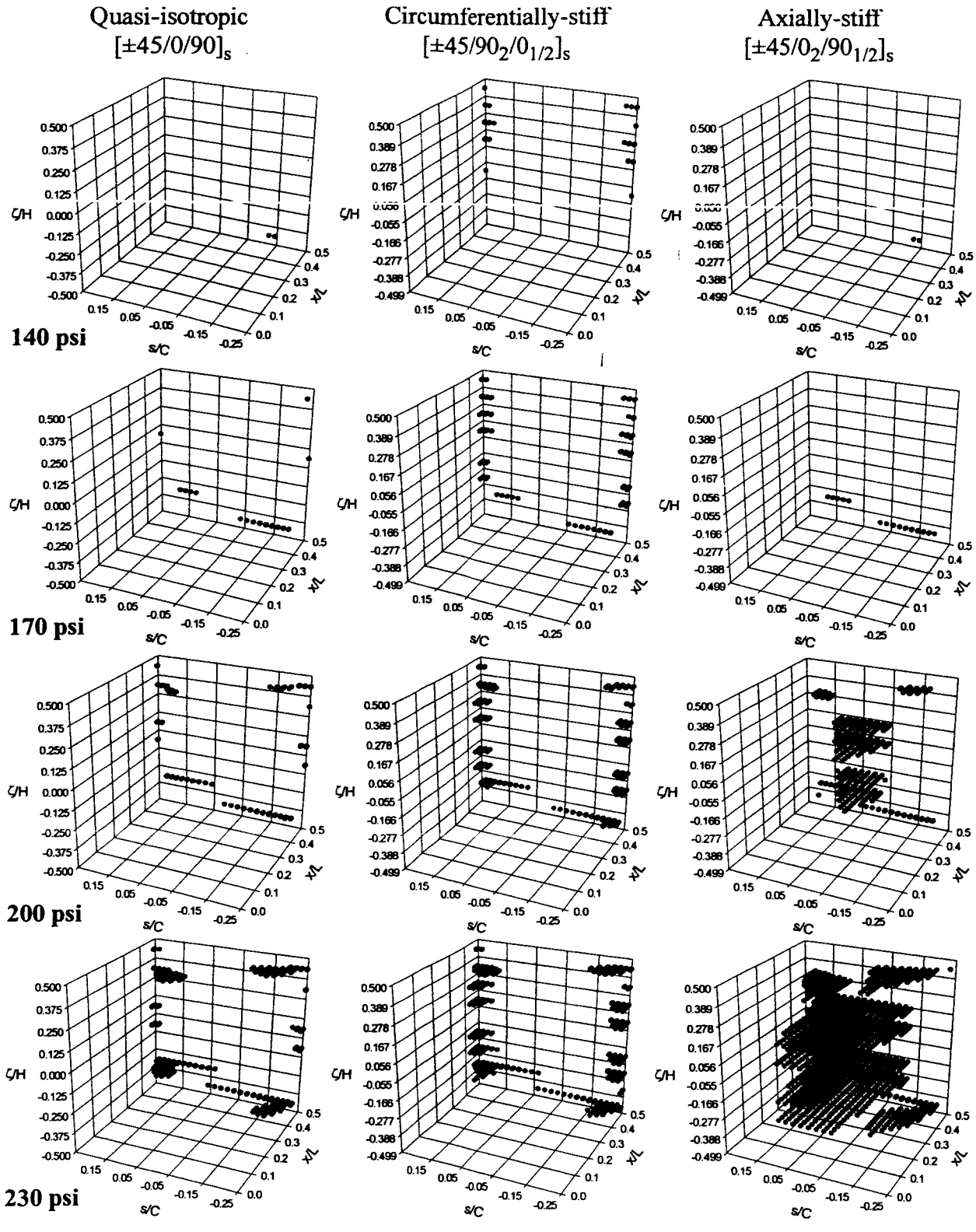

Figure 3.5 Matrix cracking scenarios for elliptical cylinders with different material orthotropy, maximum stress criterion, baseline degradation scheme, β=0.2

Tables 3.1 and 3.2 summarizes the pressures for first matrix tensile and first fiber failures for each of the cylinders. In Table 3.2, the percent damage associated with the first fiber failure pressures are also listed.

Table 3.1: First matrix failure pressures for maximum stress criterion

Cylinder orthotropy	First matrix failure pressure, psi
quasi-isotropic	138
circumferentially-stiff	105
axially-stiff	139

Table 3.2: First fiber failure pressures for maximum stress criterion, baseline degradation scheme, β=0.2

Cylinder orthotropy	First fiber failure pressure, psi	Percent damage[a]
quasi-isotropic	246	5.5
circumferentially-stiff	253	6.9
axially-stiff	251	26.5

a. Number of failed integration points / total number of integration points

The key results for the three cylinders just discussed are summarized as:

i. All of the cylinders were found to exhibit the same type of failures at the indicated pressures. Specifically, matrix tension, or matrix cracking, which is associated with excessive stress in the direction perpendicular to the fibers, occurred for all pressure levels up to first fiber failure pressure.

ii. The first matrix cracks occurred, for all intents and purposes, at the same pressures and locations for the quasi-isotropic and axially-stiff cylinders. That pressure was close to 140 psi. The matrix cracks at that pressure were found, mainly, to be due to high shear stress resultants and bending effects. For the circumferentially-stiff cylinder, the first matrix failure occurred at a lower pressure than for the other two, i.e., at approximately 105 psi. The cracks in this cylinder

occurred at the sides and were mainly due to large values of the axial bending moment and force resultants.

iii. The quasi-isotropic cylinder sustained the least amount of damage of all three cylinders, i.e., 5.5% damage at first fiber failure pressure. The circumferentially-stiff cylinder exhibited slightly more cracks than the quasi-isotropic cylinder. The axially-stiff cylinder had significantly more damage than the other two, i.e., 26.5% at first fiber failure pressure.

iv. At the first fiber failure pressure it was found that no complete leakage paths developed in any of the three cylinders. This fact was particularly remarkable for the case of the axially-stiff cylinder, in spite of the large amount of damage exhibited at that pressure.

3.5 Effects of not Degrading G_{12} on the Matrix Failure Scenarios

To answer the question of how the degradation of the inplane shear modulus impacts the matrix cracking scenarios for the quasi-isotropic, circumferentially-stiff, and axially-stiff cylinders, the matrix cracking scenarios obtained by using the baseline degradation scheme are compared with the resulting matrix failure scenarios when G_{12} is not degraded. In both cases the maximum stress criterion is used and β=0.2.

In Fig. 3.6 the effects of inplane shear modulus degradation on the matrix cracking pattern for the quasi-isotropic elliptical cylinder can be seen. The left column of the figure shows the cracking maps at the pressure levels of 140, 170, 200, and 230 psi that correspond to the baseline degradation scheme shown in Fig. 3.4, which is the scheme reproduced in Fig. 3.5, in the left hand column. The right column of Fig. 3.6 shows the cracking maps at the same pressure levels for the case of not degrading G_{12}. As can be observed from the figure, for the quasi-isotropic cylinder, it is fair to say that the degradation of the inplane shear modulus has little impact in the matrix cracking scenarios at the pressure levels shown, thus concluding that G_{12} is not important for resisting matrix crack progression. In fact, at the first three pressure levels there are no noticeable differences between the two cases. At 230 psi, though difficult to see, the distribution of the cracks is slightly different; however, the overall amount of cracking seems to be the same in both cases. For example, in the inner $+45^{\circ}$ layer, the map for baseline degradation scheme at 230 psi shows fewer cracks than the right hand side map where G_{12} is not degraded. On the other hand, in the inner -45° layer, the former map exhibits more cracks. The argument that the degradation of the inplane shear does not play an important role in resisting matrix crack progression for the quasi-isotropic cylinder can be further supported by the facts that the first fiber failure pressure and the percent damage, listed in Table 3.3, are not affected by the degradation or lack of degradation of the inplane shear modulus.

Figure 3.7 shows the effects of the shear modulus degradation for the circumferentially-stiff cylinder. Following a format similar to the one presented for the quasi-isotropic cylinder, the left column shows the failure scenarios for the baseline degradation scheme at 140, 170, 200, and 230

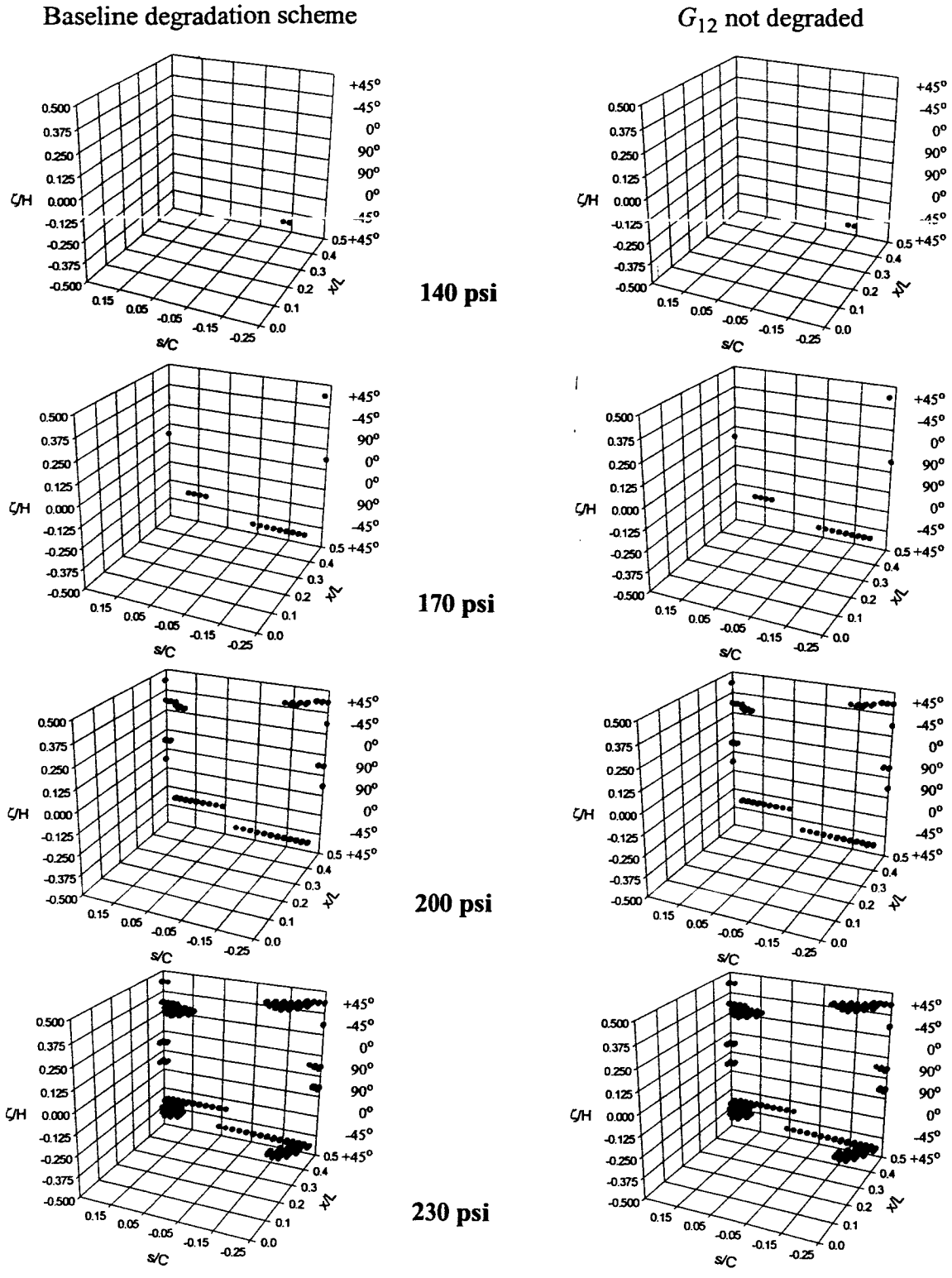

Figure 3.6 Effects of shear modulus degradation on the matrix cracking scenario for the quasi-isotropic $[\pm 45/0/90]_s$ elliptical cylinder, maximum stress criterion, β=0.2

psi. These cracking maps were previously shown in the middle column of Fig. 3.5. The right column shows the cracking maps for the case where G_{12} is not degraded. From the figure, it can be seen that for the circumferentially-stiff cylinder, the shear modulus degradation has a small effect on the matrix cracking scenarios. Specifically, at all pressure levels shown, the maps for the baseline degradation scheme exhibit slightly more cracking than the maps for the case where G_{12} is not degraded. For example, at 140 psi, the left hand side map shows cracks in the 90° layer just inside the midsurface, at the sides of the cylinder, $s/C \approx \pm 0.25$. Those cracks do not occur in the right hand side map at that pressure. At 170 psi, at a glance, there are no significant differences between the baseline degradation scheme and the scheme where G_{12} is not degraded. However, the innermost 90° layer in the left hand side map shows a few more cracks at $s/C \approx -0.25$. At the next pressure level, 200 psi, the same trend occurs, the left hand side map shows more cracks in the outer +45° layer near $s/C=-0.15$ and in the outer and inner –45° layers near $s/C=+0.25$. At 230 psi pressure level, more cracking still occurs in map for the baseline degradation scheme in the ±45° and the inner two 90° layers near the sides of the cylinder. To quantify the impact of degrading the inplane shear modulus on the matrix failure scenario for this cylinder; that is, to assess to what extent the shear modulus resists the progression of matrix cracks, Table 3.3 shows the values for the first fiber failure pressures and the corresponding percent damage associated with both cases. As indicated in the table, for the baseline degradation scheme, the percent damage is slightly larger and the first fiber failure occurs at a slightly lower pressure than when G_{12} is not degraded.

With a format similar to the one used for the previous two cylinders, Fig. 3.8 shows the comparison between the matrix failure scenarios for the baseline degradation scheme and the case where G_{12} is not degraded for the axially-stiff cylinder. The left column corresponding to the baseline degradation scheme was previously shown in the furthest right column of Fig. 3.5. Though, in Fig. 3.8, at 140, 170, and 200 psi it cannot be seen that the overall amount of cracking is larger for the baseline degradation scheme, at 230 psi, the map associated with that scheme shows more cracking. At the first two pressure levels, the cracking scenarios are identical for both degradation schemes. Interestingly, at 200 psi, the map for the case for the case where G_{12} is not

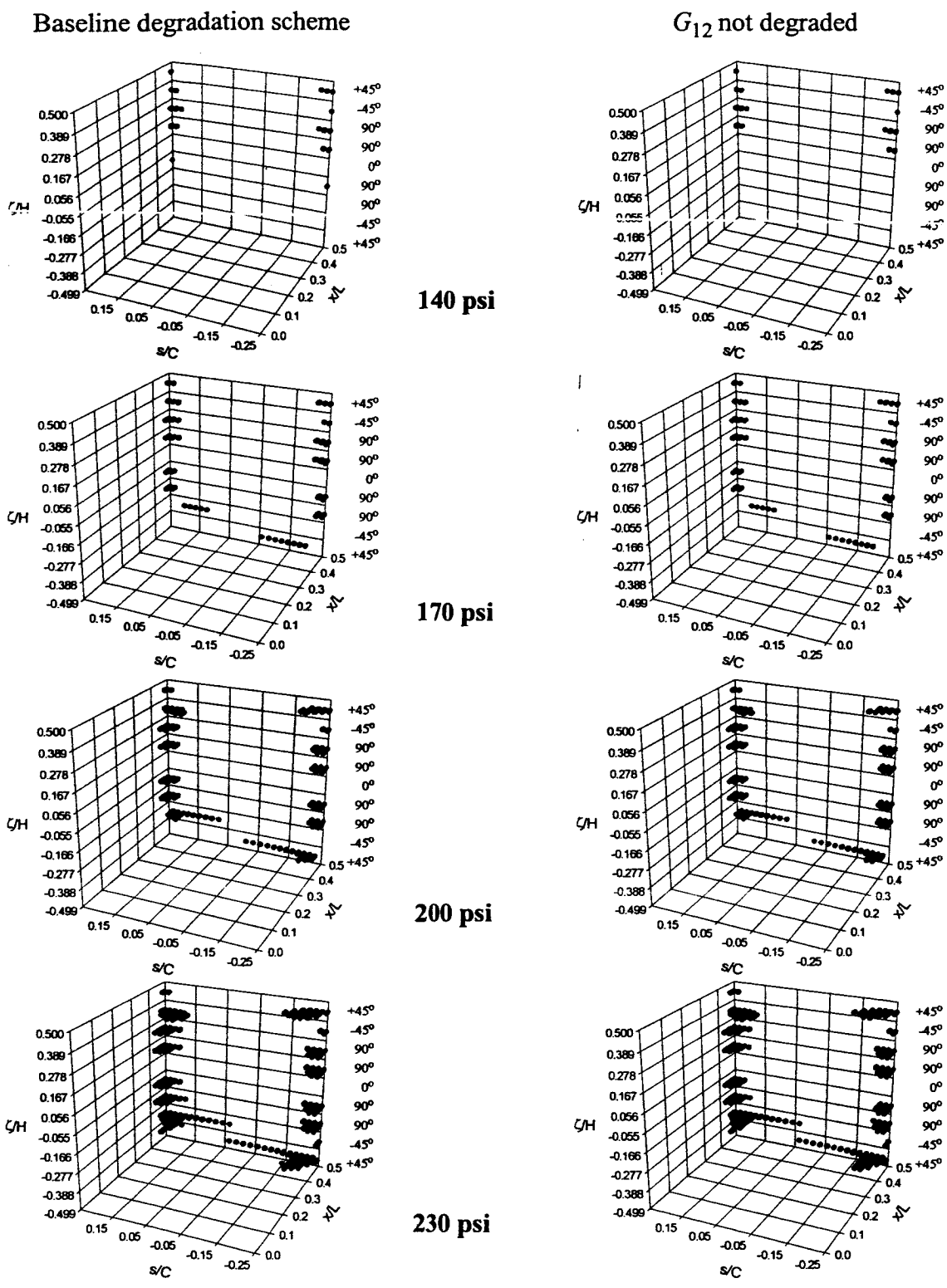

Figure 3.7 Effects of shear modulus degradation on the matrix cracking scenario for the circumferentially-stiff $[\pm 45/90_2/0_{1/2}]_s$ elliptical cylinder, maximum stress criterion, β=0.2

degraded shows cracks occurring away from the clamped end of the cylinder in the inner +45° layer at $s/C \approx -0.15$. Those cracks do not occur in the left hand side map. Also at this pressure, there is more cracking that has progressed axially near the crown in the 0° layer just inside the midsurface in the case that neglects the shear modulus degradation. From the maps at 200 psi, it would seem that the case where G_{12} is not degraded exhibits more cracking. However, at 230 psi the reverse is true. Longer axial lines of cracks can be identified in the left hand side map in the outer +45° layer near the crown, in all the 0° layers near $s/C = \pm 0.15$, and in the inner +45° layer at $s/C \approx -0.15$. As with the circumferentially-stiff cylinder, for the axially-stiff cylinder the first fiber failure pressure is lower and the associated percent damage is higher for baseline degradation scheme than for the case that does not degrade the shear modulus. Those values are indicated in Table 3.3.

Table 3.3: Effects of shear modulus degradation on first fiber failure pressures and percent damage, maximum stress criterion, β=0.2

Scheme	baseline degradation		G_{12} not degraded	
Cylinder orthotropy	First fiber failure pressure, psi	Percent damage[a]	First fiber failure pressure, psi	Percent damage[a]
quasi-isotropic	246	5.5	246	5.5
circumferentially-stiff	253	6.9	255	6.7
axially stiff	251	26.5	253	26.2

a. Number of failed integration points / total number of integration points

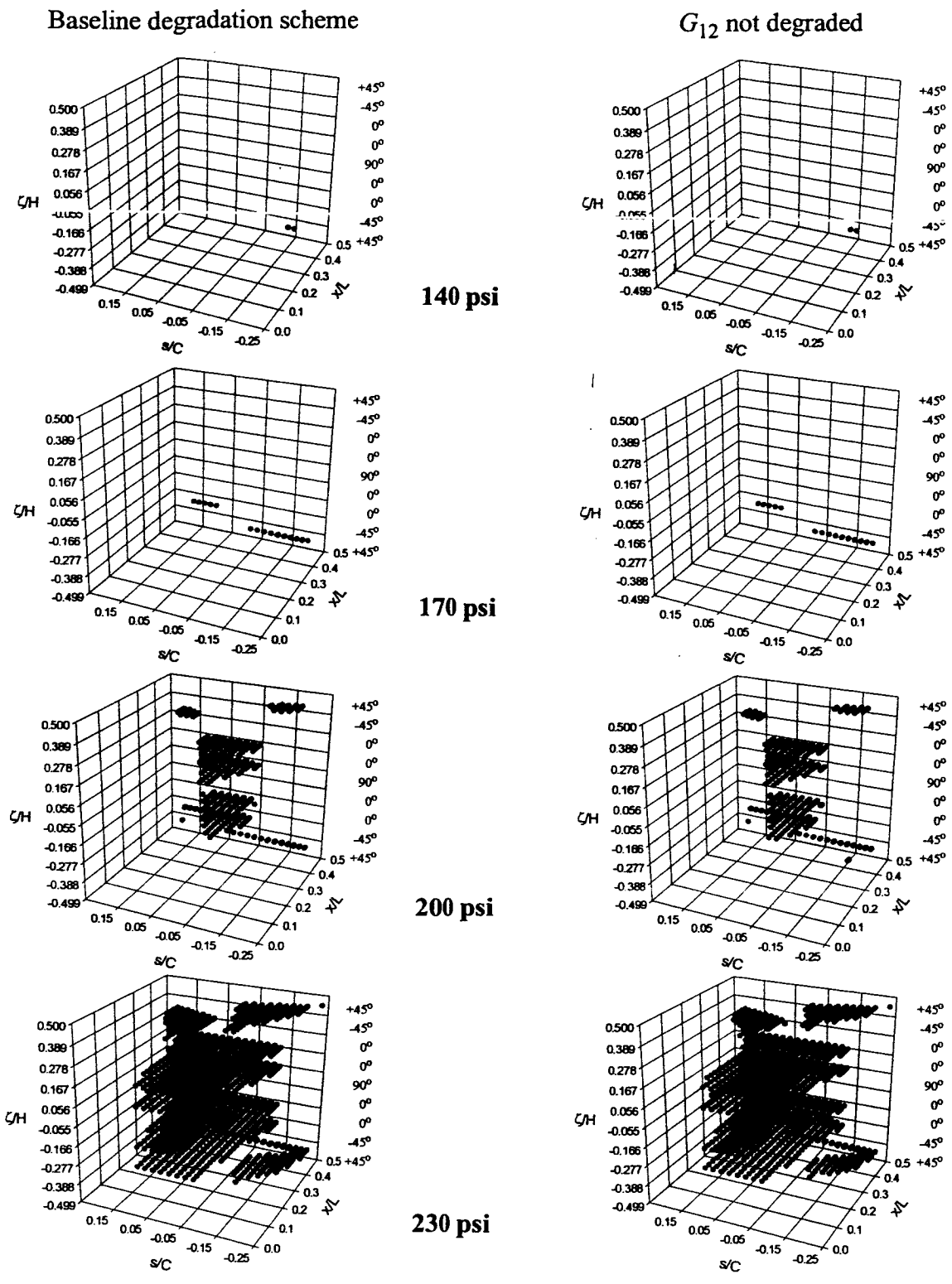

Figure 3.8 Effects of shear modulus degradation on the matrix cracking scenario for the axially-stiff $[\pm 45/0_2/90_{1/2}]_s$ elliptical cylinder, maximum stress criterion, β=0.2

3.6 Influence of β on the Matrix Failure Scenarios

As stated in an earlier chapter, the value of β=0.2 was adapted from the work in [5]. To investigate the effects of the value of the degradation factor on the matrix cracking scenarios for the three cylinders studied, the PFA option was configured to use the baseline degradation scheme and values of β=0.05 and 1.0. It is believed that this range of degradation factors, from severe (β=0.05) to no degradation (β=1), would provide a good idea of how sensitive the predicted matrix cracking scenarios are to the degradation of the engineering properties.

Figure 3.9 shows the failure scenarios for the quasi-isotropic cylinder. The first column shows the results for the case where the engineering properties are reduced by a factor of β=0.2. These failure maps were last seen in Fig. 3.6. The middle and right columns show the cracking maps corresponding to the cases where the engineering properties are reduced by β=0.05 and β=1.0, respectively. As can be seen, if the engineering properties are severely reduced or not reduced at all, it makes, practically, no difference in the matrix cracking scenario for the quasi-isotropic cylinder. With some difficulty, at 230 psi, it can be observed that fewer cracks are noticeable in the furthest right hand side map associated with the case of no degradation. Particularly, in layer 5, the 90° layer above the midsurface, near $s/C=-0.25$ and in layer 8, a +45° layer, near $s/C=+0.25$. At first fiber failure, the percent damage for the quasi-isotropic cylinder, as indicated in Table 3.4, is the same for the three cases. The only effect of using different β factors is that the first fiber failure pressure seems to increase with less severe degradation. In other words, the failure pressure when the engineering properties are not degraded is 2% higher than when the engineering properties are degraded by β=0.05. There is no significant difference in the first fiber failure pressures between the case of β=0.2 and the case of β=0.05.

In Fig. 3.10, following the same format of Fig. 3.9, the matrix failure scenarios for the circumferentially-stiff cylinder are shown. Though not easily seen, the failure maps at all pressure levels show a slight trend associated with the degree of degradation of the engineering properties. That trend, though not pronounced, indicates that the larger the reduction of the engineering properties, the more the predicted damage in the cylinder. For example, at 140 psi, the case of β=0.05 shows a few more cracks in the outer +45° layer, layer 9, at $s/C\approx+0.25$, than the case of β=0.2. At the

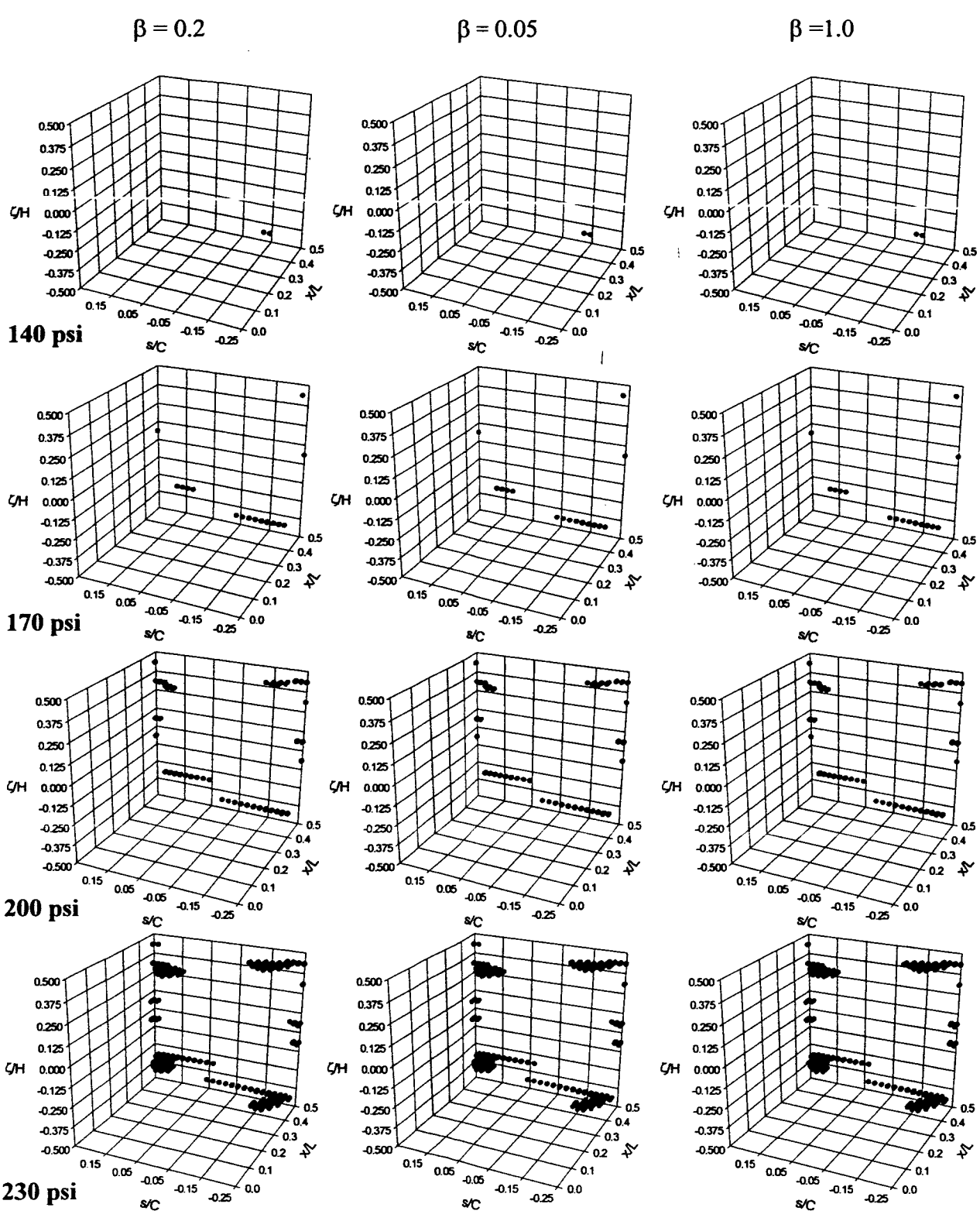

Figure 3.9 Effects of degradation factors on the matrix cracking scenario for the quasi-isotropic $[\pm 45/0/90]_s$ elliptical cylinder, maximum stress criterion, baseline degradation scheme

same pressure, the map for the case of β=0.2, in the 90° layer just inside the midsurface, layer 4, shows cracks that do not occur in the map for the case of no degradation, or β=1.0. The same trend can be seen in the maps at 170 psi. Notice, for the case of β=0.05, the cracks occurring in the inner –45° layer, layer 2, at $s/C \approx +0.25$. Those cracks do not occur in the map for the case of β=0.2. At the same pressure, it can be observed that in the map for β=0.2, in the outer –45° layer, layer 8, at $s/C \approx -0.25$ there is more cracking than in the map for the case of no degradation. Similar observations can be made for the remainder of the pressure levels. Table 3.4 quantifies that trend by indicating the percent damage when first fiber failure occurs. Those values suggest that the case of no degradation sustains the least amount of damage, while the case with most severe degradation exhibits the most damage. Table 3.4 also indicates that the first fiber failure pressures increase with less severe degradation.

The matrix failure maps for the different degradation factors for the axially-stiff cylinder are shown in Fig. 3.11. Again, the format of this figure follows the format of figs. 3.9 and 3.10. Comparison of the maps in Fig. 3.11, shows that as the pressure level increases, the effects of degrading the engineering properties by different β factors become more evident. Particularly, at 200 and 230 psi, it is easy to see that the larger the reduction of the engineering properties, the larger the damage in the cylinder. At 200 psi, for β=0.05, more cracks occur, particularly near the crown, compared to the map corresponding to β=0.2. On the other hand, in the case of no degradation, there is significantly less cracking than in the case of β=0.2. A similar scenario can be seen at 230 psi, where still more cracking near the crown in the case of β=0.05 can be distinguished compared to the case of β=0.2, and significantly less damage is observed in the case of no degradation. Table 3.4 lists the first fiber failure pressures and percent damage for the axially-stiff cylinder for the three different degradation factors. Those values indicate that, compared to the other two cylinders, the degree of degradation of the engineering properties affects the first fiber failure pressure and amount of damage for this cylinder.

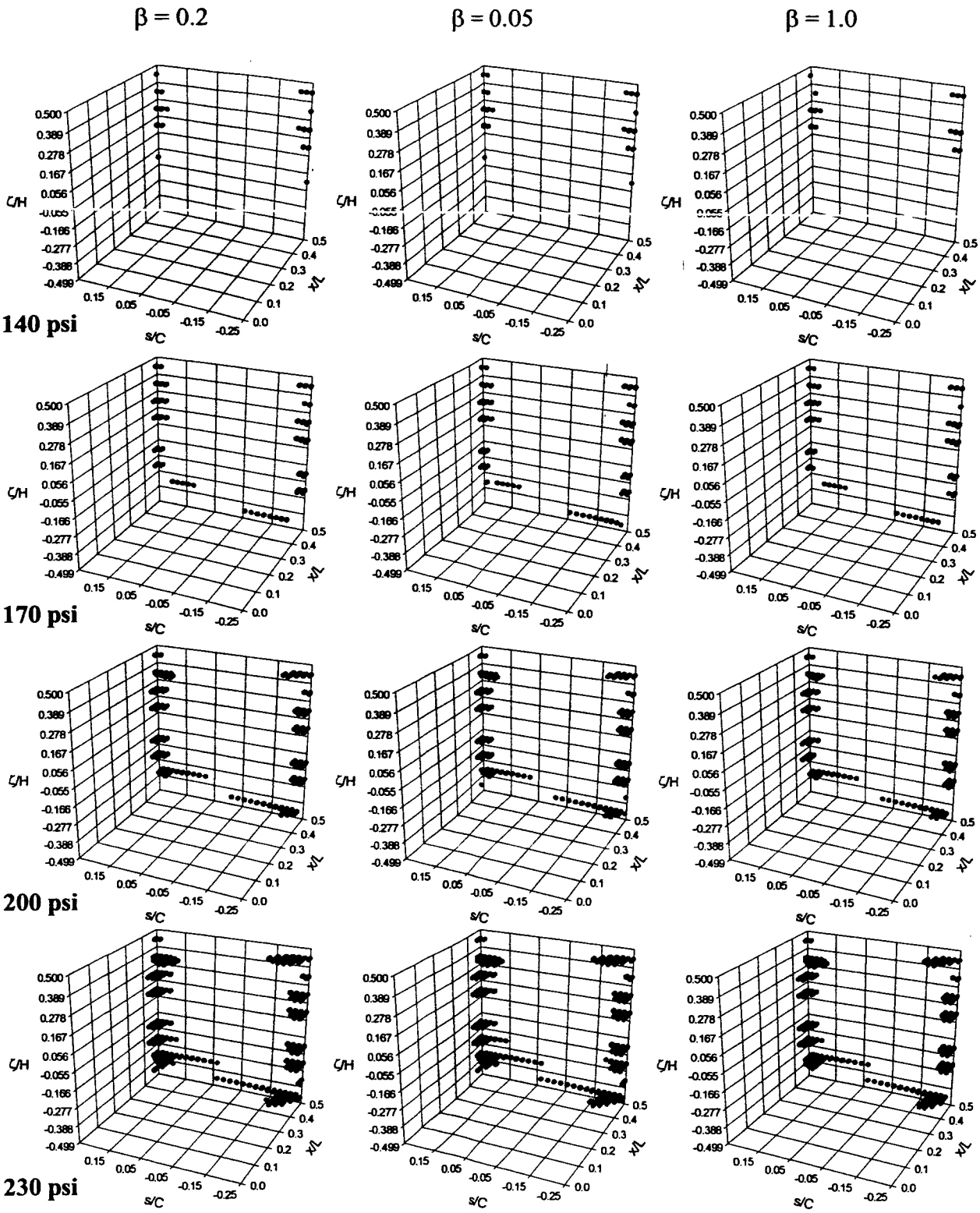

Figure 3.10 Effects of degradation factors on the matrix cracking scenario for the circumferentially-stiff $[\pm 45/90_2/0_{1/2}]_s$ elliptical cylinder, maximum stress criterion, baseline degradation scheme

Table 3.4: Effects of degradation factors on first fiber failure pressures and percent damage, maximum stress criterion, baseline degradation scheme

degradation factor	$\beta = 0.05$		$\beta = 0.2$		$\beta = 1.0$	
Cylinder orthotropy	First fiber failure pressure, psi	Percent damage[a]	First fiber failure pressure, psi	Percent damage[a]	First fiber failure pressure, psi	Percent damage[a]
quasi-isotropic	245	5.5	246	5.5	250	5.5
circumferentially-stiff	252	7.0	253	6.9	258	6.5
axially-stiff	250	27.3	251	26.5	258	22.8

a. Number of failed integration points / total number of integration points

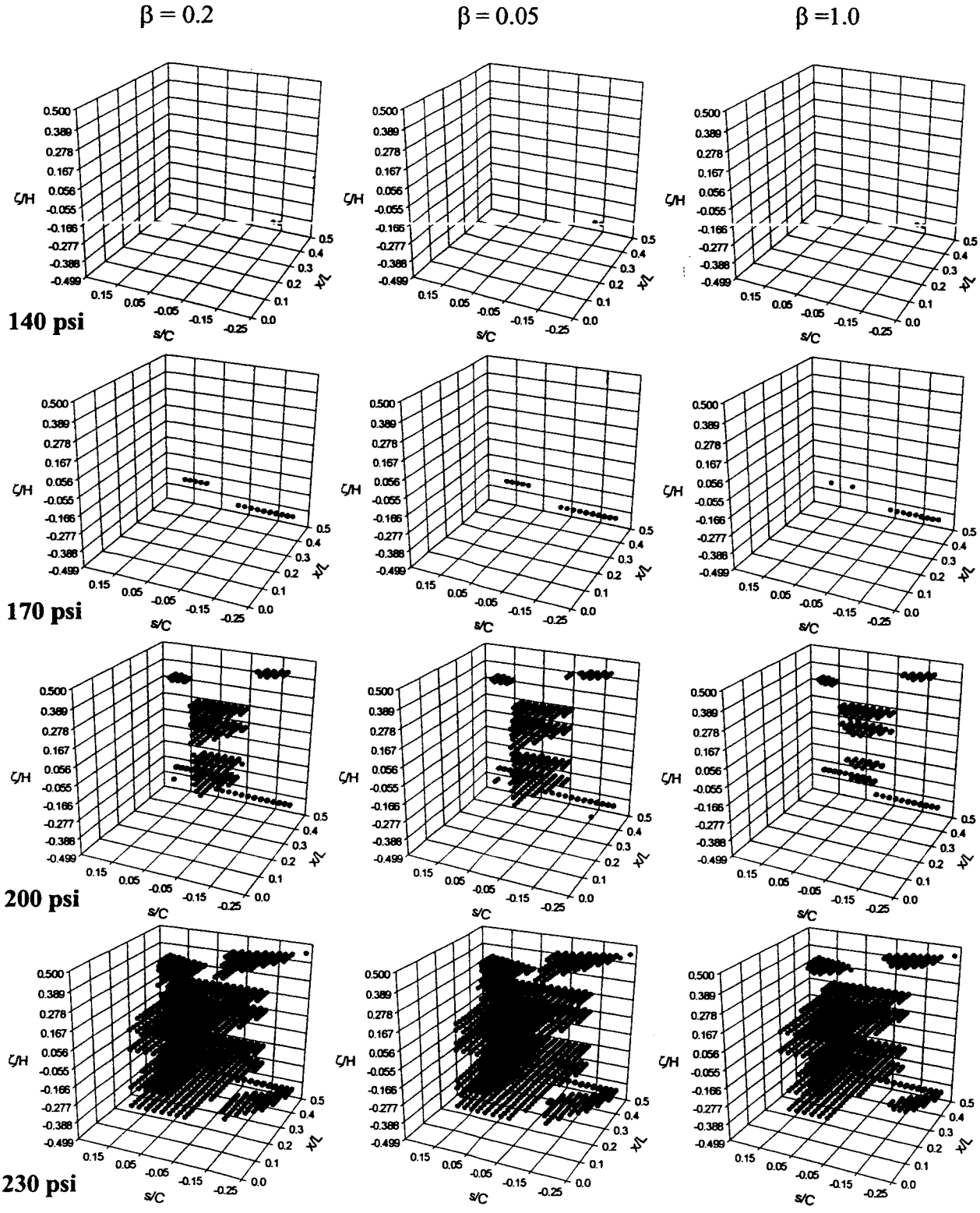

Figure 3.11 Effects of degradation factors on the matrix cracking scenario for the axially-stiff $[\pm 45/0_2/90_{1/2}]_s$ elliptical cylinder, maximum stress criterion, baseline degradation scheme

3.7 Effects of Recursive Degradation on the Matrix Failure Scenarios

All the degradation schemes investigated up to this point involved the non-recursive degradation of the engineering properties. In a non-recursive degradation, at a given pressure load, the engineering properties at the integration points where failure is detected are multiplied by the factor β when the failures are encountered. In a recursive degradation, the engineering properties are again multiplied by β at each subsequent pressure level. For example, if at the first pressure step, failures are detected, the properties at those failed points are multiplied by β. At the second pressure step, if additional failures are found, the newly failed points are multiplied by β and the previously failed points are multiplied by β^2. To investigate the effects of the recursive degradation on the matrix failure scenarios for the cylinders studied, the cracking maps obtained by using the PFA option with a recursive degradation of E_2, G_{12}, ν_{12}, and ν_{21} by a factor of β=0.2 are compared to the results using the baseline degradation scheme with β=0.2. All results are based on the maximum stress criterion. It should be noted that use of the recursive scheme results in the degree of degradation depending directly on the number of steps taken to reach the final pressure, i.e., 5 psi increments or 10 psi increments. Wether or not this is an issue could be problem dependent.

For the quasi-isotropic cylinder, Fig. 3.12 shows the comparisons between the cracking maps for the non-recursive and the recursive degradation schemes with β=0.2. Following the format of the previous sections, in the left column, the maps corresponding to the non-recursive degradation of the engineering properties are shown. The right column correspond to the recursive degradation of the properties. It is evident from the figure that the recursive degradation has, for all practical purposes, no effect on the failure scenarios for this cylinder. No easily noticeable differences can be detected from the maps. At the last two pressure levels, though difficult to see, there are a few additional cracks in the recursive case. Particularly, at 200 psi, in the right hand side map, there can be seen additional cracking in the innermost 90° layer at $s/C \approx -0.25$. At 230 psi, the recursive case shows a few additional cracks in the inner +45° layer near $s/C = -0.15$. However, the differences between the failure maps are insignificant. In fact, the first fiber failure pressures and associated percent damage, as indicated in Table 3.5, suggest that this cylinder is not affected by the recursive degradation.

In Fig. 3.13, the matrix failure scenarios for the non-recursive and recursive degradations for the circumferentially-stiff cylinder are shown. From the figure, it is fair to say that, for this cylinder, there are also no significant differences between both schemes; although, in general, the maps for the recursive degradation exhibit additional cracking. Specifically, at 170 psi additional cracking can be seen in the inner -45° layer near the side $s/C=+0.25$ in the map for the recursive case. At 200 psi, also, a few more failures can be observed in the map for the recursive case, in particular, in the inner $\pm 45^{\circ}$ layers at both sides near the clamped end. A similar observation can be made at 230 psi, where, in layer 3 near the sides at the clamped end, more cracks have progressed circumferentially for the recursive degradation. However, quantitatively, the pressure and percent damage at first fiber failure listed in Table 3.5 indicates that there is no significant difference between the two degradation schemes for the circumferentially-stiff cylinder.

At a glance, the matrix failure scenarios for the axially-stiff cylinder shown in Fig. 3.14 suggest that, as for the other two cylinders, there is no significant difference between recursive and non-recursive degradation. However, by a close observation, the amount of damage for the axially-stiff cylinder due to the recursive degradation is more pronounced than for the other two cylinders. At 200 psi and 230 psi, several more failures can be observed in the maps for the recursive case. At 200 psi for the recursive case, in the crown area in the 0° layers there are more failures that have progressed axially. In the right hand side map at 230 psi, there are even more failures that have progressed axially and circumferentially. Though difficult to see, this occurs in the top two layers near the crown. Note that the gap between the two clusters of failures in the outer $\pm 45^{\circ}$ layers is smaller for the recursive case, indicating a larger amount of damage in the area surrounding the gap. In the inner $+45^{\circ}$ layer for the recursive case, it can be seen that there is an additional line of cracks in the axial direction near $s/C=-0.05$. From the values listed in Table 3.5, it becomes clear that for the axially-stiff cylinder, recursive degradation results in more damage at first fiber failure and that the pressure at which first fiber failure occurs is lower than for non-recursive degradation.

Table 3.5: Effects of recursive degradation on first fiber failure pressures and percent damage, maximum stress criterion, β=0.2

Degradation	Non-recursive		Recursive	
Cylinder orthotropy	First fiber failure pressure, psi	Percent damage[a]	First fiber failure pressure, psi	Percent damage[a]
quasi-isotropic	246	5.5	245	5.4
circumferentially-stiff	253	6.9	252	7.0
axially-stiff	251	26.5	249	27.2

a. Number of failed integration points / total number of integration points

For the recursive degradation for all three cylinders, STAGS took considerably longer time to run. The number of iterations needed for the analysis to converge was larger than for the non-recursive degradation. In particular, for the axially-stiff cylinder, the number of iterations, at the higher pressure levels, was above 30, close to the maximum number of iterations allowed by STAGS using the default settings for convergence.

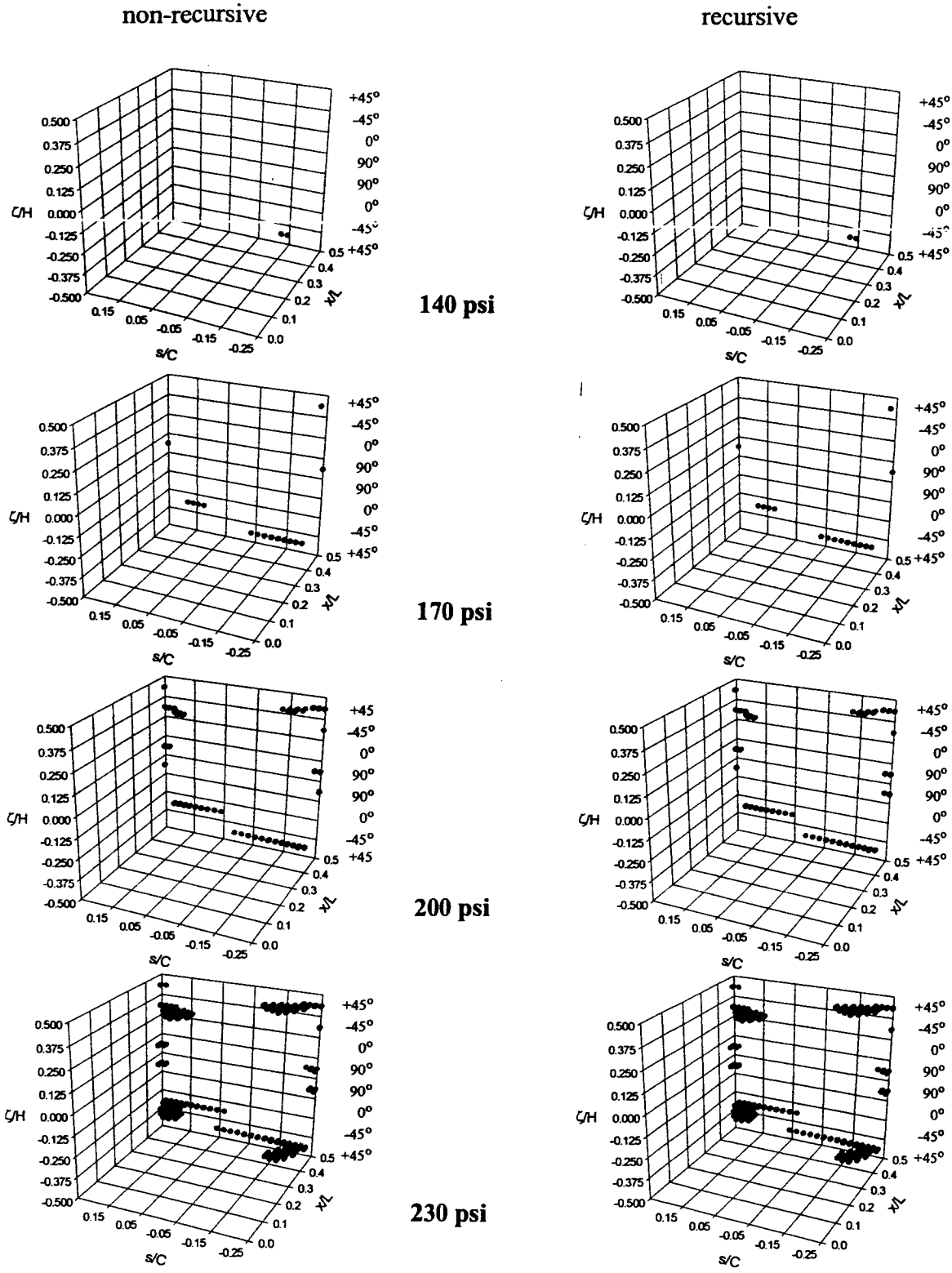

Figure 3.12 Effect of recursive degradation on the matrix cracking scenario for the quasi-isotropic $[\pm 45/0/90]_s$ elliptical cylinder, maximum stress criterion, β=0.2

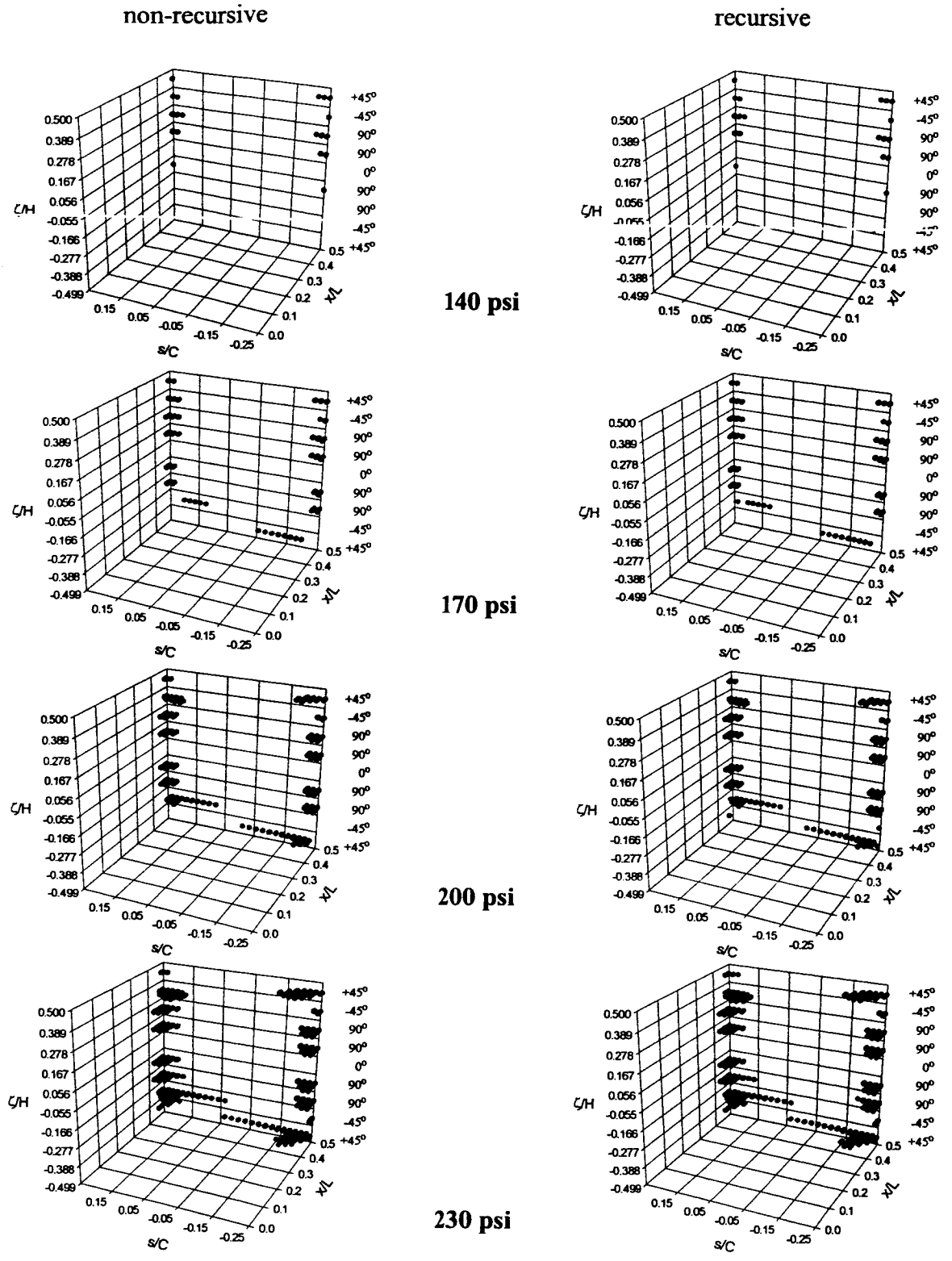

Figure 3.13 Effect of recursive degradation on the matrix cracking scenario for the circumferentially-stiff $[\pm 45/90_2/0_{1/2}]_s$ elliptical cylinder, maximum stress criterion, β=0.2

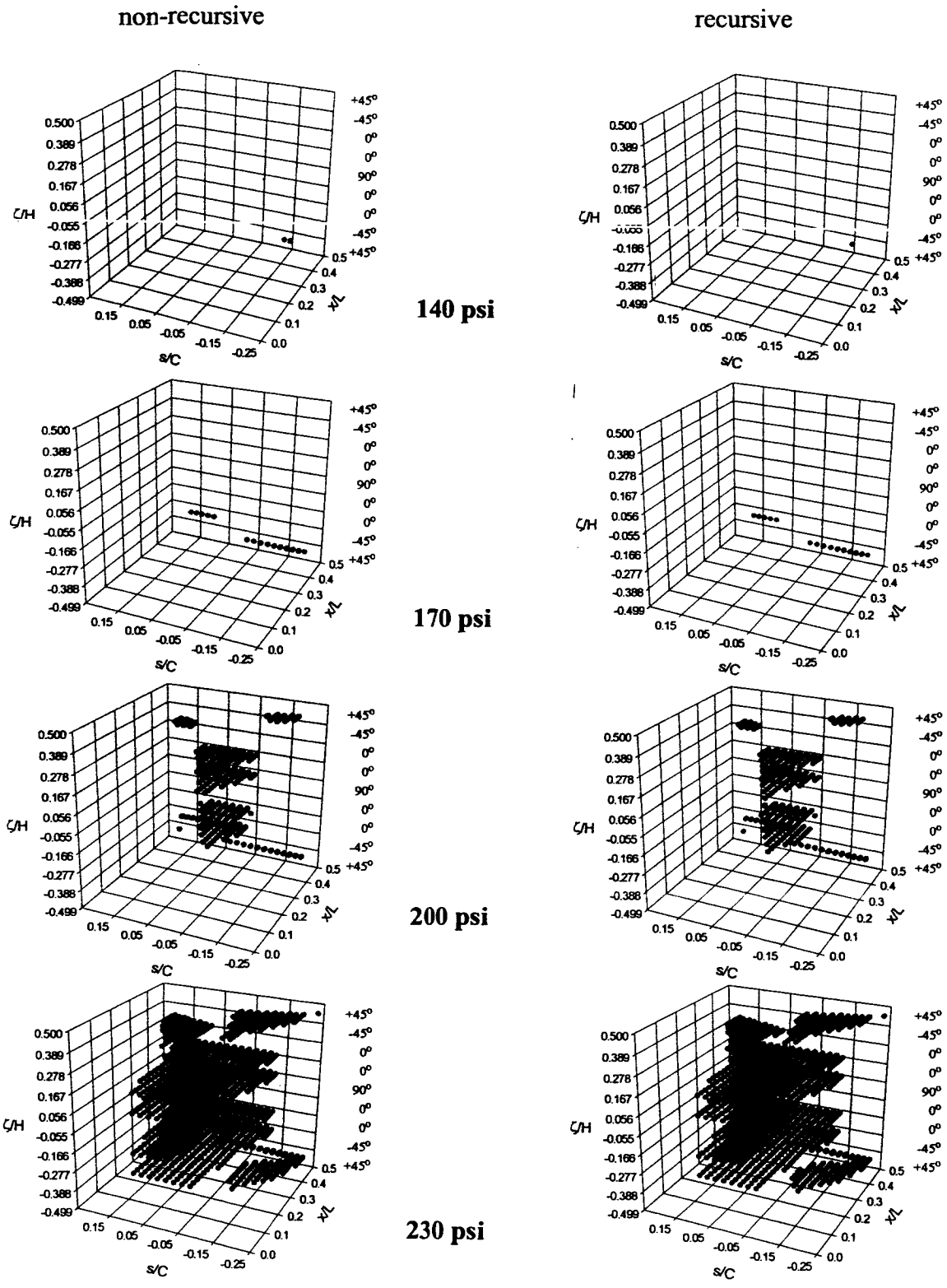

Figure 3.14 Effect of recursive degradation on the matrix cracking scenario for the axially-stiff $[\pm 45/0_2/90_{1/2}]_s$ elliptical cylinder, maximum stress criterion, β=0.2

3.8 Evaluation of Computational Algorithms

A point that can be made at this time is that, in obtaining the results presented here, the PFA in STAGS used a specific computational algorithm to compute the stiffness matrix components. This algorithm uses the extensional moduli, E_1 and E_2, in a particular fashion in the computation of the stiffness matrix components. Specifically, using STAGS notation in the principal material coordinate system, the stiffness matrix, which is orthotropic, is given by

$$\begin{bmatrix} cm(1) & cm(4) & 0 \\ cm(2) & cm(5) & 0 \\ 0 & 0 & cm(9) \end{bmatrix} \tag{3.4}$$

where the components are computed as follows:

$$\begin{aligned} cm(1) &= \frac{1}{\Delta \cdot E_2} \\ cm(2) &= \frac{\nu_{12}}{\Delta \cdot E_2} \\ cm(4) &= cm(2) \\ cm(5) &= \frac{1}{\Delta \cdot E_1} \\ cm(9) &= G_{12} \end{aligned} \tag{3.5}$$

with

$$\Delta = \frac{1 - \nu_{12} \cdot \nu_{21}}{E_1 \cdot E_2} \tag{3.6}$$

and

$$\nu_{21} = \nu_{12} \cdot \left(\frac{E_2}{E_1}\right)^o \tag{3.7}$$

where the superscript 'o' indicates that the ratio is based on original, or undegraded, values of the extensional moduli. (Note: Equation (3.7) is another way of stating, as was stated in Table 2.1, that both Poisson's ratios are degraded when failure is encountered.) This algorithm can encounter numerical singularities if the degradation factor β is very small, or is set to zero to completely eliminate either extensional moduli. Although by defining ν_{21} using the undegraded ratio helps to prevent ν_{21} from becoming zero or infinity when the degradation factor β is set to zero, the

expression for Δ in Eq. (3.6) becomes very large if either moduli is very small, and infinity if either moduli is reduced to zero. In a number of programming languages, including FORTRAN, which is the language STAGS utilizes, the very large or infinity value results in a computational error, sometimes referred to as overflow. Two options that were recently implemented in STAGS circumvent this computational problem.

The first option, which will be referred to as option 1, defines Δ without using the extensional moduli and computes the matrix components in a different manner than in Eq. (3.5). Specifically, this option defines the stiffness matrix components as follows:

$$\begin{aligned} cm(1) &= \frac{E_1}{\Delta} \\ cm(4) &= \frac{\nu_{12} \cdot E_2}{\Delta} \\ cm(2) &= cm(4) \\ cm(5) &= \frac{E_2}{\Delta} \\ cm(9) &= G_{12} \end{aligned} \tag{3.8}$$

with

$$\Delta = 1 - \nu_{12} \cdot \nu_{21} \tag{3.9}$$

With this approach, setting either extensional moduli to zero presents no particular computational problem.

With the second option, option 2, the components of the undegraded stiffness matrix are multiplied by a factor of β. The factor β multiplies the row and column of the stiffness matrix corresponding to a particular mode of failure. For example, if tensile or compressive matrix failure is detected, the elements of the second row and second column of the stiffness matrix are multiplied by β. That is, for matrix failure, the stiffness matrix is written as

$$\begin{bmatrix} cm(1) & \beta \cdot cm(4) & 0 \\ \beta \cdot cm(2) & \beta \cdot cm(5) & 0 \\ 0 & 0 & \beta \cdot cm(9) \end{bmatrix} \tag{3.10}$$

If fiber tensile or compressive failure is encountered, the stiffness matrix is then given by

$$\begin{bmatrix} \beta \cdot cm(1) & \beta \cdot cm(4) & 0 \\ \beta \cdot cm(2) & cm(5) & 0 \\ 0 & 0 & \beta \cdot cm(9) \end{bmatrix} \tag{3.11}$$

If shear failure occurs, Eq. (3.4) becomes

$$\begin{bmatrix} cm(1) & cm(4) & 0 \\ cm(2) & cm(5) & 0 \\ 0 & 0 & \beta \cdot cm(9) \end{bmatrix} \tag{3.12}$$

With option 2, the overflow problem is not an issue since the definition of the components *cm* are defined using the undegraded moduli.

To assess the influence of different computational algorithms on the results corresponding to the baseline degradation scheme, with β=0.2, and using the maximum stress criterion, Table 3.6 shows the number of iterations needed for convergence and percent damage at different pressure levels for the three cylinders. As can be seen from the table, no significant differences between the three options can be observed for the quasi-isotropic cylinder. In fact, for all practical purposes, all options go through the same number of iterations and find the same percent damage. For the circumferentially-stiff cylinder, the number of iterations varies with algorithm. However, it is difficult to determine which option goes through the least number of iterations, since there is not a clear trend in one direction or the other. Though the difference is not significant, option 2 finds the least amount of damage for this cylinder. For the axially-stiff cylinder, the number of iterations and percent damage also depend on the algorithm. As for the circumferentially-stiff cylinder, it is difficult to determine which option goes through the least amount of iterations to converge, although at the last two pressure levels, option 1 goes through more iterations. It should be mention that in running the three options for the axially-stiff cylinder, the extended number of iterations (40 maximum) was used. Recall that the default option had to be extended from 22 maximum iterations to 40 maximum at 190 psi. It should be stated that in the range from 190 to 240 psi, the extension was needed with all options, since the number of iterations was larger than 22 at certain pressures. For this cylinder, the difference in percent damage between option 2 and the other two options is more evident than the difference found for the circumferentially-stiff cylinder, particularly, at the last four pressure levels.

Figures 3.15, 3.16, and 3.17 show, respectively, the matrix cracking scenarios at different pressure levels for the quasi-isotropic, circumferentially-stiff, and axially-stiff cylinders obtained using all three computational algorithms. As can be seen from figures 3.15 and 3.16, there are no significant differences between the options for the quasi-isotropic and circumferentially-stiff cylinders. This observation emphasizes the fact, seen in Table 3.6, that all three options predicted practically the same amount of damage in these cylinders. In the matrix cracking maps for the axially-stiff cylinder, shown in Fig. 3.17, noticeable differences can be observed between option 2 and the other two options. The maps associated with option 2, at 220 and 240 psi, exhibit the least amount of cracking, as also indicated in Table 3.6 by the difference in percent damage. The default option and option 1 exhibit no significant differences. Table 3.7 shows the first fiber failure pressures and associated percent damage. Interestingly, all options, at the first fiber failure pressures, predict basically the same amount of damage for the three cylinders. However, with option 2 the first fiber fails at a higher pressure than with the default and option 1.

Table 3.6: Effects of computational algorithms on the number of iterations and percent damage, maximum stress criterion, baseline degradation scheme, β=0.2

Cylinder orthotropy	Option	Default		1		2	
	Pressure	Number of iterations	Percent damage[a]	Number of iterations	Percent damage[a]	Number of iterations	Percent damage[a]
quasi-isotopic	140	2	0.0	2	0.0	2	0.0
	150	2	0.0	3	0.0	3	0.0
	160	3	0.1	3	0.1	3	0.1
	170	4	0.2	3	0.2	3	0.2
	180	3	0.4	3	0.4	3	0.4
	190	4	0.6	4	0.6	3	0.6
	200	4	1.0	4	1.0	5	1.0
	210	7	1.8	7	1.8	6	1.8
	220	7	2.8	6	2.8	5	2.8
	230	7	3.9	6	3.9	7	3.8
	240	8	4.9	7	4.9	7	4.9

Table 3.6: Effects of computational algorithms on the number of iterations and percent damage, maximum stress criterion, baseline degradation scheme, β=0.2

Cylinder orthotropy	Option	Default		1		2	
	Pressure	Number of iterations	Percent damage[a]	Number of iterations	Percent damage[a]	Number of iterations	Percent damage[a]
circumferentially-stiff	140	3	0.3	4	0.3	3	0.3
	150	4	0.6	5	0.5	4	0.5
	160	8	0.9	8	0.9	7	0.9
	170	6	1.3	5	1.3	7	1.2
	180	10	1.8	18	1.8	6	1.7
	190	7	2.3	6	2.4	6	2.2
	200	6	3.0	6	3.0	6	2.9
	210	6	3.8	8	3.8	8	3.6
	220	6	4.4	9	4.5	7	4.3
	230	8	5.2	10	5.2	7	5.0
	240	8	5.9	10	5.9	14	5.8
axially-stiff	140	2	0.0	2	0.0	2	0.0
	150	2	0.0	3	0.0	2	0.0
	160	2	0.1	3	0.1	3	0.1
	170	3	0.2	3	0.2	3	0.2
	180	3	0.3	3	0.3	3	0.3
	190	24	0.9	17	0.9	5	0.9
	200	18	4.2	18	4.2	21	4.2
	210	22	10.6	27	10.6	18	10.0
	220	29	15.3	26	15.3	26	14.7
	230	19	19.4	30	19.4	25	18.4
	240	25	22.6	28	22.6	20	21.5

a. Number of failed integration points / total number of integration points

Table 3.7: Effects of computational algorithms on first fiber failure pressures and percent damage, maximum stress criterion, baseline degradation scheme, β=0.2

Option	Default		Option 1		Option 2	
Cylinder	First fiber failure pressure, psi	Percent damage[a]	First fiber failure pressure, psi	Percent damage[a]	First fiber failure pressure, psi	Percent damage[a]
quasi-isotropic	246	5.5	246	5.5	247	5.5
circumfere-tially-stiff	253	6.9	253	6.9	255	6.8
axially-stiff	251	26.5	250	26.4	254	26.4

a. Number of failed integration points / total number of integration points

3.9 Summary of Matrix Failure Scenarios in Internally Pressurized Elliptical Cylinders Using Different Degradation Schemes

In this chapter, the matrix failure scenarios for an elliptical cylinder with quasi-isotropic $[\pm 45/0/90]_s$, circumferentially-stiff $[\pm 45/90_2/0_{1/2}]_s$, and axially-stiff $[\pm 45/0_2/90_{1/2}]_s$ material orthotropies were investigated. The PFA was configured to use the maximum stress failure criterion with various degradation schemes. The mode of failure for all cases considered was found to be due to excessive tension in the direction perpendicular to the fibers. The pressure and locations of the initial matrix failures were found to depend on the material orthotropy. After initial failure, as the pressure was increased, it was found that the quasi-isotropic and circumferentially-stiff cylinders developed similar cracking patterns, although the pressure and the amount of damage when first fiber failure occurred was higher for the circumferentially-stiff cylinder. The axially-stiff cylinder exhibited a significant amount of damage. The damage developed rapidly after about 180 psi. The damage was so dramatic that the default algorithm of the PFA, which allows for 22 iterations for convergence, had to be extended to 40 iterations to converge. The percent damage at first fiber failure was approximately 26.5%. These value was about 5 and 4 times larger than for the quasi-isotropic and circumferentially-stiff cylinders, respectively. For all three cylinders, it was determined that up to first fiber failure, no leakage paths developed because there always remained at least one uncracked layer in the cylinder wall. All these findings agreed well

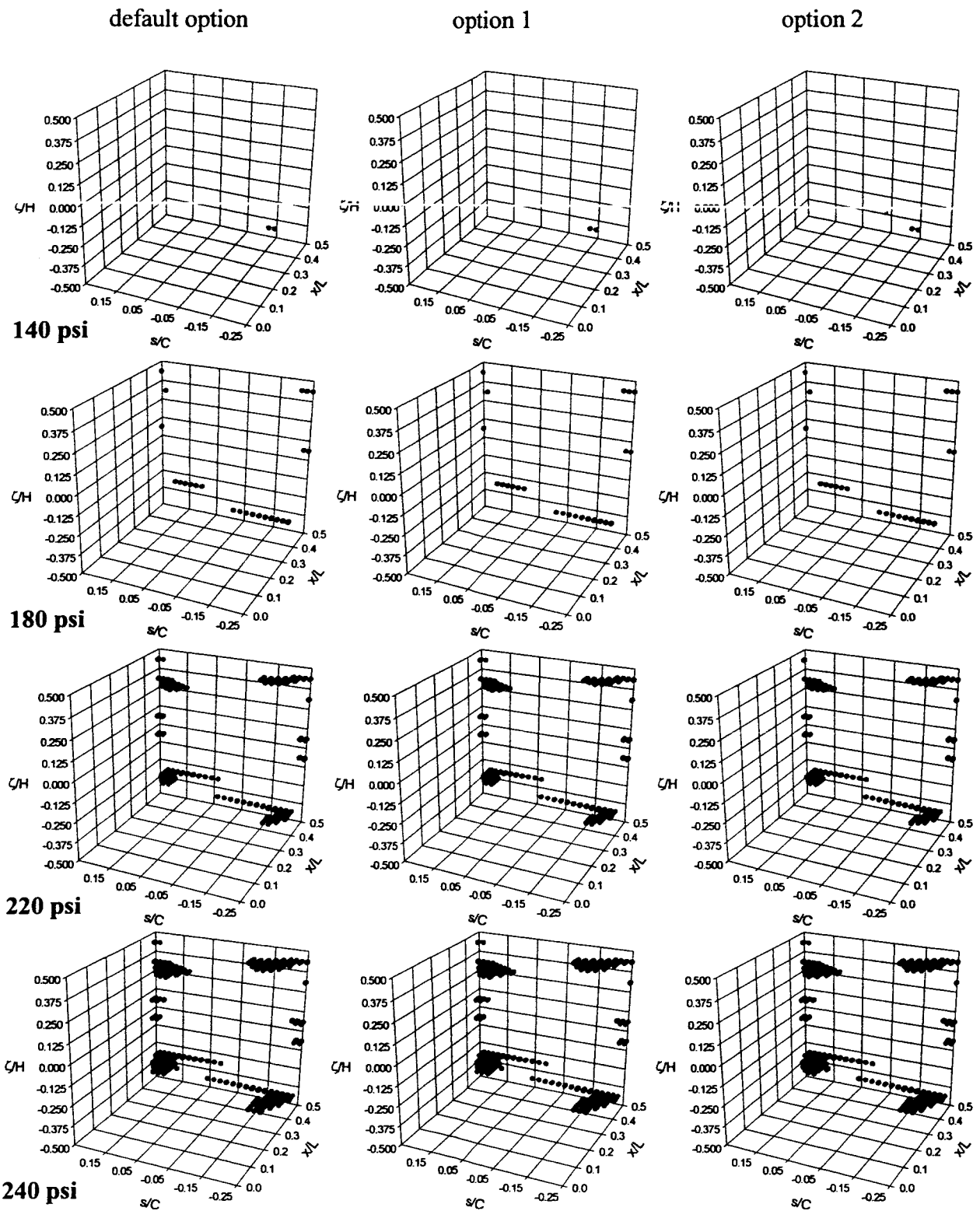

Figure 3.15 Matrix cracking scenarios for the quasi-isotropic $[\pm 45/0/90]_s$ elliptical cylinder, maximum stress criterion, baseline degradation scheme, β=0.2, different computational algorithms

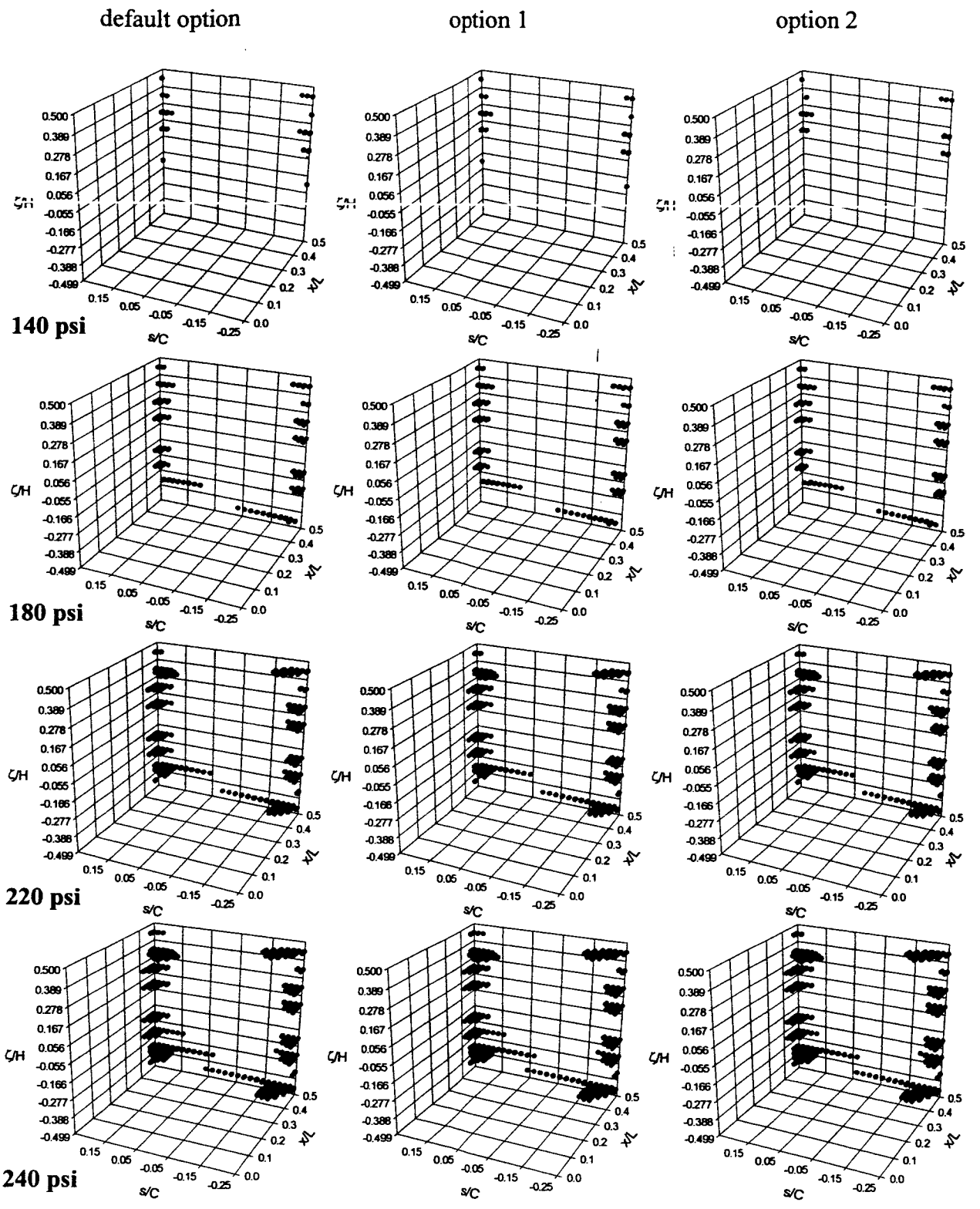

Figure 3.16 Matrix cracking scenarios for the circumferentially-stiff $[\pm 45/90_2/0_{1/2}]_s$ elliptical cylinder, maximum stress criterion, baseline degradation scheme, β=0.2, different computational algorithms

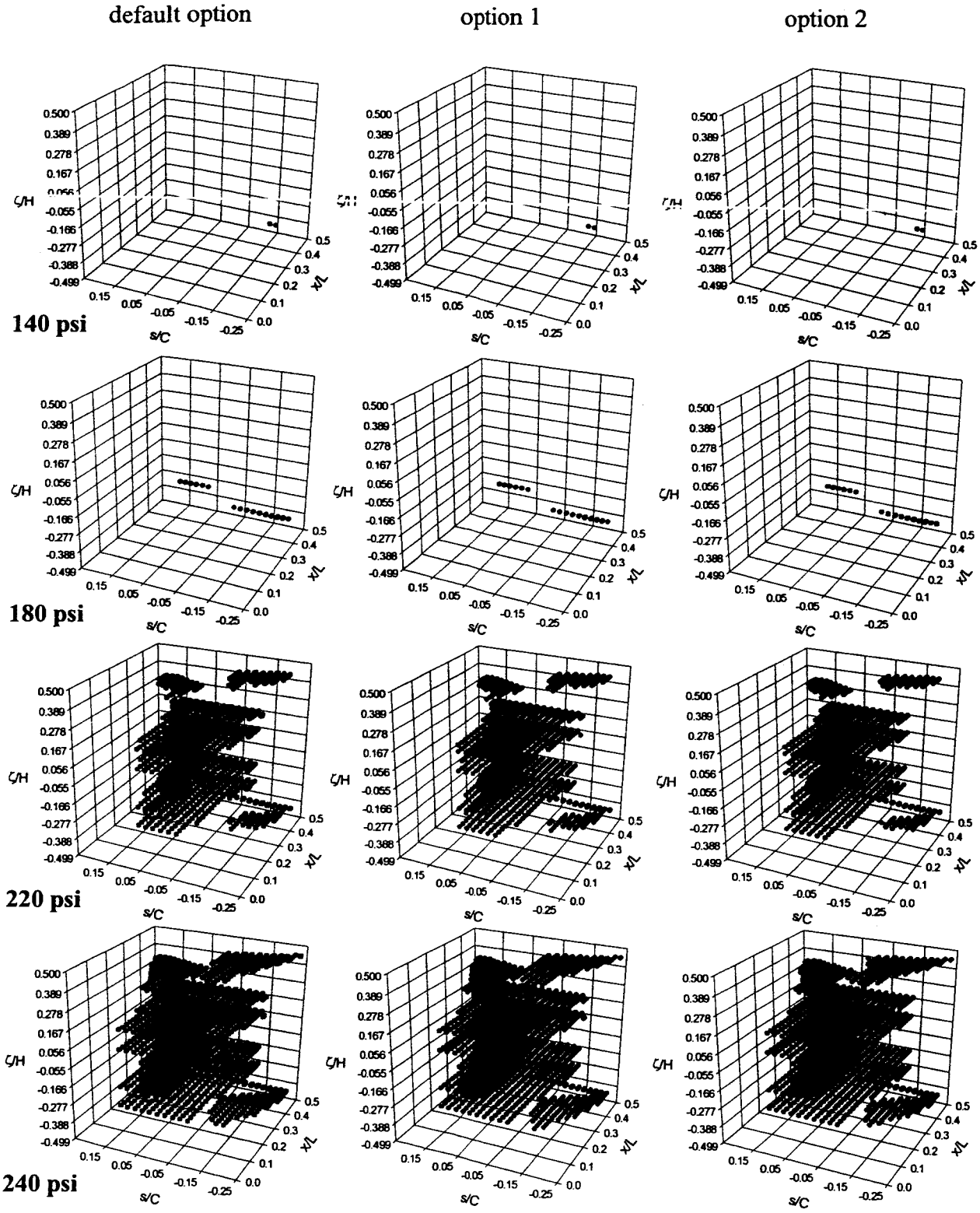

Figure 3.17 Matrix cracking scenarios for the axially-stiff $[\pm 45/0_2/90_{1/2}]_s$ elliptical cylinder, maximum stress criterion, baseline degradation scheme, β=0.2, different computational algorithms

with previous works that characterized the behavior and failure of internally pressurized elliptical composite cylinders.

With respect to the importance of the inplane shear modulus degradation, it was found that by neglecting the shear modulus in the degradation process there was no difference in the matrix cracking scenario for the quasi-isotropic cylinder. For the circumferentially-stiff and axially-stiff cylinders, not reducing the shear modulus caused slightly less damage and the first fiber failure pressure was found to be slightly higher than the case where the inplane shear modulus was degraded.

The matrix cracking scenarios associated with different degradation factors; specifically, β=0.05, β=0.2, and β=1.0, or no degradation, indicated that the larger the reduction of the engineering properties, the larger the amount of damage. However, the effect was not overly pronounced, and this trend was not exactly valid for the quasi-isotropic cylinder. The percent damage when first fiber failure occurred for the quasi-isotropic cylinder was precisely the same for each value of β considered. The pressure at which first fiber failure occurred, however, was highest for the case of no degradation and lowest for the lowest value of β. The other two cylinders were found to be more sensitive to the value of β. The first fiber failure pressure for the circumferentially-stiff as well as for the axially-stiff cylinder was found to increase with larger β. The percent damage at those pressures actually decreased as β increased. It was interesting to find that for the axially-stiff cylinder and the lowest value of β, which led to the largest percent damage at first fiber failure, there still remained an uncracked layer, impeding the formation of a leakage path.

In regard to the effects of recursive degradation of engineering properties, it was found that a recursive degradation had an effect similar to the effect of severely reducing the engineering properties. This was the case because in a recursive degradation the engineering properties are multiplied by the factor β at each load step. For the quasi-isotropic cylinder, it was found that there were no significant differences between the cracking maps for a recursive and non-recursive degradation. The failure maps for the circumferentially-stiff and axially-stiff cylinders exhibited more cracking when a recursive degradation was performed. For the quasi-isotropic and circumferentially-stiff cylinders, the first fiber failure pressures and percent damage were practically

unaffected by the recursive degradation. For the axially-stiff cylinder, the first fiber failure pressure was found to be lower than the respective pressure for the non-recursive case, and the percent damage at first fiber failure was higher for the recursive degradation case.

Finally, the issue of different computational algorithms within the PFA in STAGS was addressed. Because the default algorithm in STAGS may cause a numerical overflow problem if the engineering properties are multiplied by a small or zero value of β, two optional algorithms in STAGS may be used to prevent the numerical singularities. The number of iterations for convergence, the percent damage, and the cracking patterns were found to depend to some degree on the computational algorithm used. However, the differences were not significant and one computational scheme was not found to be superior.

Chapter 4 Matrix Failure Scenarios in Internally Pressurized Elliptical Cylinders Using Different Failure Criteria

Up to this point, the investigation of the matrix failure scenarios for the elliptical cylinders studied has focused on the use of the maximum stress criterion, which is a non-interactive criterion. In a non-interactive failure criterion, the conditions of failure only involve one stress component. It is believed that if the matrix failure scenarios are predicted by interactive failure criteria, which account for the interaction of different stress components, perhaps more cracking would be predicted. If that is the case, a leakage path could be predicted to form before the first fiber fails. To investigate if that occurs and assess to what extent the failure predictions depend on the failure criterion used, the failure scenarios resulting from using the Hashin and Tsai-Wu failure criteria, which are interactive criteria, will be compared to the scenarios provided by the maximum stress criterion.

4.1 Comparison Between the Maximum Stress and Hashin Failure Criteria

For the Hashin and the maximum stress criteria, the PFA option was set to use the baseline degradation scheme with β=0.2. The maximum stress criterion predictions were discussed previously. Interestingly, up to first fiber failure the Hashin criterion predictions were comprised of only matrix tensile failures, so all the results presented here involve matrix cracking. The conditions for matrix tensile failure for the maximum stress and Hashin criteria were defined in Eq. (2.6) and Eq. (2.11), respectively.

Figure 4.1 shows the matrix failure maps at different pressure levels for the quasi-isotropic cylinder. The left column of the figure shows the failure maps corresponding to the maximum

stress criterion. These maps were last shown in the left column of Fig. 3.15. The right column displays the failure maps predicted by the Hashin criterion. As can be seen, the suspicion that more cracking would be predicted by the interactive criterion is confirmed in this case. At 140 psi it can be observed that the Hashin criterion predicts two additional failures relative to the predictions of the maximum stress criterion. The initial matrix failure pressure according to that criterion occurs at approximately 134 psi. This pressure is lower than the pressure predicted by the maximum stress criterion, as indicated in Table 4.1. The locations of the initial matrix failure, however, are predicted to be the same by both criteria. At 170 psi, again more failures are predicted by the Hashin criterion, particularly, in the outer ±45° layers. Also, cracks in the inner ±45° layers have progressed further circumferentially in the right hand side map. At the next pressure level, 200 psi, the same trend can be seen, however, the failure distribution predicted by both criteria looks very similar. In the right hand side map more cracking occurs in the outer +45° layer at $s/C \approx +0.25$, as well as in the 90° layer just inside the midsurface at both sides. The differences between the maps, however, are somewhat difficult to detect. At 230 psi, more axial and circumferential progression of matrix cracks are predicted by the Hashin criterion than by the maximum stress criterion. This can be seen in the outer –45° layer near $s/C=+0.15$, in the inner +45° layer in the region of $s/C=-0.15$, and in the inner ±45° layers, where more overlapping of cracks occurs near the crown. The fact that the Hashin criterion predicts more damage at every pressure level than the maximum stress criterion is further confirmed by the percent damage at the first fiber failure pressure, as indicated in Table 4.2. Interestingly, both criteria predict the same first fiber failure pressure for the quasi-isotropic cylinder. Evidently, though the Hashin criterion predicts a higher percentage of damage, the failure distribution is very similar to the one predicted by the maximum stress criterion. Consequently, in the Hashin criterion predictions the two 0° layers remain uncracked, impeding the formation of a leakage path, as was the situation for the predictions of the maximum stress criterion.

Following the same format used in Fig. 4.1, fig 4.2 shows the matrix cracking scenarios predicted by both criteria for the circumferentially-stiff cylinder. The failure maps corresponding to the maximum stress criterion were last seen in the left column of Fig. 3.16. A close observation of Fig. 4.2 reveals that the Hashin criterion also predicts more damage at every pressure level for this

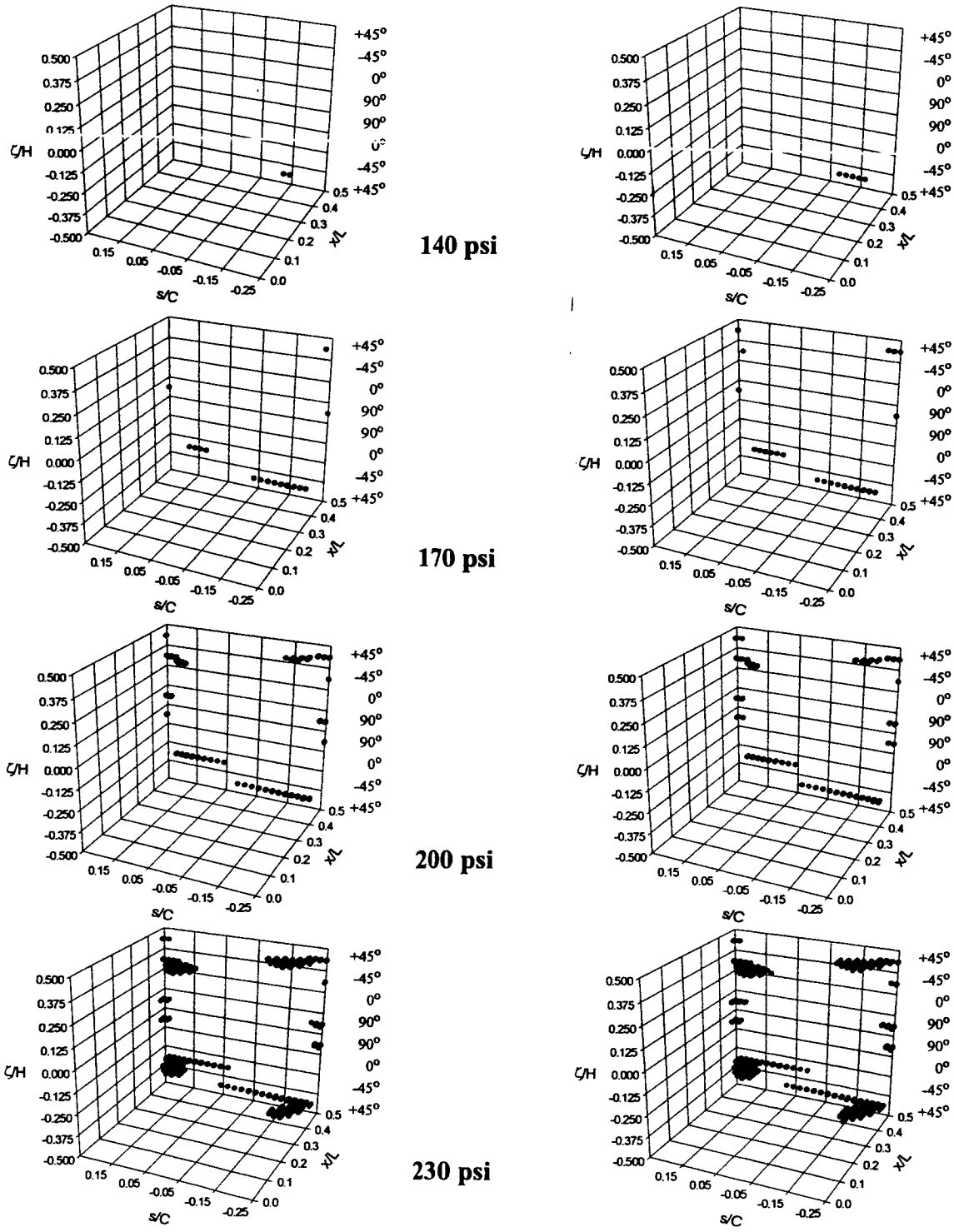

Figure 4.1 Matrix cracking scenarios for maximum stress and Hashin failure criteria for the quasi-isotropic $[\pm 45/0/90]_s$ elliptical cylinder, baseline degradation scheme, β=0.2

cylinder. Interestingly, unlike for the quasi-isotropic cylinder, where the initial matrix failure pressure predicted by the Hashin criterion was lower than that predicted by the maximum stress criterion, for this cylinder, both criteria predict the same initial matrix failure pressure, as indicated in Table 4.1. Figure 4.2 also shows that for the circumferentially-stiff cylinder both criteria predicts slightly different failure distributions. The additional cracks predicted by the Hashin criterion are mainly distributed in the circumferential direction. For example, at 140 psi, in the right hand side map, more circumferential progression of cracks can be observed in the $\pm 45^{\circ}$ layers near s/C=+0.25. Similar observations can be made for the remaining pressure levels. In particular, at 230 psi the circumferential progression of cracks predicted by the Hashin criterion is more obvious. Note the larger overlapping in the inner $\pm 45^{\circ}$ layers and the longer circumferential lines of cracks in the inner 90° layer. Regardless the larger amount of cracking and the different failure distribution predicted by the Hashin criterion, at 230 psi, the 0° layer can be seen to be uncracked. Interestingly, the Hashin criterion predicts that, up to first fiber failure, that layer remains uncracked. Therefore, no leakage path forms.

Figure 4.3 shows the failure predictions for the axially-stiff cylinder. The failure maps predicted by the maximum stress criterion were shown previously in the left column of Fig. 3.17. Here, again, more cracking can be seen in the failure maps predicted by the Hashin criterion. This observation becomes obvious, particularly at 200 and 230 psi, where more cracking can be seen in the right hand side maps. At these pressure levels the failure maps display similar failure distributions, but a larger amount of cracking occurs in all layers in the right hand side maps. Though it cannot be discerned from the map at 230 psi, the 90° layer in the failure scenario predicted by the Hashin criterion remains uncracked, regardless of the large damage elsewhere. In fact, up to first fiber failure the Hashin criterion predicts that the 90° layer remains crack-free, impeding the formation of a leakage path. Tables 4.1 and 4.2 list the initial matrix failure pressure and the first fiber failure pressure and associated percent damage.

An interesting observation from the results just discussed is that though the shear stress, τ_{12}, seems to influence the amount of damage predicted by the Hashin criterion, since that stress is involved in the matrix tensile failure condition of Eq. (2.11), degrading or not degrading the

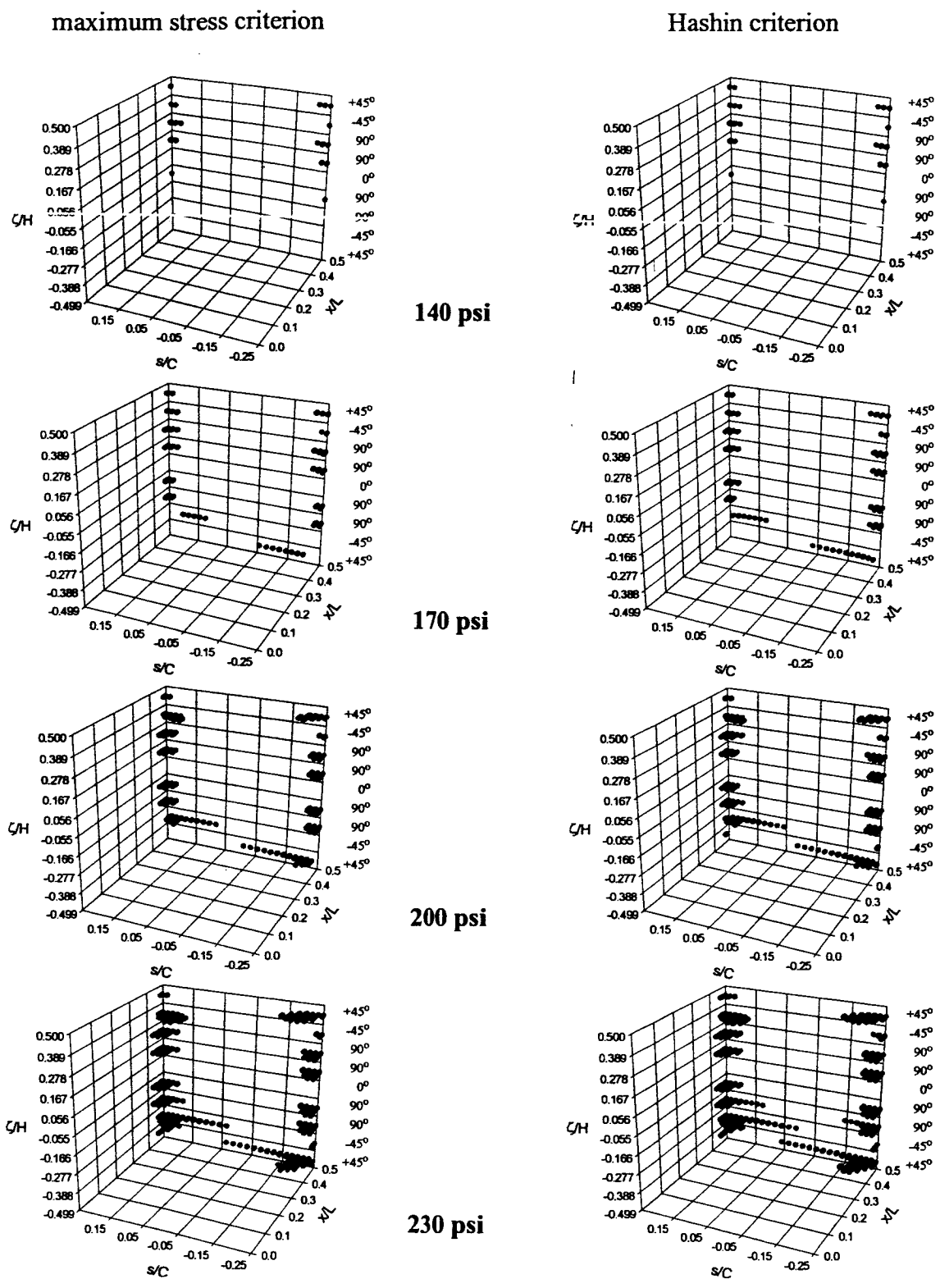

Figure 4.2 Matrix cracking scenarios for maximum stress and Hashin failure criteria for the circumferentially-stiff $[\pm 45/90_2/0_{1/2}]_S$ elliptical cylinder, baseline degradation scheme, β=0.2

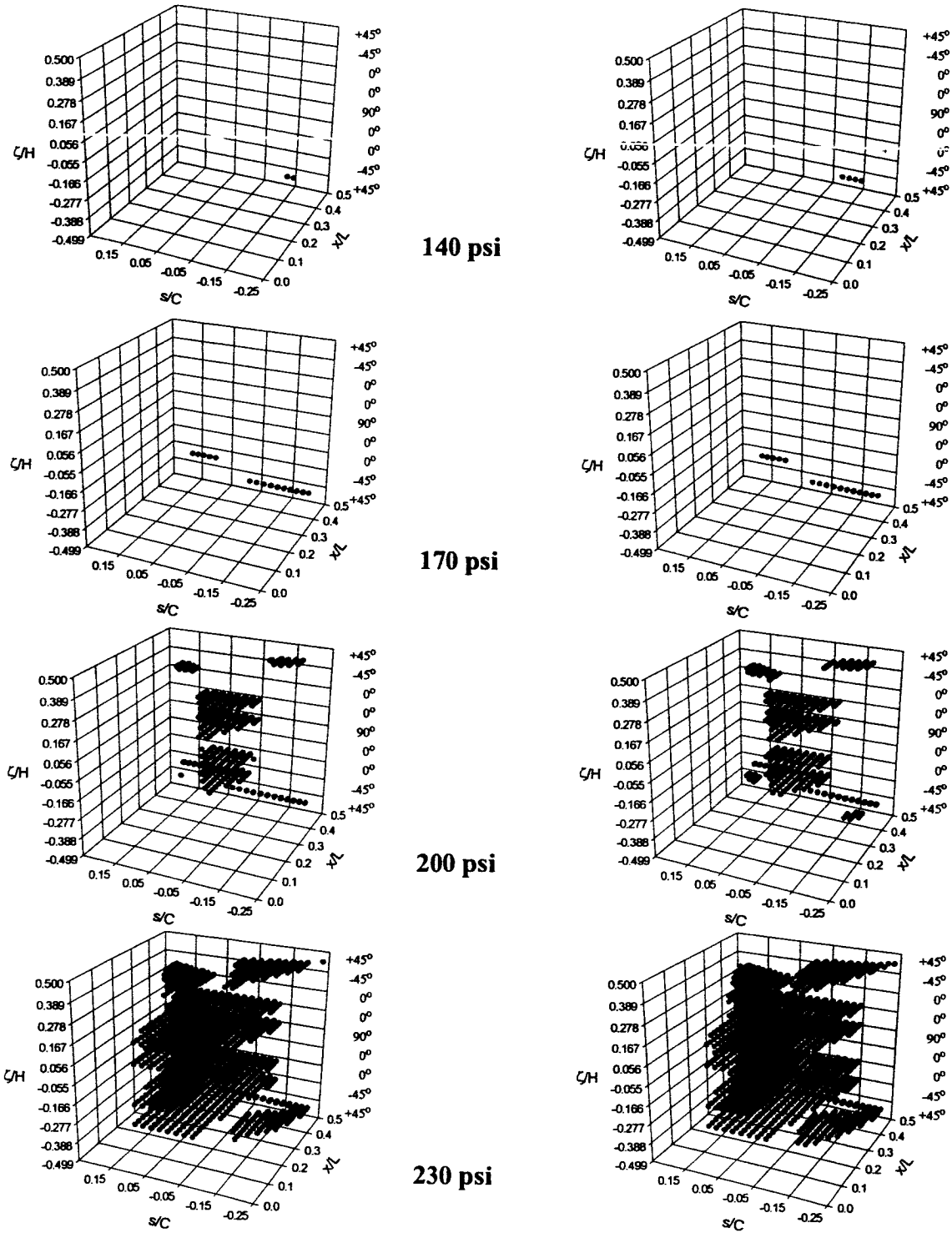

Figure 4.3 Matrix cracking scenarios for maximum stress and Hashin failure criteria for the axially-stiff $[\pm 45/0_2/90_{1/2}]_s$ elliptical cylinder, baseline degradation scheme, β=0.2

Table 4.1: Maximum stress and Hashin failure criteria predictions of initial matrix failure pressures

	First matrix failure pressure, psi	
Cylinder orthotropy	Maximum stress criterion	Hashin criterion
quasi-isotropic	138	134
circumferentially-stiff	105	105
axially-stiff	139	134

Table 4.2: Maximum stress and Hashin failure criteria predictions of first fiber failure pressures and percent damage, baseline degradation scheme, β=0.2

Criterion	Maximum Stress		Hashin	
Cylinder orthotropy	First fiber failure pressure, psi	Percent damage[a]	First fiber failure pressure, psi	Percent damage[a]
quasi-isotropic	246	5.5	246	6.2
circumferentially-stiff	253	6.9	250	7.5
axially-stiff	251	26.5	252	30.9

a. Number of failed integration points / total number of integration points

inplane shear modulus, G_{12}, as was seen in Figures 3.6, 3.7, and 3.8, did not seem to have a large impact when using the maximum stress criterion.

4.2 Comparison Between the Maximum Stress and Tsai-Wu Failure Criteria

As listed in Table 1, when using the Tsai-Wu failure criterion, the PFA option uses a degradation scheme that reduces recursively or non-recursively E_2, ν_{12}, and ν_{21} by a factor of β when matrix failure is detected. The shear modulus, G_{12}, is not reduced. The matrix failure scenarios predicted by the maximum stress criterion but not reducing G_{12} were previously discussed in section 3.5. Therefore, to assess the differences between the Tsai-Wu criterion and the maximum stress criterion, results for that section are compared with the results using the Tsai-Wu criterion. A factor of β=0.2 is used. Because the results obtained using the Tsai-Wu criterion predicted only matrix tensile failures, again, all the results presented here involve matrix cracking. The condition for matrix tensile failure for the Tsai-Wu criterion was defined in Eq. (2.17).

Figure 4.4 shows the matrix failure scenarios for the quasi-isotropic cylinder predicted using both failure criteria. The left column displays the failure maps predicted by the maximum stress criterion, while the right column shows the maps predicted by the Tsai-Wu criterion. The left column in Fig. 4.4 is the same as the right column of Fig. 3.6. As can be seen from the figure, as it was the case for the other interactive criterion, the Tsai-Wu criterion predicts more cracking at all pressure levels than the maximum stress criterion. However, unlike the Hashin and the maximum stress criteria, the Tsai-Wu criterion predicts the first fiber failure pressure to be lower than 230 psi. That is why the map at 230 psi in the right column is missing. The first matrix failure pressure found by the Tsai-Wu criterion is lower than the pressure found by the maximum stress criterion, as indicated in Table 4.3. From Fig. 4.4 it can also be seen that the failure distributions are different for the two criteria; however, the distribution predicted by the Tsai-Wu criterion at 200 psi looks similar to the one predicted by the maximum stress at 230 psi. Up to first fiber failure, the Tsai-Wu criterion also predicts that two layers remain uncracked. Thus no leakage path forms. Table 4.4 shows the first fiber failure pressures and percent damage values predicted by both criteria. The first fiber failure pressure predicted by the Tsai-Wu criterion is about 12% lower than that predicted by the maximum stress criterion. It is interesting to see that when first fiber failure occurs, according to the Tsai-Wu criterion, only 3.0% of the cylinder is damaged. This value is roughly half the percent damage predicted by the maximum stress criterion.

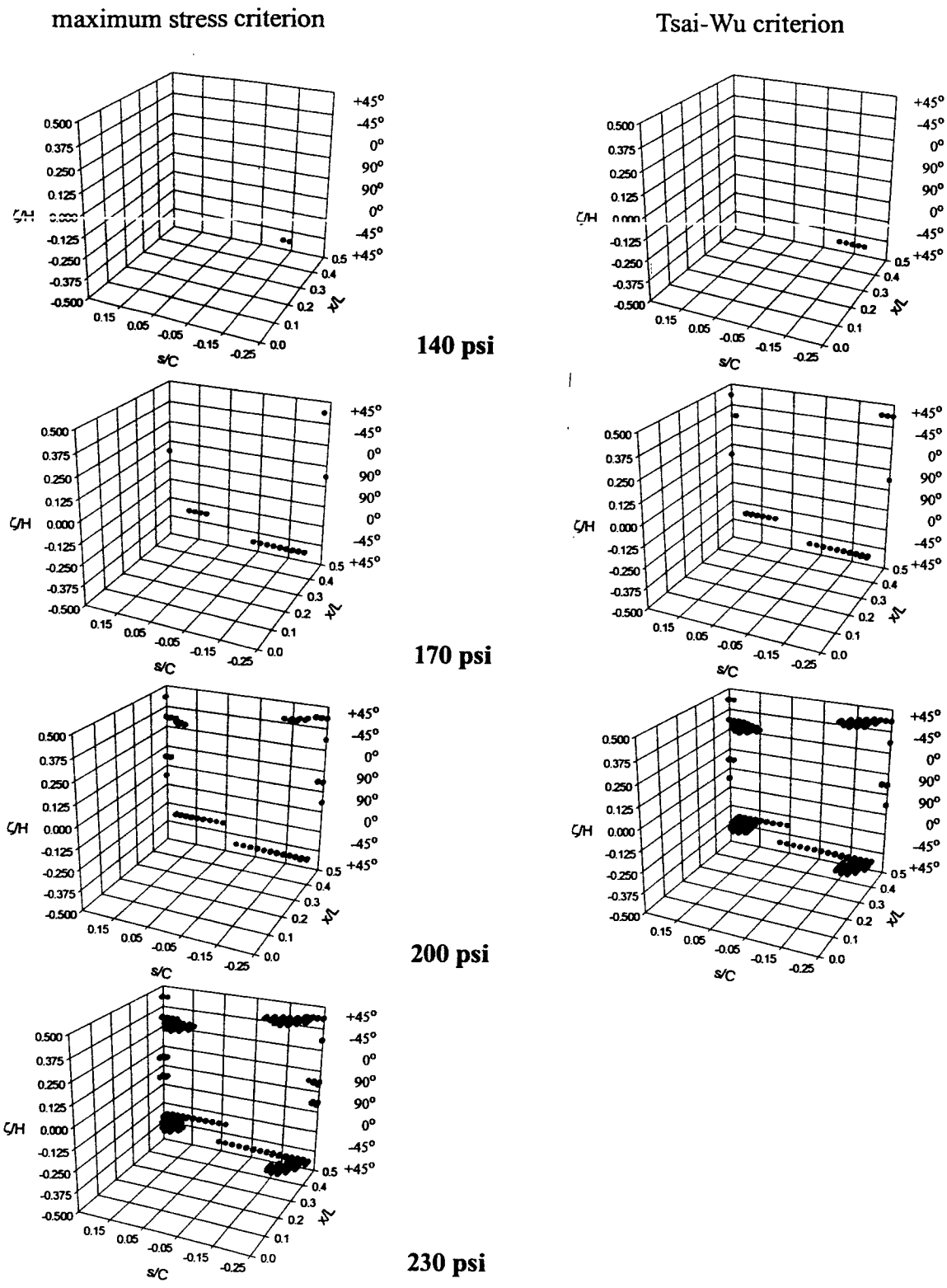

Figure 4.4 Matrix cracking scenarios for maximum stress and Tsai-Wu failure criteria for the quasi-isotropic $[\pm 45/0/90]_s$ elliptical cylinder, non-recursive degradation of E_2, ν_{12}, and ν_{21}, β=0.2

The matrix cracking predictions for the circumferentially-stiff cylinder are shown in Fig. 4.5. The figure shows that the Tsai-Wu criterion, again, predicts more matrix cracking than the maximum stress criterion, which is taken from the left hand column of Fig. 3.16, and a first fiber failure pressure lower than 230 psi. As indicated in Table 4.3, the initial matrix failure occurs at a similar pressure for both criteria. This was also the case when the Hashin criterion was used. Table 4.4 compares the first fiber failure pressures and associated percent damage. As can be seen from the table, the first fiber failure pressure predicted by the Tsai-Wu criterion is about 13% less than the pressure predicted by the maximum stress criterion. As it was found for the quasi-isotropic cylinder, the percent damage at first fiber failure predicted by the Tsai-Wu criterion is roughly half the value found by the maximum stress criterion.

Figure 4.6 shows the predictions for the axially-stiff cylinder. The results for the maximum stress criterion are taken from the left hand column of Fig. 3.17. For this cylinder, the Tsai-Wu criterion not only predicts more matrix cracking, but also a different failure distribution. At 140 psi, the maps look like the maps, in Fig. 4.4, for the quasi-isotropic cylinder at the same pressure. Also the first matrix failure pressures, as indicated in Table 4.3, were similar to the quasi-isotropic results. At 170 psi, the failure scenario predicted by the Tsai-Wu criterion exhibits more failures and a different failure distribution than the failure scenario predicted by the maximum stress. Notice that, in the right hand side map, there can be seen matrix cracks in the inner and outer $\pm 45^{\circ}$ layers away from the clamped end. At 200 psi, the Tsai-Wu criterion predicts significantly more cracks, mainly distributed circumferentially, though there are many cracks in the axial direction. The first fiber failure pressures with the associated percent damage are listed in Table 4.4. The first fiber failure pressure predicted by the Tsai-Wu criterion is 10% lower than the pressure predicted by the maximum stress criterion. There is also a factor of 2 in the percent damage predicted.

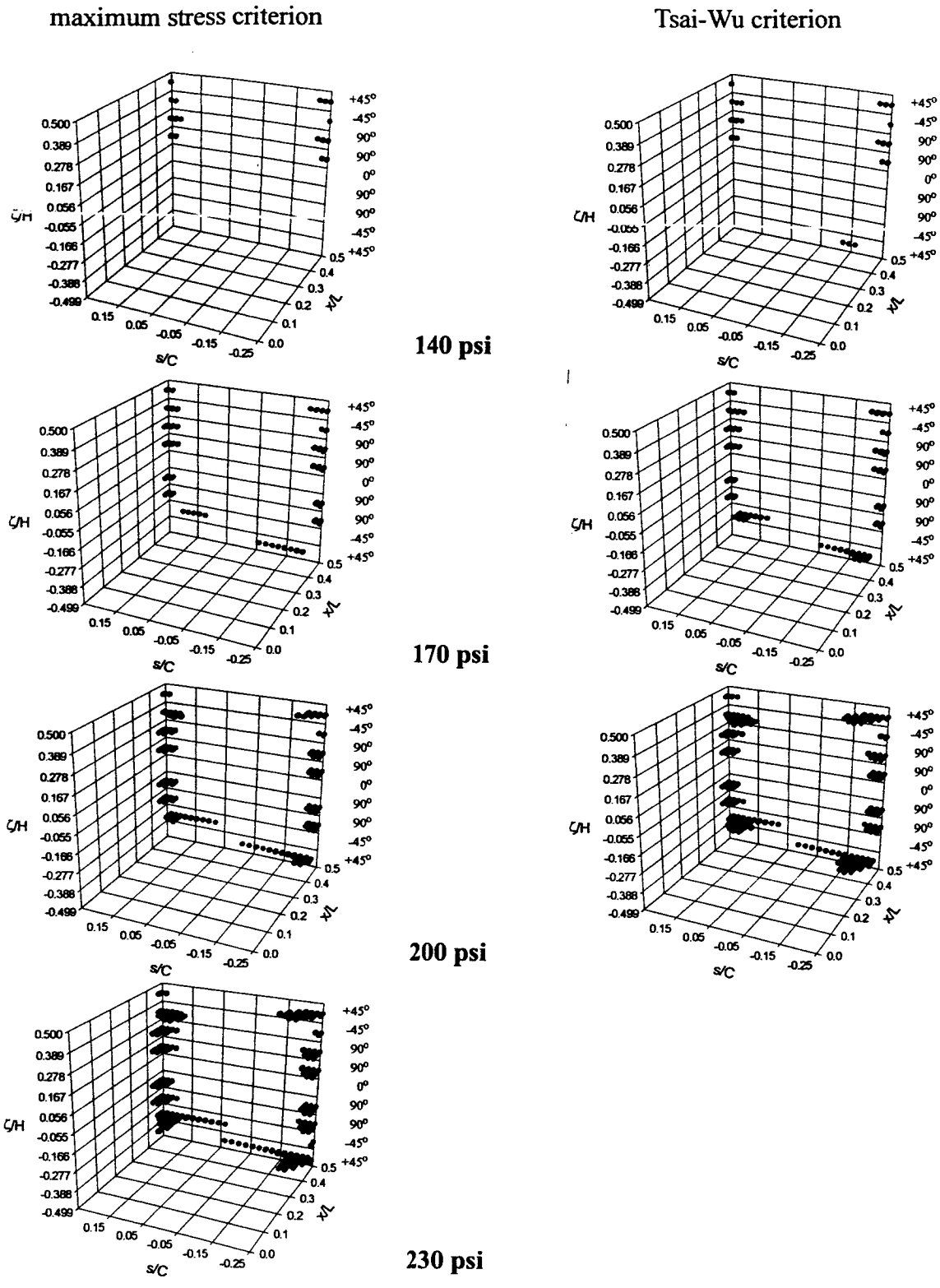

Figure 4.5 Matrix cracking scenarios for maximum stress and Tsai-Wu failure criteria for the circumferentially-stiff $[\pm 45/90_2/0_{1/2}]_s$ elliptical cylinder, non-recursive degradation of E_2, ν_{12}, and ν_{21}, β=0.2

Table 4.3: Maximum stress and Tsai-Wu failure criteria predictions of initial matrix failure pressures

	First matrix failure pressure, psi	
Cylinder orthotropy	Maximum stress criterion	Tsai-Wu criterion
quasi-isotropic	138	132
circumferentially-stiff	105	106
axially-stiff	139	133

Table 4.4: Maximum stress and Tsai-Wu failure criteria predictions of first fiber failure pressures and percent damage, non-recursive degradation of E_2, ν_{12}, and ν_{21}, β=0.2

Criterion	Maximum Stress		Tsai-Wu	
Cylinder orthotropy	First fiber failure pressure, psi	Percent damage[a]	First fiber failure pressure, psi	Percent damage[a]
quasi-isotropic	246	5.5	216	3.0
circumferentially-stiff	255	6.7	221	3.9
axially-stiff	253	26.2	227	12.2

a. Number of failed integration points / total number of integration points

4.3 Summary of Matrix Failure Scenarios in Internally Pressurized Elliptical Cylinders Using Different Failure Criteria

In this chapter, the matrix failure scenarios up to first fiber failure predicted by the non-interactive maximum stress criterion, and two interactive criteria, namely, the Hashin and Tsai-Wu failure criteria, were investigated for the quasi-isotropic, circumferentially-stiff, and axially-stiff cylinders. The results revealed that all three criteria predicted only failures due to excessive σ_2 stress and similar locations of initial matrix failures. Except for the circumferentially-stiff cylinder, the initial matrix failure pressures, however, were lower when the interactive failure criteria were used. For the circumferentially-stiff cylinder, compared to the maximum stress criterion, the Hashin failure criterion predicted the same matrix failure pressure and the Tsai-Wu failure crite-

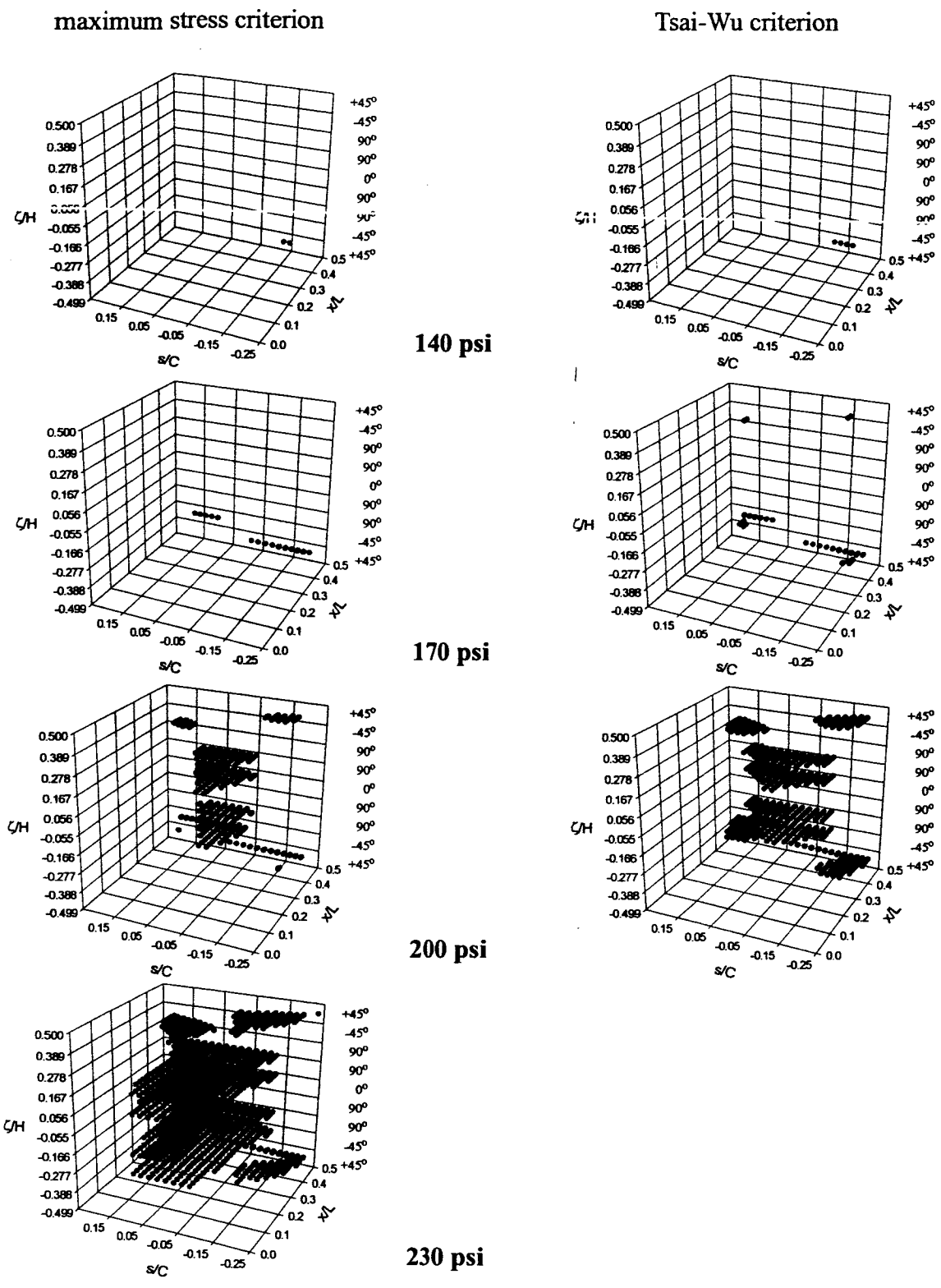

Figure 4.6 Matrix cracking scenarios for maximum stress and Tsai-Wu failure criteria for the axially-stiff $[\pm 45/0_2/90_{1/2}]_s$ elliptical cylinder, non-recursive degradation of E_2, ν_{12}, and ν_{21}, β=0.2

rion predicted a higher first matrix failure pressure. The failure distributions were found to depend on the failure criterion used. The interactive criteria predicted more matrix cracking at all pressure levels. Except for the axially-stiff case, the first fiber failure pressures were found to be lower for the interactive criteria. Particularly, the first fiber failure pressures were predicted to be significantly lower by the Tsai-Wu criterion. For the axially-stiff case, the Hashin criterion predicted a slightly higher first fiber failure pressure. The percent damage at first fiber failure predicted by the Hashin criterion was higher than that found by the maximum stress criterion. On the other hand, the percent damage at first fiber failure found by the Tsai-Wu criterion was lower than the that predicted by the maximum stress criterion. Like the maximum stress criterion, the interactive criteria predicted that at least one layer remained crack-free, impeding the formation of a leakage path.

As leakage is the primary interest of this study, attention now turns to determining the pressure levels and failure conditions that lead to leakage.

Chapter 5 Failure Analysis Beyond Fiber Failure in Internally Pressurized Elliptical Cylinders

In the previous chapters, it was shown that regardless the degradation schemes or failure criteria used to predict the matrix failure scenarios up to first fiber failure, no leakage paths developed in any of the cases studied. If the failure analysis continues to higher pressures, at some pressure, at certain axial and circumferential locations, there will be failure in some form in all layers, thus resulting in a complete leakage path. This chapter will present the results of the failure analysis beyond first fiber failure, until a leakage path is found in each of the cylinders. At that condition, the pressure, location, and modes of failures associated with leakage are determined and the amount of fiber damage assessed. In determining the factors involved with leakage, the PFA in STAGS continues to be used for this phase of the study. The PFA configuration employed uses only the maximum stress failure criterion with the baseline degradation scheme and a degradation factor of β=0.2. It is important to note that in this chapter the definition of the baseline degradation scheme also includes the degradation of E_1, G_{12}, ν_{12}, and ν_{21} when fiber failure is encountered and G_{12} when inplane shear failure is found.

5.1 Leakage Path Formation in Internally Pressurized Elliptical Cylinders

In fig 5.1, the failure progression up to the pressure where a leakage path forms in the quasi-isotropic cylinder is shown. The figure is arranged so that the failure maps in the left column are associated with matrix failure modes, the middle column corresponds to fiber failure modes, and the right column corresponds to the inplane shear mode. The upper left map at a pressure of 230 psi only displays matrix tensile failures, as shown previously in figs. 3.4, 3.5, and other subsequent figures. The maps at 246 psi correspond to the first fiber failure event. Note that at this pres-

sure the map in the middle column shows a single fiber failure, indicated by a blue square symbol, at the clamped end, near s/C=–0.15, in the outer +45° layer, layer 8. This failure is due to excessive compressive σ_1 stress in the fiber direction. This fiber failure is believed to be due to bending effects at the clamped end. Also, it should be pointed out that, as mentioned earlier, at the first fiber failure pressure, in the matrix failure map, the two 0° layers, layers 3 and 6, are free of failures, thus preventing a leakage path formation. At 254 psi, the map in the left column indicates that the matrix tensile failures continue to progress axially and circumferentially, with new failures developing, particularly, in the crown region, away from the clamped end. Those particular failures appear in a 0° layer, layer 6, which was previously uncracked. Layer 3 remains uncracked. At the same pressure, the map in the middle column shows that more compressive fiber failures occur in the outer +45° layer and in layer 6, a 0° layer. Also new tensile fiber failures, denoted by the red square symbols, develop in the inner –45° layer, layer 2. The map in the right column displays the initial inplane shear failures, denoted by green triangular symbols, occurring in layers 3 through 6. It is important to note that these shear failures occur suddenly and in the same axial and circumferential region where the initial matrix and fiber failures occurred. Although at 254 psi it can be seen that all layers of the laminate sustain failures, there is still not a complete leakage path at any particular axial and circumferential location. From the maps at this pressure, it becomes evident that a leakage path seems to begin developing at the clamped end near s/C=–0.15, where all but one layer, layer 7, exhibit some kind of failure. This can be verified if all three maps are superimposed. At the next pressure level shown, 255 psi, the map associated with matrix failures displays compressive matrix failures (blue round symbols), due to excessive compressive σ_2 stress in the direction perpendicular to the fibers, occurring in the +45° layer, layer 7, which was the only layer that remained uncracked. The map showing fiber tensile and compressive failures indicates that these failures progress circumferentially in the layers where they initiated. Also new fiber tensile failures occur in the other 0° layer, layer 3. The inplane shear failure map shows that more shear failures develop in most of the layers near s/C=–0.15. If the three maps are superimposed, a complete leakage path can be observed near s/C=–0.15. A combination of matrix tensile and compressive, fiber tensile and compressive, and inplane shear failure modes are responsible for the formation of this leakage path. The leakage pressure of 255 psi is less than 4% greater than the first fiber failure.

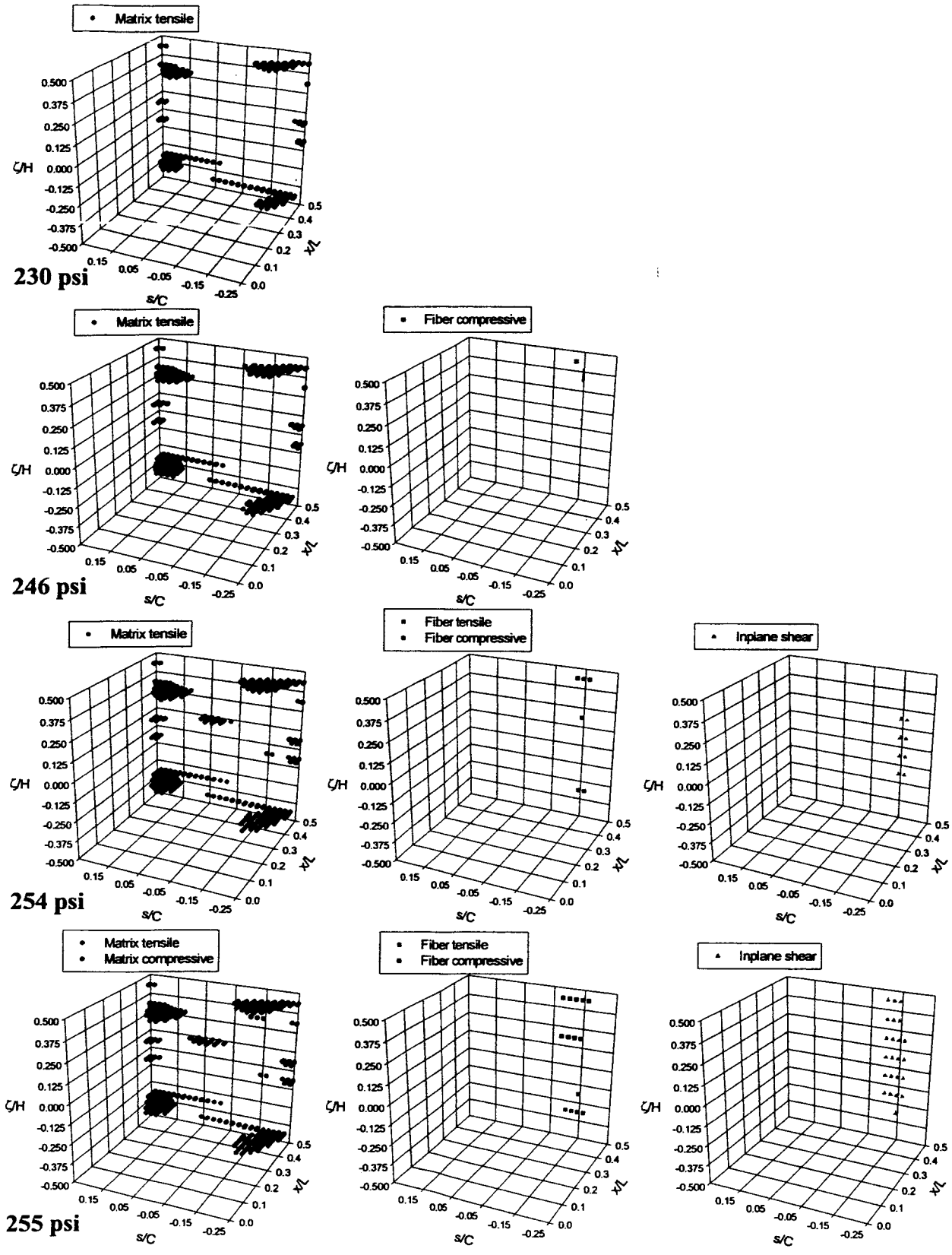

Figure 5.1 Modes of failure involved in leakage for the quasi-isotropic $[\pm 45/0/90]_s$ elliptical cylinder, baseline degradation scheme, maximum stress criterion, β=0.2

For the circumferentially-stiff cylinder, following a similar format to Fig. 5.1, Fig. 5.2 shows the failure maps at the pressures of 230 psi, 253 psi, and 254 psi. As shown previously in the center column of Fig. 3.5, at 230 psi, only matrix tensile failures occur. At 253 psi, the initial fiber failure occurs. The map in the middle column, at this pressure, shows that, as was the case for the quasi-isotropic cylinder, the initial fiber failure occurs due to excessive compressive σ_1 stress, in layer 9, a +45 ° layer, near s/C=–0.15 at the clamped end. Again, bending effects are believed to be responsible for this failure in an outer layer. The map in the left column shows a pronounced circumferential progression of matrix cracks, particularly, in the three inner layers, relative to the 230 psi condition. Note also that, in this matrix cracking map, the only 0° layer, layer 5, exhibits no damage, preventing the formation of a leakage path. At 254 psi, the initial inplane shear failures develop. These shear failures, which appear suddenly, also occur near s/C=–0.15 at the clamped end in all layers except in layer 1. Also at this pressure, more fiber compressive failures occur in layer 9 and new fiber tensile failures occur in the inner –45° layer, layer 2. If these three maps are superimposed, a complete leakage path can be observed in the region near s/C=–0.15 at the clamped end due to a combination of matrix tensile, fiber compressive and tensile, and inplane shear failure modes. The closeness of the first fiber failure pressure, 253 psi, to the leakage pressure, 254 psi, is quite surprising.

With the same format of Fig. 5.1 and Fig. 5.2, Fig. 5.3 shows the failure progression that leads to the formation of a leakage path in the axially-stiff cylinder. The first pressure level of 230 psi, shown previously in the right column of Fig. 3.5, corresponds to a pressure where only matrix tensile failures occur. At 251 psi, as seen in the map of the middle column, initial fiber failure occurs at the clamped end near s/C=–0.15 in the +45° layer, layer 9, due to excessive compressive σ_1 stress. As mentioned in previous chapters, though the matrix failure map in the left column exhibits significant amount of damage at first fiber failure pressure, the 90° layer, layer 5, remains crack-free, preventing a leakage path formation. The next pressure level shown, 265 psi, is when the initial inplane shear failures occur. Again, it can be seen that for this cylinder these failures develop suddenly and occur in several layers. More fiber compressive failures and fiber tensile failures can also be seen in layers 2, 3, 7, and 9 at 265 psi, in the map of the middle column. Also

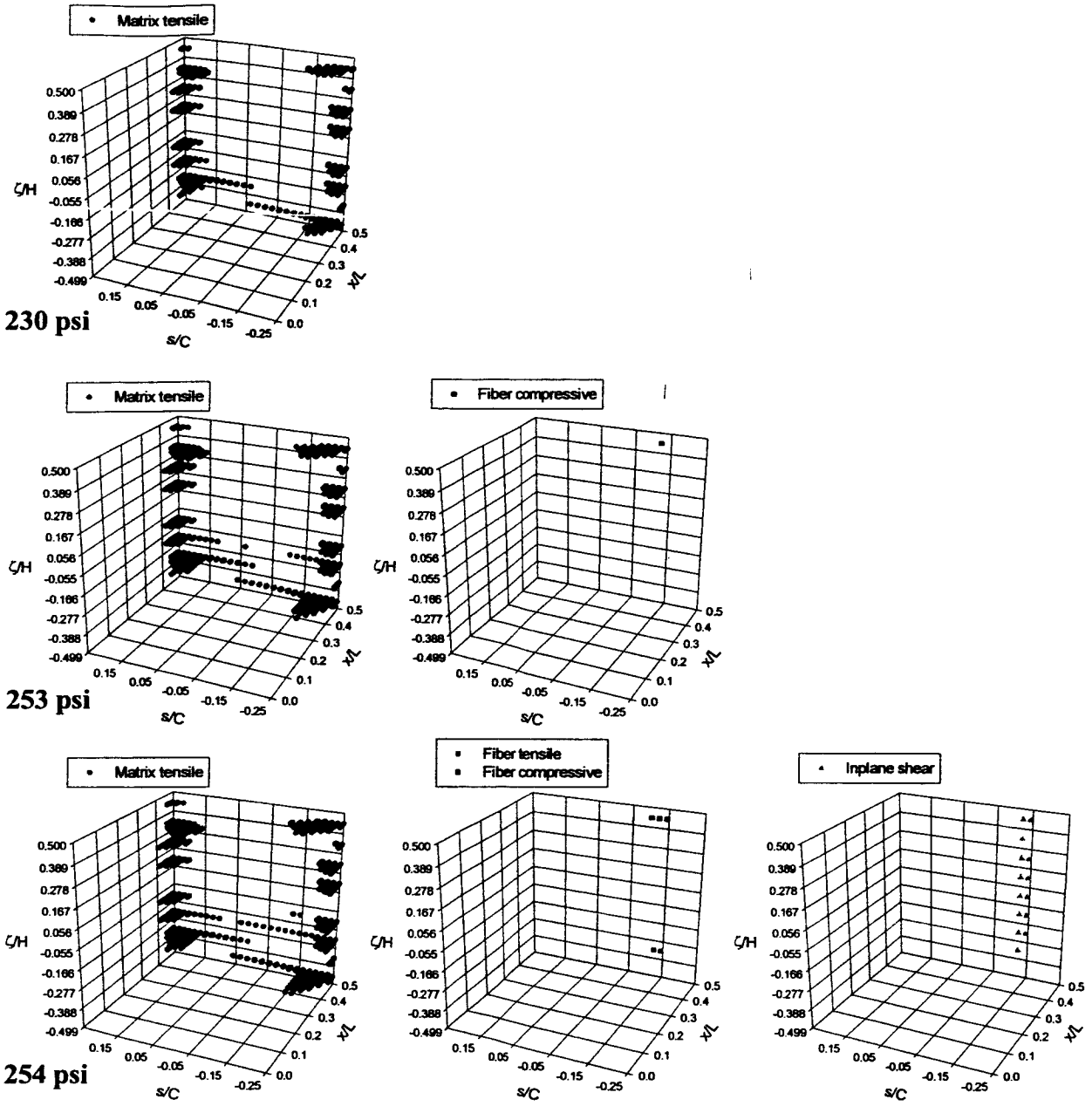

Figure 5.2 Modes of failure involved in leakage for the circumferentially-stiff $[\pm 45/90_2/0_{1/2}]_s$ elliptical cylinder, baseline degradation scheme, maximum stress criterion, β=0.2

at this pressure, though difficult to see in the map of the left column, the single 90° layer remains uncracked regardless the large amount of matrix tensile failures. In addition, there is also matrix compressive failures occurring in the outer –45° layer, layer 8. Again, if the three maps are super-

imposed, a leakage path can be observed at the clamped end near s/C=–0.15 due to matrix tensile and compressive, fiber tensile and compressive, and inplane shear failure modes.

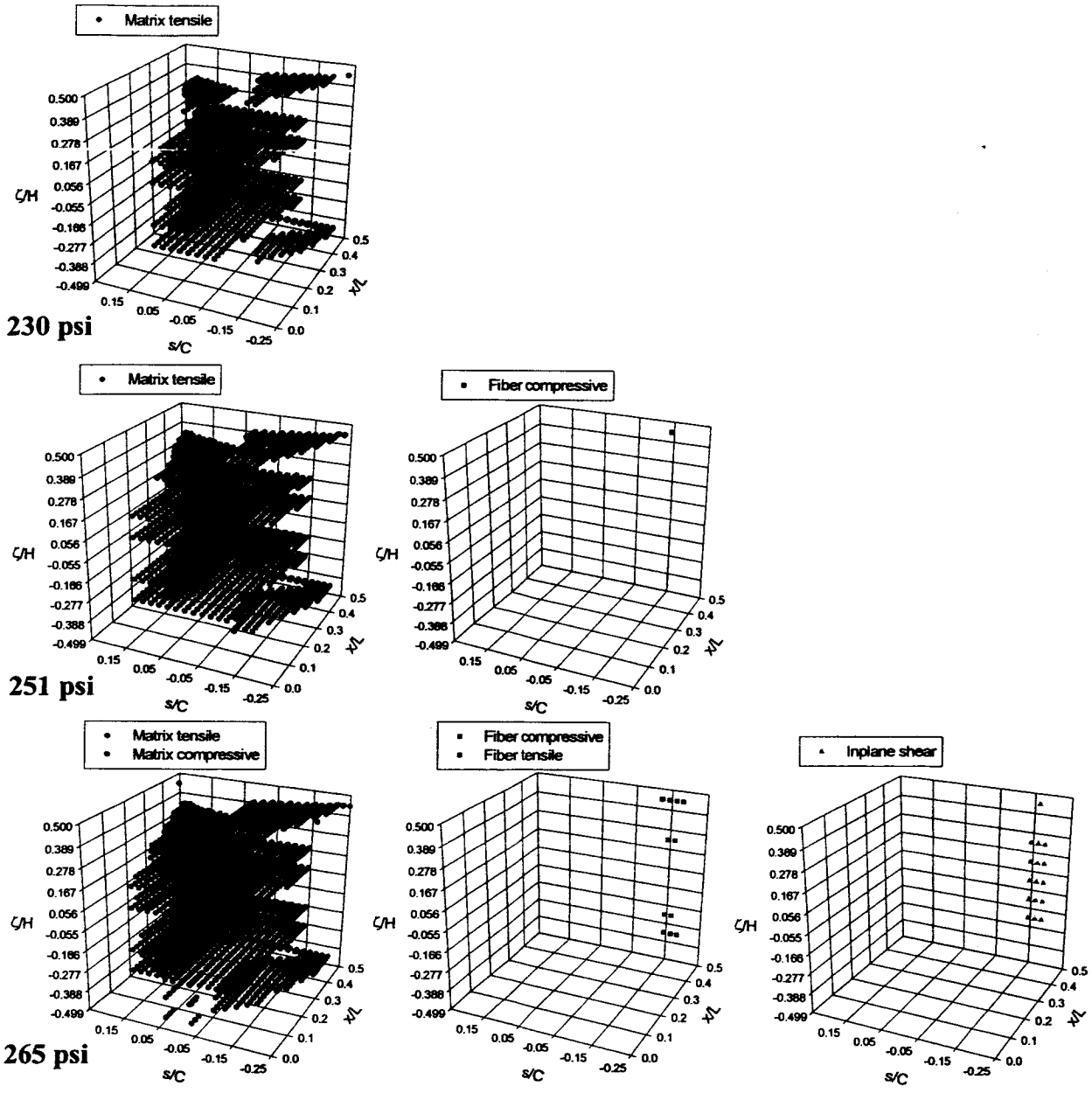

Figure 5.3 Modes of failure involved in leakage for the axially-stiff $[\pm 45/0_2/90_{1/2}]_s$ elliptical cylinder, baseline degradation scheme, maximum stress criterion, β=0.2

5.2 Summary of Failure Analysis Beyond Fiber Failure in Internally Pressurized Elliptical Cylinders

The results presented in this chapter have shown that leakage occurs in the quasi-isotropic, circumferentially-stiff, and axially-stiff cylinders studied due to a combination of failure modes. Specifically, it was found that matrix tensile and compressive, fiber tensile and compressive, and inplane shear failure modes contribute to the formation of leakage paths. The axial and circumferential locations where leakage paths initially form were found to be similar for all three cylinders and the leakage pressures were within 4% of each other. Table 5.1 summarizes the leakage pressures. This fact suggests that the formation of leakage paths depend on the elliptical geometry rather than on material orthotropy.

At leakage, the quasi-isotropic and axially-stiff cylinders sustained similar amount of fiber damage. The circumferentially-stiff cylinder, in the other hand, sustained the least amount of fiber damage. However, in all the cylinders, when leakage occurs, the overall number of fibers that have failed is relatively small. Also, for all cylinders it was found that shear failures develop suddenly, and soon after, leakage occurs.

Table 5.1: Leakage pressures, baseline degradation scheme, maximum stress criterion, β=0.2

Cylinder orthotropy	Leakage pressure, psi
quasi-isotropic	255
circumferentially-stiff	254
axially-stiff	265

Chapter 6 Conclusions and Future Work

6.1 Conclusions

The goals of the work presented, defined in Chapter 1, have been accomplished. Specifically, using a progressive failure analysis approach, the conditions leading to leakage in internally pressurized elliptical cylinders with various material orthotropies have been investigated. In the investigation, the progressive failure analysis capability, PFA option, of the finite-element code STAGS was utilized. As discussed in Chapter 2, the PFA accounts for the localized loss of stiffness when material failure occurs by reducing the local engineering properties by a certain degradation factor. The manner in which this degradation of engineering properties takes place depends on the failure modes, which are determined by the use of a failure criterion. The PFA was performed on a quasi-isotropic, circumferentially-stiff, and axially-stiff cylinders. The results obtained using this analysis were organized in two parts. First, the failure scenarios for the three cylinders at pressures below the levels to cause fibers to fail were studied. From these failure scenarios obtained using the PFA option with different degradation schemes and various failure criteria, it was determined that before fibers began to fail in each of the three cylinders, only matrix tensile failures, or matrix cracking, develop within the cylinder walls. Though some differences between the matrix cracking scenarios were found to depend, in some instances, on the particular degradation scheme and failure criterion used, leakage at those pressure levels did not occurred in any of the cylinders because at least one layer always remained crack-free, preventing the formation of a leakage path. The following list summarizes the main differences determined from the comparisons made between the matrix cracking scenarios obtained for the quasi-isotropic, circumferentially-stiff, and axially-stiff cylinders using the PFA with several degradation schemes and failure criteria.

1. PFA with maximum stress failure criterion and several degradation schemes.
   - *Effects of material orthotropy*: The pressure and locations of initial matrix cracks were found to depend on material orthotropy. At higher pressures, the cracking patterns for the quasi-isotropic and circumferentially-stiff cylinders were found to be similar. The cracking pattern for the axially-stiff cylinder, in the other hand, was remarkably different than the other two cylinders, as the amount of damage sustained by the axially-stiff cylinder was significantly higher.
   - *Effects of not degrading* G_{12}: The importance of the inplane shear modulus in resisting matrix cracking was insignificant for the quasi-isotropic cylinder. For the circumferentially-stiff and axially-stiff cylinders, it was found that by not degrading the shear modulus, these cylinders sustain slightly less damage and higher first fiber failure pressures.
   - *Effects of different degradation factors*: A severe degradation of the engineering properties was found to produce more damage in the circumferentially-stiff and axially-stiff cylinders than a less severe, or no, degradation. This trend was not observed in the quasi-isotropic cylinder. In fact, the damage at the first fiber failure pressure for the quasi-isotropic cylinder was found to be the same for the different degrees of degradation used.
   - *Effects of recursive degradation*: By continuously degrading the engineering properties as the load increased, the cracking scenarios at each load level for the circumferentially-stiff and axially-stiff cylinders exhibited more damage than when a non-recursive degradation was performed. However, for the circumferentially-stiff, the amount of damage at first fiber failure pressure was, for all purposes, unaffected by the recursive degradation. For the axially-stiff cylinder, when a recursive degradation was performed, the first fiber failure occurred at a lower pressure, and the amount of damage at this pressure was higher that when a non-recursive degradation was used. The matrix failure scenarios for the quasi-isotropic cylinder was unaffected by the recursive degradation.
   - *Effects of different computational algorithms*: If a very small or zero value of the degradation factor is used with the PFA in STAGS, a numerical overflow may occur. Two optional algorithms that help prevent that problem were compared with the default

algorithm. The failure scenarios for the quasi-isotropic, circumferentially-stiff, and axially-stiff cylinders were determined using all three algorithms. No significant differences were found between the different computational algorithms.

2. PFA with baseline degradation scheme and a degradation factor of 0.2
   - *Effects of interactive failure criteria*: For the three cylinders studied, the failure scenarios resulting from using the non-interactive maximum stress criterion were compared to the scenarios predicted by the interactive Hashin and Tsai-Wu criteria. Except for the circumferentially-stiff cylinder, the initial matrix failure pressures were lower when the interactive failure criteria were used. For the circumferentially-stiff cylinder, the Tsai-Wu failure criteria predicted a higher first matrix failure pressure. The interactive criteria predicted more matrix cracking at all pressure levels. Except for the circumferentially-stiff case, the first fiber failure pressures were found to be lower for the interactive criteria. In particular, the first fiber failure pressures were predicted to be significantly lower by the Tsai-Wu criterion. For the axially-stiff case, the Hashin criterion predicted a slightly higher first fiber failure pressure. The amount of damage at first fiber failure found by the Tsai-Wu criterion was lower than the that predicted by the maximum stress criterion.

The second part of the results involved the progression of failures occurring at pressures above first fiber failure pressures up to leakage pressures. In all three cylinders, it was found that leakage occurred due to a combination of matrix, fiber, and inplane shear failure modes in adjacent layers of the laminates. In the circumferentially-stiff and axially-stiff cylinders, at pressures when shear failures, which developed suddenly, occurred, complete leakage paths at certain axial and circumferential locations formed. In the quasi-isotropic cylinder, soon after shear failures appeared, leakage developed. At leakage, the quasi-isotropic and axially-stiff cylinders sustained similar amount of fiber damage. The circumferentially-stiff cylinder, in the other hand, sustained the least amount of fiber damage. However, in all the cylinders, when leakage occurred, the overall number of fibers that failed was found to be relatively small. The leakage paths formed in zones of high bending and high inplane shear stresses, which were believed to cause initial matrix failure in the quasi-isotropic and axially stiff cylinders, at the clamped ends of the cylinders. It is

suspected the elliptical geometry rather than material orthotropy influenced the formation of these paths at those locations. Leakage was found to occur at very similar pressures for the quasi-isotropic and circumferentially-stiff cylinders. Though the leakage pressure for the axially-stiff cylinder was found to be higher, all pressures were within 4% of each other.

6.2 Future work

To move forward in this research, the following issues should be addressed in the failure analysis of the elliptical cylinder with different material orthotropies:

i. Since the basic research presented here is based on the idea that non-circular laminated composite cylinders may be used in future designs of fuel tanks for reusable launch vehicles, a study with combined loading, which simulate the conditions under which these tanks may be subjected to, could be taken into consideration.

ii. Also, since typical fuels used in reusable launch vehicles may involve liquefied gases at cryogenic temperatures, the basic stages of the research could benefit if thermal stresses are included in the analysis.

iii. Since stress concentrations, which eventually may lead to leakage in non-circular cross sections, as shown in this work for the elliptical cylinder, depend on the particular noncircular geometry and occur at locations that are not entirely obvious, tailoring of fibers in certain optimal fashion could compensate for the non-circular geometry, thus preventing the zones of high stresses.

iv. Experimental work should be undertaken to compare with the results presented here. Critical issues to be consider in this regard include not only the fabrication of the elliptical cylinders but also the implementation of boundary conditions and the monitoring of failures.

References

1 McMurray, J. M. and M. W. Hyer, "Response and Failure of Internally Pressurized Elliptical Composite Cylinders," Virginia Tech Center For Composite Materials and Structures, Report CCMS-99-09, available Virginia Tech Center for Composite Materials and Structures, Mail Code 0219, Blacksburg, VA 24061.

2 McMurray, J. M. and Hyer M. W. "Response and Failure Characteristics of Internally Pressurized Elliptical Composite Cylinders," *AIAA Journal*, vol. 40, No. 1, 2002, pp. 117-125.

3 McMurray, J. M. and Hyer M. W. "Failure Analysis of Internally Pressurized Composite Cylinders," AIAA paper no. 2001-1185, presented at 42nd AIAA/ASME/ASCE/AHS/ASC Structures, Structural Dynamics, and Materials Conference, Seattle, WA, 2001.

4 Sleight, D. W., Knight N. F., Jr., and Wang, J. T. "Evaluation of a Progressive Failure Analysis Methodology for Laminated Composite Structures," AIAA paper no. 97-1187, presented at 38th AIAA/ASME/ASCE/AHS/ASC Structures, Structural Dynamics, and Materials Conference and Exhibit, Kissimmee, FL, 1997.

5 Camanho P. P. and Mathews F. L. "A Progressive Damage Model for Mechanically Fastened Joints in Composite Materials," *Journal of Composite Materials*, vol. 33, No.24, 1999, pp. 2248-80.

6 Rankin C. C., Brogan F. A., Loden W. A., and Cabiness H. D. "STAGS User Manual, Version 4.0," Lockheed Martin Missiles & Space Co., Inc., Report LMSC P032594, May 2001.

7 Knight, N. F., Jr., Private communication, October 12, 2000.

8 Knight, N. F., Jr., Rankin C. C., and Brogan F. A. "STAGS Computational Procedure for Progressive Failure Analysis of Laminated Composite Structures," *International Journal of Non-Linear Mechanics*, vol. 37, issues 4-5, pp.833-849, 2002.

9 Saada, A. S., *Elasticity Theory and Applications*. New York, NY: Pergamon Press Inc., 1974.

10 Brush D. O. and Almroth, B. O., *Buckling of Bars, Plates, and Shells*. New York, McGraw-Hill, 1975.